

AFIT/GE/ENG/97D-08

EVALUATION OF A MAXIMUM
A-POSTERIORI SLOPE ESTIMATOR FOR
A HARTMANN WAVEFRONT SENSOR

THESIS

Troy B. Van Caster
Captain, USAF

DTIC QUALITY INSPECTED 2

AFIT/GE/ENG/97D-08

19980130 150

Approved for public release; distribution unlimited

The views expressed in this thesis are those of the author and do not reflect the official policy or position of the Department of Defense or the United States Government.

AFIT/GE/ENG/97D-08

EVALUATION OF A MAXIMUM
A-POSTERIORI SLOPE ESTIMATOR FOR
A HARTMANN WAVEFRONT SENSOR

THESIS

Presented to the Faculty of the School of Engineering
of the Air Force Institute of Technology
Air University
In Partial Fulfillment of the
Requirements for the Degree of
Master of Science in Electrical Engineering

Troy B. Van Caster, B.S.E.E., M.E.M.
Captain, USAF

December 1997

Approved for public release; distribution unlimited

EVALUATION OF A MAXIMUM
A-POSTERIORI SLOPE ESTIMATOR FOR
A HARTMANN WAVEFRONT SENSOR

Troy B. Van Caster, B.S.E.E., M.E.M.

Captain, USAF

Approved:

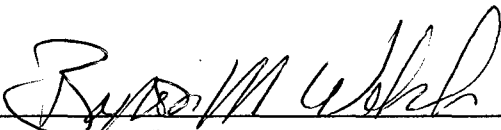

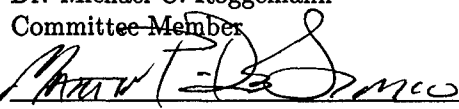
 _____ Dr. Byron M. Welsh Thesis Advisor	<u>10/30/97</u> _____ Date
 _____ Dr. Michael C. Roggemann Committee Member	<u>10/30/97</u> _____ Date
 _____ Dr. Marty DeSimio Committee Member	<u>30 Oct 97</u> _____ Date

Table of Contents

	Page
List of Figures	vii
Abstract	x
 I. Background	 1-1
1.1 Introduction	1-1
1.2 Atmospheric turbulence	1-2
1.3 Adaptive optics systems	1-4
1.4 Hartmann wave-front sensor	1-5
1.5 Maximum <i>a-posteriori</i> estimators	1-5
1.6 Goal of research	1-6
1.7 Overview	1-7
 II. Imaging theory and wavefront sensor simulation development	 2-1
2.1 Introduction	2-1
2.2 Image formation	2-1
2.3 Image detection	2-2
2.3.1 Shot noise	2-2
2.3.2 Read noise	2-3
2.4 Hartmann wavefront sensor	2-3
2.5 Hartmann wavefront sensor simulation	2-5
2.6 Using the wavefront sensor simulation	2-11
 III. Implementation of a maximum <i>a-posteriori</i> estimator	 3-1
3.1 Introduction	3-1
3.2 Maximum <i>a-posteriori</i> estimator	3-1
3.3 Slope correlation	3-2

	Page
3.4 Slope correlation matrix development	3-5
3.5 Slope correlation equations	3-7
3.5.1 Kolmogorov turbulence statistics	3-7
3.5.2 von Karman turbulence statistics	3-8
3.5.3 Implementation	3-9
3.6 Theoretical MAP estimator performance	3-10
3.6.1 Correction factor matrix	3-10
3.6.2 MAP estimator performance using Kolmogorov statistics . .	3-11
3.6.3 MAP estimator performance using von Karman statistics . .	3-13
IV. Verification of simulation performance and test plan	4-1
4.1 Introduction	4-1
4.2 Hartmann wavefront sensor simulation verification	4-1
4.3 Centroid estimator RMSE performance	4-3
4.3.1 Shot noise effects	4-3
4.3.2 Read noise effects	4-4
4.3.3 Atmospheric turbulence effects	4-6
4.4 MAP estimator performance	4-6
4.4.1 Introduction	4-6
4.4.2 Simulation flowchart	4-7
4.4.3 Simulation performance	4-8
4.5 Test plan	4-11
V. Results and Analysis	5-1
5.1 Introduction	5-1
5.2 Global tilt	5-1
5.3 Intensity overlap	5-2
5.4 Detector array size	5-5

	Page
5.4.1 Relative MSE for a fixed ratio of σ_c^2/σ_p^2	5-5
5.4.2 Absolute MSE for a fixed ratio of σ_c^2/σ_p^2	5-6
5.4.3 Relative MSE for a fixed detector array size.	5-7
5.4.4 Absolute MSE for a fixed detector array size.	5-8
5.5 Read noise	5-12
5.5.1 Relative MSE as detector read noise increases.	5-12
5.5.2 Absolute MSE as detector read noise increases.	5-12
5.6 Using incorrect atmospheric parameters in the MAP estimator	5-18
5.7 SOR Generation III detector configuration	5-22
VI. Conclusions	6-1
6.1 Introduction	6-1
6.2 Summary of Methodology	6-1
6.3 MAP estimator performance	6-2
6.4 Recommendations	6-2
Appendix A. Slope correlation for Kolmogorov Statistics	A-1
Appendix B. Slope correlation for von Karman Statistics	B-1
Appendix C. Shot limited performance	C-1
Appendix D. Wavefront sensor source code listing	D-1
D.1 Wavefront sensor code	D-1
D.2 Poisson number generator	D-4
D.3 Phase screen tilt removal	D-5
Appendix E. Correlation generation source code listing	E-1
E.1 Source code for building Kolmogorov correlation matrices	E-1
E.2 Source code for building von Karman correlation matrices	E-4
E.3 Function for Two dimensional numerical integration	E-7

	Page
Bibliography	BIB-1
Vita	VITA-1

List of Figures

Figure		Page
1.1.	Turbulence model	1-3
1.2.	Adaptive optics system	1-4
2.1.	Single lens imaging system	2-1
2.2.	Hartmann WFS	2-3
2.3.	Piecewise linear representation of a wavefront.	2-4
2.4.	Simulation flow chart	2-6
2.5.	Hartmann wavefront sensor simulation I	2-10
2.6.	Hartmann wavefront sensor simulation II	2-10
2.7.	Wave front sensor array numbering	2-13
3.1.	Slope correlation geometry	3-2
3.2.	Subaperture slope geometry	3-6
3.3.	Correction factor matrix behavior	3-11
3.4.	Theoretical MAP performance using Kolmogorov statistics	3-12
3.5.	Theoretical MAP performance using von Karman statistics	3-14
4.1.	Shot noise limited RMSE performance	4-3
4.2.	Centroid RMSE performance	4-4
4.3.	Theoretical RMSE performance with read noise	4-6
4.4.	Centroid estimator RMSE performance with read noise	4-7
4.5.	Theoretical RMSE performance with atmospheric turbulence	4-8
4.6.	Centroid estimator RMSE performance with atmospheric turbulence	4-9
4.7.	Theoretical MAP performance in simulation	4-11
4.8.	Modified detector configuration	4-13
4.9.	Shell program flow chart	4-14

Figure		Page
5.1.	Relative MSE performance with global tilt removed	5-2
5.2.	Relative MSE with overlap allowed	5-3
5.3.	MAP estimator MSE performance with overlap	5-4
5.4.	Relative MSE with overlap and large focal length	5-5
5.5.	Relative MSE for a finite detector array with $\sigma_c^2/\sigma_p^2 = 2$	5-6
5.6.	Relative MSE for a finite detector array with $\sigma_c^2/\sigma_p^2 = 1$	5-7
5.7.	Relative MSE for a finite detector array with $\sigma_c^2/\sigma_p^2 = 1/2$	5-8
5.8.	Relative MSE for a finite detector array with $\sigma_c^2/\sigma_p^2 = 1/4$	5-9
5.9.	MAP and centroid MSE performance for $\sigma_c^2/\sigma_p^2 = 1/2$	5-9
5.10.	Relative MSE for a 2×2 detector array	5-10
5.11.	Relative MSE for a 4×4 detector array	5-10
5.12.	Relative MSE for a 8×8 detector array	5-11
5.13.	MAP and centroid MSE for a 4×4 detector array	5-11
5.14.	Relative MSE for a 2×2 detector array with read noise and $\sigma_c^2/\sigma_p^2 = 1$. . .	5-13
5.15.	Relative MSE for a 4×4 detector array with read noise and $\sigma_c^2/\sigma_p^2 = 1$. . .	5-14
5.16.	MAP and centroid estimator MSE performance for a 4×4 detector array with read noise.	5-14
5.17.	Relative MSE for a 2×2 detector array with read noise and $\sigma_c^2/\sigma_p^2 = 1/2$. .	5-15
5.18.	Relative MSE for a 4×4 detector array with read noise and $\sigma_c^2/\sigma_p^2 = 1/2$. .	5-15
5.19.	MAP and centroid estimator MSE performance for a 4×4 detector array with read noise.	5-16
5.20.	Relative MSE for a 2×2 detector array with read noise and $\sigma_c^2/\sigma_p^2 = 1/4$. .	5-16
5.21.	Relative MSE for a 4×4 detector array with read noise and $\sigma_c^2/\sigma_p^2 = 1/4$. .	5-17
5.22.	MAP and centroid estimator MSE performance for a 4×4 detector array with read noise.	5-17
5.23.	Relative MSE using incorrect Fried parameters with $\sigma_R^2 = 0$	5-19
5.24.	MAP and centroid MSE using incorrect Fried parameters with $\sigma_R^2 = 0$	5-19
5.25.	Relative MSE using incorrect Fried parameters with $\sigma_R^2 = 5$	5-20

Figure		Page
5.26.	MAP and centroid MSE using incorrect Fried parameters with $\sigma_R^2 = 5$	5-20
5.27.	Relative MSE using incorrect outer scales for a 2×2 detector array.	5-21
5.28.	Relative MSE using incorrect outer scales for a 4×4 detector array.	5-21
5.29.	Relative MSE using a SOR Generation III detector with $\sigma_R^2 = 0$	5-23
5.30.	Relative MSE using a SOR Generation III detector with $\sigma_R^2 = 5$	5-23
5.31.	Relative MSE using a SOR Generation III detector with $\sigma_R^2 = 10$	5-24
5.32.	MAP and centroid MSE performance using Generation III detector.	5-24
C.1.	Quad cell detector configuration	C-1

Abstract

Current methods for estimating the wavefront slope at the aperture of a telescope using a Hartmann wavefront sensor are based upon a centroid shift estimator. The centroid shift estimator determines the displacement, or shift, of the centroid off the optical axis using a moment calculation of the intensity distributions recorded in each subaperture. This centroid shift is proportional to the average slope of the wavefront in each subaperture. A maximum *a-posteriori* (MAP) slope estimator takes advantage of *a-priori* knowledge of the wavefront slope statistics and total irradiance falling on the subaperture detector arrays when determining the shift estimate. In order to derive a closed form solution for the MAP estimator, several assumptions were made: infinite resolution on the detector arrays, no read noise in the detection process, and no intensity spillover into adjacent subapertures. By implementing the Hartmann wavefront sensor and MAP estimator in simulation, the performance of the MAP estimator was evaluated using realizable wavefront sensor parameters. While the MAP estimator mean square error (MSE) performance decreased relative to the centroid estimator MSE performance as a result of spillover, finite detector resolution, and read noise, the MAP estimator MSE performance was found to be upper bounded by the centroid estimator MSE in all cases.

EVALUATION OF A MAXIMUM *A-POSTERIORI* SLOPE ESTIMATOR FOR A HARTMANN WAVEFRONT SENSOR

I. Background

1.1 Introduction

It is well known that atmospheric turbulence reduces the resolution of imaging systems. In fact, Isaac Newton recognized that, without correction, the resolution of telescopes was limited not by aperture size, but by the turbulence in the atmosphere [16]. A variety of techniques have been used to improve image resolution. One solution was to build telescopes at higher altitudes. While the higher altitudes significantly reduced the effects of turbulence, this approach had its obvious limitations. Another solution was to compensate for the turbulence using post-processing or adaptive optics techniques. While it has been shown that adaptive optics systems can improve resolution by compensating for the atmospheric effects, cost and complexity often encourage the use of speckle imaging [2, 29] and other post-processing techniques such as inverse filtering or blind deconvolution [1, 20]. Significant research has been done by the Air Force Maui Optical Station (AMOS) and the Starfire Optics Range to improve upon the resolution of systems imaging through the atmosphere using adaptive optics systems [9, 19]. One of the key components of the adaptive optics system is a wavefront sensor. The wavefront sensor gathers information used to estimate the phase of the incident wavefront so the phase delays that distort the image and reduce the overall resolution of the imaging system can be removed. If *a-priori* information about the atmospheric turbulence is used along with the information gathered by the wavefront sensor, better estimates of the wavefront phase can be made. This thesis examined the advantages of using *a-priori* knowledge about the atmospheric turbulence when gathering data to reconstruct and remove the incident wavefront phase distortions. The following sections present the information required to understand

the operation of a Hartmann wavefront sensor and its role in the adaptive optics system, the purpose of the research, summary of results, and a brief thesis overview.

1.2 Atmospheric turbulence

Atmospheric turbulence is caused by the heating and cooling of the Earth's surface by the sun. Uneven temperature distributions in the atmosphere result in the formation of eddies with varying indexes of refraction. These random refractive-index inhomogeneities distort the light that propagates any significant distance through the atmosphere [8]. Consider light propagating from a distant star. Initially, the light propagates outward with a spherical wavefront. After a significant distance, the wavefront can be modeled as planar. As the plane wave propagates through the atmosphere, different parts of the wavefront pass through eddies with differing refractive indexes. As a result, the surface of the wavefront experiences various phase delays and appears to be dimpled. This dimpling effect is a direct result of the light passing through pockets of random index of refraction. The most significant effect of atmospheric turbulence is that it imparts a random tilt on the wavefront [8]. For long exposure images, the random tilt will cause the image to roam around the image plane of the detector, resulting in a blurred image.

Atmospheric turbulence is characterized by a set of parameters which include the outer scale, L_o , and the Fried parameter, r_o . The outer scale is a measure of the largest turbulent eddies that are of a single index of refraction [22]. The Fried parameter is the atmospheric coherence diameter which relates to the overall strength of the turbulence induced perturbations [11]. The turbulent nature of the atmosphere is modeled using wave structure functions. A wave structure function describes the phase and amplitude fluctuations of a wave due to turbulence [5]. For the purpose of the simulations in this thesis, phase structure function statistics will only be considered since the effects of amplitude perturbations are small relative to the effects of phase perturbations [3]. Two common phase structure functions that are used to model the effects of turbulence are the

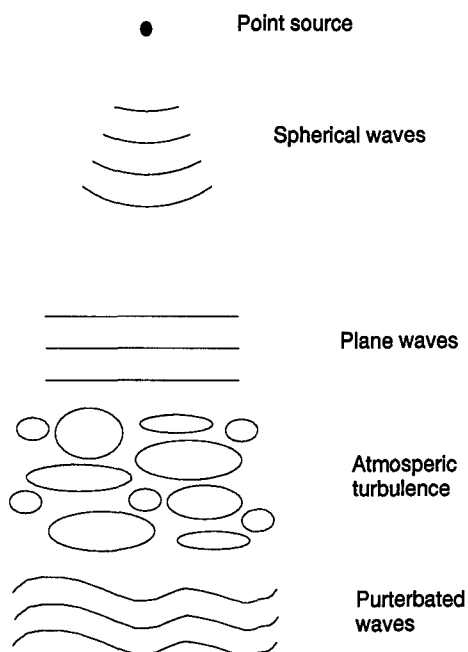


Figure 1.1 Wave front distortions caused by atmospheric turbulence

Kolmogorov structure function and the von Karman structure function. The Kolmogorov structure function assumes infinite outer scale and is the most commonly used model. The von Karman structure function uses a finite outer scale. The outer scale, L_o , is the size of the largest turbulent eddie that is of a single index of refraction. Turbulent eddies larger than L_o are not assumed to be of a single index of refraction, but composed of smaller eddies with various indexes of refraction.

The affect atmospheric turbulence has on the imaging process is that it can only degrade the resolution of the imaging system. As the Fried parameter, r_o , becomes small, the turbulent nature of the atmosphere becomes the limiting factor in the angular resolution of imaging systems, not the aperture size. Fried showed that when the telescope diameter, D , is much less than r_o , the diameter is the limiting factor. But, when D becomes larger than r_o , the resolution is consistent with a telescope with diameter r_o [7].

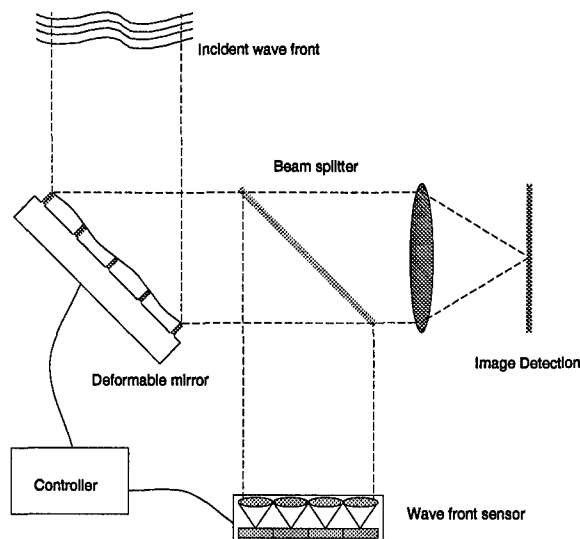


Figure 1.2 A typical wavefront compensation adaptive optical system

1.3 Adaptive optics systems

The fundamental goal of adaptive optics systems is to remove the perturbations caused by atmospheric turbulence in real time, thus improve the overall resolution of the imaging system. The removal of perturbations is accomplished by performing two basic functions: wavefront sensing and wavefront correction. A wavefront sensor measures the turbulence induced phase distortions across the telescope aperture. This data is then used to control a wavefront modifying device. The adaptive optics system shown in Fig. 1.2 uses a technique known as wavefront compensation and is used when the objective is to obtain the best possible image of a distant object viewed through a turbulent path [13]. The wavefront sensor provides the information required to drive a deformable mirror. The purpose of the deformable mirror is to remove the phase perturbations in the wavefront. A tip-tilt mirror can also be used to remove the overall tilt of the incident wavefront [6]. This process is known as global tilt removal. Ideally, the wavefront correction would completely negate the phase perturbations that are present in the telescope aperture. However, there are many factors that contribute to error in the adaptive optics process which result from the inability to produce perfect wavefront sensors and deformable mirrors [10].

1.4 Hartmann wave-front sensor

While numerous wavefront sensing techniques exist [13], this research studies the performance of a Hartmann wavefront sensor. The Hartmann wavefront sensor is a tilt or slope sensor. It consists of an array of lenslets, or subapertures, that segments the incident wavefront in the pupil of the imaging system. An intensity distribution, or centroid, is formed behind each subaperture on a charged coupled device (CCD) detector array. The distance the centroid is displaced from the optical axis is called a shift. The shift is directly related to the average slope of the wavefront in the pupil of the subaperture [3]. Using the centroid shift data from all of the subapertures in the wavefront sensing array, the phase of the incident wavefront can be reconstructed [6, 25, 28]. The accuracy of the shift data will directly affect the accuracy of the wavefront reconstruction as well as the ability of the adaptive optics system to remove the phase perturbations.

1.5 Maximum *a-posteriori* estimators

The accuracy of the data collected by the Hartmann wavefront sensor is limited by the random nature of the atmospheric turbulence and the photo detection process. If the random nature of the atmospheric turbulence and the detection process can be characterized using probability density functions (PDFs), shift estimators that incorporate the PDF information can be developed. If the wavefront turbulence statistics are known *a-priori*, the atmospheric turbulence statistics can be characterized using a posterior PDF and a maximum *a-posteriori* (MAP) estimator can be developed. The approach taken by Sallberg [23] was to model the image detection process as a product of joint PDFs. By maximizing the joint PDF with respect to the shift parameter, a MAP shift estimator was derived. Several assumptions were made in order to obtain a closed form solution for the MAP estimator:

- The intensity distribution on the image plane was modeled as a Gaussian distribution.

- The intensity distribution was sufficiently compact and the local wavefront tilts were sufficiently small so that the intensity distribution formed by one subaperture does not bleed over onto the detector pixels from an adjacent subaperture.
- The CCD detector array was assumed to have infinite spatial resolution.
- The random nature of optical detection was modeled with Poisson statistics.
- The detection process had no read noise.

The resulting MAP estimator incorporated statistical knowledge of wavefront slopes and the detected light levels when estimating the shift data. If all the parameters in the joint PDF were jointly Gaussian, the resulting estimator would be the Minimum Mean Square Error (MMSE) estimator. Since the arrival of photons on the CCD detector was modeled as a Poisson process and the intensity distribution was only approximated by a Gaussian distribution, the MAP estimator will not be an MMSE estimator. Sallberg found that the MAP estimator mean square error (MSE) had the centroid estimator MSE as its upper bound.

1.6 Goal of research

The purpose of this research was to evaluate the performance of Sallberg's MAP estimator [23] under actual operating conditions. Many of the assumptions made by Sallberg no longer hold when considering a realizable wavefront sensor design. The MAP estimator must be evaluated using simulation since a closed form solution can not be found when realizable wavefront sensor parameters are considered. The following MATLAB 5.0[®] simulations were used to complete the research:

- A Fourier series based phase screen generator modified from code developed by Welsh [30].
- A Hartmann wavefront sensor employing an $N \times N$ array of square subapertures.

- A slope correlation matrix generator for von Karman and Kolmogorov atmospheric statistics for use in the MAP estimator.

1.7 Overview

Chapter II covers the principles behind Hartmann wavefront sensors and the simulation development. Chapter III discusses the implementation of Sallberg's MAP estimator and the required equations for the slope correlation matrix. Chapter IV verifies the simulation accuracy, discusses the various parameters used in the test simulations, and presents a test matrix. Chapter V examines the performance of the MAP estimator in simulation and finally, Chapter VI summarizes the thesis.

II. Imaging theory and wavefront sensor simulation development

2.1 Introduction

The purpose of this research was to develop a computer simulation for a Hartmann wavefront sensor and use it to evaluate the performance of a maximum *a-posteriori* (MAP) slope estimator. While the previous chapter presented a basic overview of the area of interest, the material in this chapter is focused on the wavefront sensor. A theoretical foundation for using a linear systems approach to model the imaging process of a single lens system and the operation of the Hartmann wavefront sensor are explained. Then, the computer simulation of the Hartmann wavefront sensor will be discussed in detail.

2.2 Image formation

Light propagating in a source free media system can be analyzed as a linear, space-invariant (LSI) system using Fourier optics theory [12]. Using the LSI framework, the single lens imaging system with an image plane located one focal length away pictured in Fig. 2.1 will produce an intensity distribution that is the magnitude squared of the Fourier transform of the wavefront in the aperture.

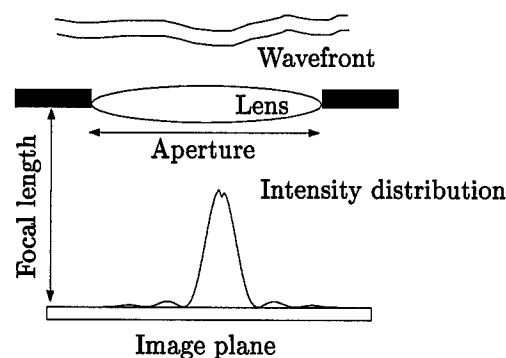


Figure 2.1 Fourier optics approach to imaging with a single lens.

In an actual imaging system, both the wavefront in the pupil and the intensity distribution on the detector are continuous. In order to implement the imaging process in simulation, the

wavefront must be represented using a finite number of samples. Representing a continuous function with a finite number of samples makes the imaging simulation a discrete process, and a Fast Fourier Transform (FFT) of the wavefront in the pupil must be used in order to determine the intensity distribution on the image plane. Two problems must be considered when working in the discrete domain: wrap around error and aliasing due to under-sampling [21]. In order to avoid problems associated with wrap around error when taking FFTs, the wavefronts are placed in a zero-padded array before transforming. The problem of under-sampling is handled by ensuring the wavefront sampling is larger-than or equal-to the sampling that is used by the phase screen generation program [30].

2.3 Image detection

Each subaperture in the wavefront sensor uses an array of charged coupled device (CCD) pixels to detect the intensity distribution that forms on the image plane. The CCD array detects the intensity distribution by counting the arrival of photons at each pixel location. Since photons arrive at random intervals, the detection process can not be treated as deterministic. In addition to a random arrive rate, the detection process is subject to several sources of random noise including background noise and readout noise [26].

2.3.1 Shot noise. Shot noise is another term for photo-conversion noise. It accounts for the uncertainty in the detection of photons. Photons arrive at a random rate and at random locations on the detector array which was modeled by a Poisson process. A Poisson process has a variance equal to its mean making it a signal dependent process. Since shot noise is signal dependent, it is the limiting factor in the detection process [28]. The best centroid estimation in the presence of shot noise is referred to as shot limited performance and is the Cramer-Rao lower bound for any unbiased shift estimator [32].

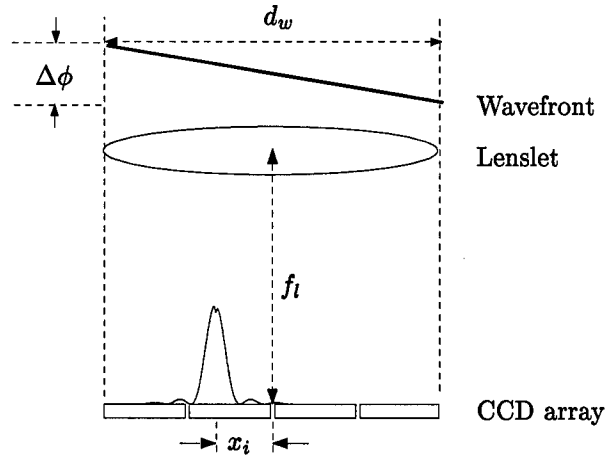


Figure 2.2 Geometry for a single subaperture of a Hartmann wavefront sensor.

2.3.2 Read noise. While the detection of the photons by the CCD pixels is modeled with a signal dependent random process, the act of reading this data contributes to the uncertainty by adding more random noise. A charge coupled device array operates by counting the arrival of photons in each pixel over a given period of time. At the end of each time period, the photon count is read out of the detector array. The random noise resulting from the read out process is referred to as readout noise and is modeled with an additive zero mean Gaussian random process [26].

2.4 Hartmann wavefront sensor

The Hartmann wavefront sensor consists of an array of lenslets or subapertures. The incident wavefront in the aperture of the imaging system is segmented over the array of subapertures. The lenslet in each subaperture forms an intensity distribution onto an array of CCD pixels located at the lenslet focal length. The intensity distribution formed by each lenslet is detected by an array of CCD pixels, and the centroid shift can be estimated for each subaperture. The estimated centroid shift data can be used to calculate the slope of the wavefront in the aperture of the imaging system. Referring to the diagram in Fig. 2.2, the slope of the wavefront in the i th subaperture, \vec{s}_i , can be

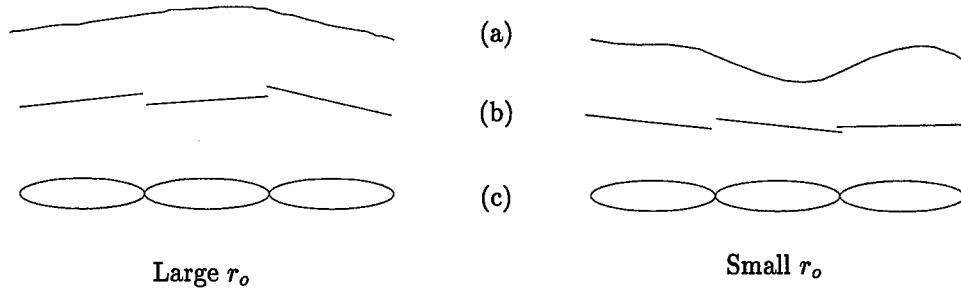


Figure 2.3 The wavefront in the aperture (a) and its piecewise linear approximation (b) across an array of subapertures (c) for different values of the Fried parameter, r_o .

determined using two relationships. First, the slope is proportional to the centroid shift, \bar{x}_i [3]:

$$\vec{s}_i = k \frac{\bar{x}_i}{f_l} \quad \left(\frac{\text{radians}}{\text{meter}} \right), \quad (2.1)$$

where $k = 2\pi/\lambda$, λ is the average wavelength, and f_l is the subaperture focal length. Secondly, the slope of the wavefront in the subaperture can be found using a relationship developed by Wallner [28],

$$\vec{s}_i = - \int d\vec{x} \nabla W_i(\vec{x}) \phi(\vec{x}) \quad \left(\frac{\text{radians}}{\text{meter}} \right), \quad (2.2)$$

where $\nabla W_i(\vec{x})$ is the gradient of the subaperture weighting function of the i th subaperture, and $\phi(\vec{x})$ is the wavefront phase in the i th subaperture. It should be noted that the expressions defined in Eqn. (2.1) approximates the wavefront slope as linear in the subaperture. Since the Hartmann wavefront sensor is an array of subapertures, the wavefront in the aperture of the imaging system is averaged in a piecewise linear fashion [14]. When the Fried parameter, r_o , is large, the linear approximation holds. However, as r_o decreases, the linear approximation will not be valid as the spatially averaged wavefront tilt can differ greatly from the true wavefront tilt as shown in Fig. 2.3.

2.5 Hartmann wavefront sensor simulation

In order to develop a simulation for the Hartmann wavefront sensor, the operation must be broken up into several steps. The approach taken to model the operation of the Hartmann wavefront sensor was similar to one described by Cannon [3] in which the incident wavefront was segmented over an array of microlenses and FFTs were used to determine the corresponding intensity distributions. A flow chart for the Hartmann wavefront sensor simulation is shown in Fig. 2.4. The simulation input is a phase screen, and the outputs are vectors containing the actual centroid shifts (\mathbf{x}_{act}) and the wavefront sensor shift estimates ($\hat{\mathbf{x}}_{est}$). The actual centroid shift can be calculated in the simulation only because the actual phase data is available. An actual wavefront sensor can only estimate the centroid shift based upon the detected signal values. The difference between the actual centroid shift and the estimated centroid shift is the estimation error. The simulation segments the incident wavefront over an array of subapertures, calculates the actual centroid shifts, calculates the intensity distribution on the detector array, accounts for shot noise, read noise, and overlap onto adjacent detectors, then estimates the centroid shifts.

The major steps of the wavefront sensor simulation are described in detail below:

- The incident wavefront is of uniform amplitude and varying phase. The phase of the wavefront is the input to the simulation. The phase data, or phase screen, of the incident wavefront is segmented over the wavefront sensor subaperture array. The actual centroid shift is then calculated for each subaperture. Using Eqns. (2.1) and (2.2), the actual centroid shift, \vec{x}_{act} , is:

$$\vec{x}_{act} = -\frac{f_l}{k} \int d\vec{x} \nabla W_i(\vec{x}) \phi(\vec{x}), \quad (2.3)$$

where f_l is the subaperture focal length, $W_i(\vec{x})$ is the subaperture weighting function of the i th subaperture, $k = 2\pi/\lambda$, and $\phi(\vec{x})$ is the wavefront phase in the i th subaperture. Since the wavefront sensor subapertures are assumed square in the simulation, the subaperture weighting function,

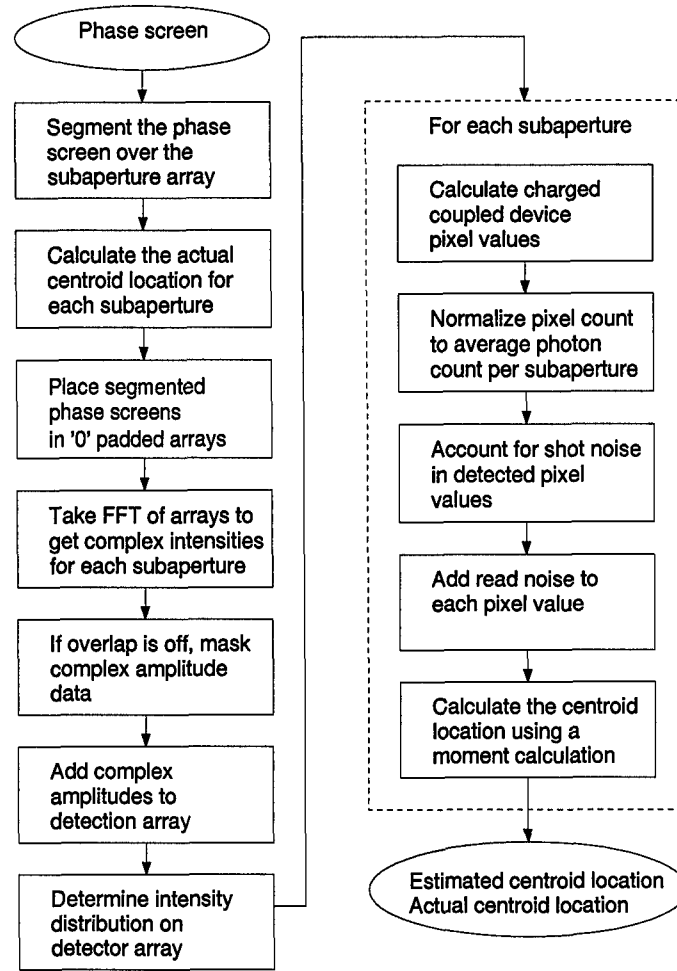


Figure 2.4 Flow chart for the Hartmann wavefront sensor simulation

$W_i(x, y)$, for all subapertures can be modeled as:

$$W_i(x, y) = \frac{1}{d_w^2} \text{rect}\left(\frac{x}{d_w}\right) \text{rect}\left(\frac{y}{d_w}\right), \quad (2.4)$$

where d_w is the width of the wavefront sensor subaperture, and

$$\text{rect}\left(\frac{x}{d_w}\right) = \begin{cases} 1 & -\frac{d_w}{2} \leq x \leq \frac{d_w}{2} \\ 0 & \text{otherwise.} \end{cases} \quad (2.5)$$

Using the definition of the gradient operator, $\nabla = \frac{\partial}{\partial x}\hat{x} + \frac{\partial}{\partial y}\hat{y}$, the gradient of the subaperture weighting function is

$$\begin{aligned}
 \nabla W_i(x, y) &= \frac{\partial}{\partial x} W_i(x, y) \hat{x} + \frac{\partial}{\partial y} W_i(x, y) \hat{y} \\
 &= \frac{\partial}{\partial x} \left[\frac{1}{d_w^2} \text{rect}\left(\frac{x}{d_w}\right) \text{rect}\left(\frac{y}{d_w}\right) \right] \hat{x} + \frac{\partial}{\partial y} \left[\frac{1}{d_w^2} \text{rect}\left(\frac{x}{d_w}\right) \text{rect}\left(\frac{y}{d_w}\right) \right] \hat{y} \\
 &= \frac{1}{d_w^2} \left(\delta\left(x + \frac{d_w}{2}\right) - \delta\left(x - \frac{d_w}{2}\right) \right) \text{rect}\left(\frac{y}{d_w}\right) \hat{x} \\
 &\quad + \frac{1}{d_w^2} \left(\delta\left(y + \frac{d_w}{2}\right) - \delta\left(y - \frac{d_w}{2}\right) \right) \text{rect}\left(\frac{x}{d_w}\right) \hat{y}.
 \end{aligned} \tag{2.6}$$

Now, Eqn. (2.3) can be written in an expanded form by substituting Eqn. (2.6) for the gradient of the subaperture weighting function:

$$\begin{aligned}
 \vec{x}_{act} &= -\frac{f_l}{k d_w^2} \iint dx dy \left[\left(\delta\left(x + \frac{d_w}{2}\right) - \delta\left(x - \frac{d_w}{2}\right) \right) \phi(x, y) \text{rect}\left(\frac{y}{d_w}\right) \hat{x} \right. \\
 &\quad \left. + \left(\delta\left(y + \frac{d_w}{2}\right) - \delta\left(y - \frac{d_w}{2}\right) \right) \phi(x, y) \text{rect}\left(\frac{x}{d_w}\right) \hat{y} \right].
 \end{aligned} \tag{2.7}$$

An expression for the actual centroid shift can be found by using the sifting property of Dirac delta functions [12]:

$$\vec{x}_{act} = \frac{f_l}{k d_w^2} \left[\int dy \left(\phi\left(\frac{d_w}{2}, y\right) - \phi\left(-\frac{d_w}{2}, y\right) \right) \hat{x} + \int dx \left(\phi\left(x, \frac{d_w}{2}\right) - \phi\left(x, -\frac{d_w}{2}\right) \right) \hat{y} \right]. \tag{2.8}$$

Consider only one of the two orthogonal directions. The x_{act} value in the \hat{x} direction can be written as

$$x_{act} = \frac{f_l}{k d_w} \left[\frac{\int dy \phi\left(\frac{d_w}{2}, y\right)}{d_w} - \frac{\int dy \phi\left(-\frac{d_w}{2}, y\right)}{d_w} \right] \hat{x}. \tag{2.9}$$

Integrating the phase with respect to y and dividing by the width of the subaperture results in the average phase value at the points $x \pm \frac{d_w}{2}$. The difference between the average phase at these two points scaled by f_l/kd_w is the actual shift in the \hat{x} direction. In the discrete domain, the actual shift can be found in a similar manner. In order to determine the average phase value at the points $x \pm \frac{d_w}{2}$, the phase samples are summed in the \hat{y} direction at the points $x \pm \frac{d_w}{2}$ and divided by the total number of samples. The difference between the average phase at these two points scaled by f_l/kd_w is the actual shift in the \hat{x} direction:

$$x_{act} = \frac{f_l}{kd_w} \left[\frac{\sum_{y=1}^N \phi\left(\frac{d_w}{2}, y\right)}{N} - \frac{\sum_{y=1}^N \phi\left(-\frac{d_w}{2}, y\right)}{N} \right] \hat{x}. \quad (2.10)$$

The discrete form of Eqn. (2.8) can be written as

$$\begin{aligned} \vec{x}_{act} = \frac{f_l}{kd_w} & \left[\frac{\sum_{y=1}^N \phi\left(\frac{d_w}{2}, y\right)}{N} - \frac{\sum_{y=1}^N \phi\left(-\frac{d_w}{2}, y\right)}{N} \right] \hat{x} \\ & + \left[\frac{\sum_{x=1}^N \phi\left(x, \frac{d_w}{2}\right)}{N} - \frac{\sum_{x=1}^N \phi\left(x, -\frac{d_w}{2}\right)}{N} \right] \hat{y}, \end{aligned} \quad (2.11)$$

where N^2 is the total number of samples in the phase screen, f_l is the subaperture focal length, $k = 2\pi/\lambda$, and d_w is the width of the wavefront sensor subaperture.

- After the actual centroid shifts have been calculated for each subaperture, the estimated centroid shifts are determined. The first step is to zero-pad each segmented piece of the phase screen in order to minimize the effects of wrap around when the FFT is taken [21]. The zero-padding is accomplished by resizing the segmented piece of the phase screen to 15×15 samples. Based upon the selected atmospheric parameters, the sampling of the phase screens generated by the phase screen generator [30] is less than 15×15 samples. Resizing to a larger number of samples ensures no loss of data or aliasing due to under-sampling. The phase screen data is placed into a 15×15

array centered on a larger 64×64 array containing 0 values. A 64×64 array is used to take advantage of FFT algorithms.

- At this point in the simulation, the phase screen in each subaperture has been placed into a larger zero-padded array. The next step is to take the FFT of each zero-padded array. The resulting arrays contain complex amplitude data for each subaperture. As shown in Fig. 2.5, all of the complex amplitude data is added to a single detection array. Since the simulation was designed such that the physical size of the arrays containing the complex amplitude data was larger than the physical size of the subaperture, the complex amplitude data for adjacent subapertures will overlap when added to the detection array. However, if overlap between subapertures is not allowed, an overlap mask is placed over the array containing the complex amplitude data, nulling all amplitude data in the overlap region. Assigning all of the amplitude values in the overlap region to zero will negate the effect of overlap on the detection array.

- After all of the complex amplitudes are added to the detector array, the detector array is multiplied by its complex conjugate to determine the intensity distribution on the detector plane.

- Figure 2.6 shows that the detection array contains the intensity distributions formed by all of the subapertures. At this point in the simulation, the detection of the intensity distribution by the CCD array is modeled. In an actual wavefront sensor, each subaperture contains an $N \times N$ array of CCD detector pixels located in the image plane. In the simulation, N is a user defined parameter. The CCD array is modeled as a square array of pixels with no spacing between them. To account for the effects dead space between the detector pixels in an actual CCD array, the photon count can be scaled by a user defined duty cycle parameter. The intensity distribution corresponding to each subaperture is sampled into an $N \times N$ CCD array. The sum of the values in each subaperture CCD array is normalized to equal the average photon count per subaperture, \bar{K} . The CCD array for each subaperture now contains the normalized detected signal values.

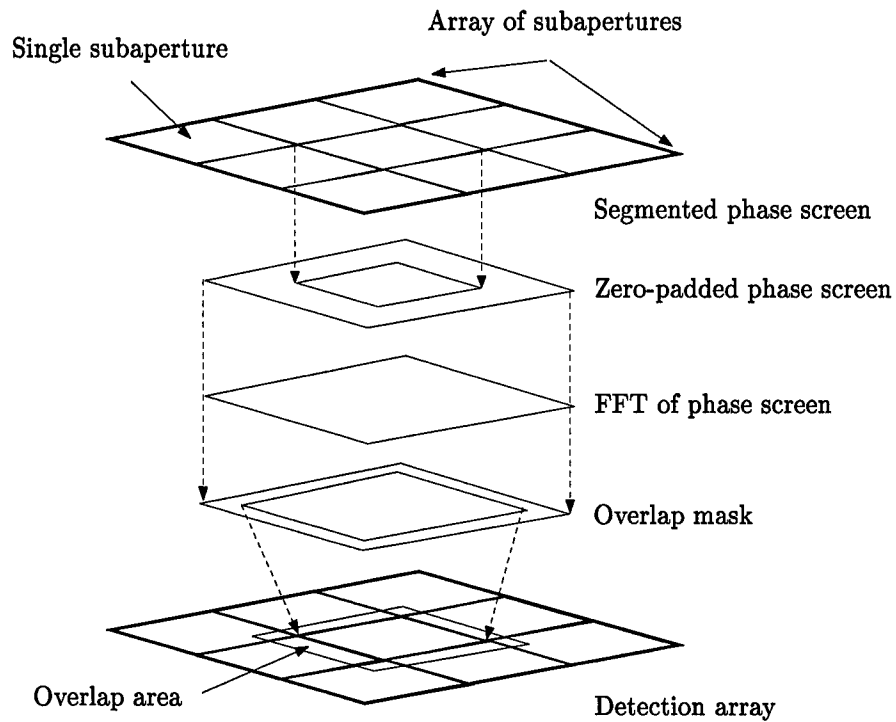


Figure 2.5 The wavefront is segmented over an array of subapertures. The individual segments are placed in zero-padded arrays. The FFT is taken to get the complex amplitude data, an overlap mask is placed on the data, then the data is added to a detection array.

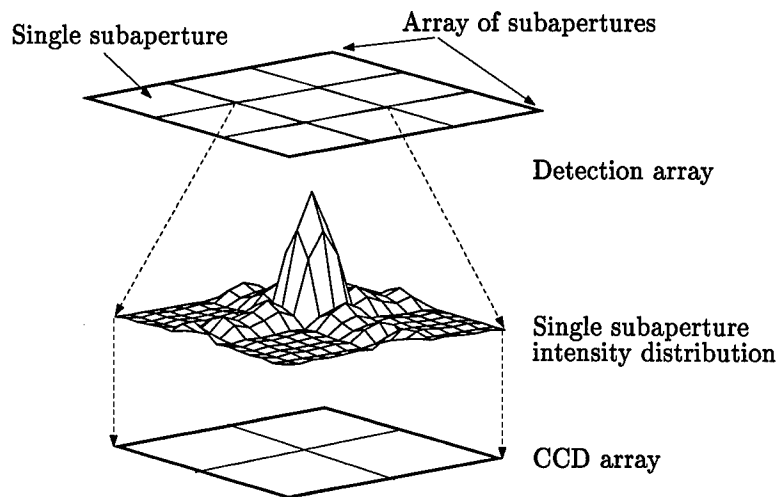


Figure 2.6 The intensity distribution for each subaperture is sampled into a smaller CCD array.

- The detection process by a CCD is subject to shot and read noise. To account for the uncertainty of the detection process, each value in the CCD arrays is subjected to a Poisson process. The CCD arrays now contain shot limited detected values. The shot limited detected values in the CCD arrays are then subjected to an additive Gaussian zero mean process to account for the effects of read noise. The variance of the read noise is another user defined parameter.

- Now that the CCD arrays contain the detected signal values, the estimated centroid shift can be calculated. For a detector array with a finite number of pixels, the centroid shift estimates for each subaperture, \vec{m} , are calculated using a first moment calculation [4],

$$\vec{m} = \frac{\sum_i \sum_j x_i P_{ij}}{\sum_i \sum_j P_{ij}} \hat{x} + \frac{\sum_j \sum_i y_j P_{ij}}{\sum_i \sum_j P_{ij}} \hat{y}, \quad (2.12)$$

where P_{ij} is the photon count in the (i, j) pixel of the subaperture detection array, and x_i and y_j are the offsets from the center of the subaperture to the center of the i th or j th pixel.

2.6 Using the wavefront sensor simulation

The wavefront sensor simulation is set up as a MATLAB 5.0[©] function call. The code listing in Appendix D is called using the following command:

```
function [xest,xact] = wfs1(PhaseScreen, SubapertureArraySize, SubapertureFocalLength,
SubapertureDiameter, AverageWavelength, DetectorArraySize, ReadNoiseVariance, ShotNoise,
AveragePhotonCount, WavefrontTilt, DetectorDutyCycle, SubapertureOverlap)
```

The wavefront sensor simulation was designed to allow the following parameters to be varied:

- PhaseScreen - The phase data of the incident wavefront in the aperture of the imaging system.

- SubapertureArraySize - The square root of the number of subapertures in the wave front sensor array. The simulation assumes a square array of subapertures.
- SubapertureFocalLength - The focal length in meters.
- SubapertureDiameter - The diameter of the subaperture in meters.
- AverageWavelength - The average wavelength in meters.
- DetectorArraySize - The square root of the number of pixels in each subaperture detector array. The CCD array is assumed square with no dead space between pixels.
- ReadNoiseVariance - The variance for the additive Gaussian noise.
- AveragePhotonCount - The average photon count per subaperture for the sampling period.
- WavefrontTilt - The global tilt on the incident wavefront can be removed to simulate the presence of a tip-tilt mirror in the adaptive optics system.
- DetectorDutyCycle - The duty cycle of the detector array.
- SubapertureOverlap - The intensity can spill over onto adjacent subapertures.

The vector \hat{x}_{est} contains the estimated centroid shifts for all subapertures and the vector x_{act} contains the actual centroid shifts for all subapertures. The format for both the actual centroid shift vector and centroid shift estimate vector follows:

$$x_{act} = \begin{bmatrix} x_{act}(1) \\ y_{act}(1) \\ x_{act}(2) \\ y_{act}(2) \\ \vdots \\ x_{act}(M) \\ y_{act}(M) \end{bmatrix} \quad \text{and} \quad \hat{x}_{est} = \begin{bmatrix} m_{\bar{x}}(1) \\ m_{\bar{y}}(1) \\ m_{\bar{x}}(2) \\ m_{\bar{y}}(2) \\ \vdots \\ m_{\bar{x}}(M) \\ m_{\bar{y}}(M) \end{bmatrix}, \quad (2.13)$$

where $x_{act}(1)$ and $y_{act}(1)$ are the actual \hat{x} and \hat{y} shifts in meters for the first subaperture, $m_{\hat{x}}(1)$ and $m_{\hat{y}}(1)$ are the estimated \hat{x} and \hat{y} shifts in meters for the first subaperture, M is the total number of subapertures in the wavefront sensor array, and the subapertures are numbered sequentially increasing from left to right, top to bottom as depicted in Fig. 2.7.

1	2	3
4	5	6
7	8	9

Figure 2.7 The numbering sequence for the wavefront sensor array.

III. Implementation of a maximum a-posteriori estimator

3.1 Introduction

The Hartmann wavefront sensor estimates the centroid shift of the irradiance distributions in each subaperture. The centroid shift information is then used to estimate the wavefront slope at the pupil of a telescope in order to correct for wavefront distortions caused by atmospheric turbulence. Centroid shift estimation uses a moment calculation and does not take advantage of the correlation properties of the wavefront slopes over the subapertures or the amount of light collected by the wavefront sensor. A MAP estimator derived by Scott Sallberg [23] incorporates statistical knowledge of wavefront slopes and light levels when estimating the centroid shifts. The MAP estimator was found to be unbiased and the MSE performance of the centroid estimator was its upper bound. This chapter will present an overview of the MAP estimator, develop the equations necessary to implement the estimator in simulation, and evaluate the theoretical performance limits of the estimator.

3.2 Maximum a-posteriori estimator

The MAP estimator derived by Sallberg [23] determines the MAP shift estimate vector (\hat{x}_{MAP}) by scaling the centroid shift estimate vector (\hat{x}_{est}) by a correction factor matrix C^{-1} :

$$\hat{x}_{MAP} = C^{-1} \hat{x}_{est}, \quad (3.1)$$

where the correction factor, C^{-1} , is defined [23] as

$$C^{-1} = \left[I - \left(I + \frac{1}{\sigma_p^2} RK \right)^{-1} \right]. \quad (3.2)$$

I is the identity matrix, R is the slope correlation matrix, σ_p^2 is the mean square spot size, and K is the photon count matrix defined as

$$K = \begin{bmatrix} K_1 & & 0 \\ & \ddots & \\ 0 & & K_j \end{bmatrix}, \quad (3.3)$$

where K_j is a diagonal matrix containing the photon count in the j th subaperture.

3.3 Slope correlation

In order to develop a simulation for the MAP estimator, the slope correlation matrix R must be calculated. The goal of the next three sections is to derive the equations needed in order to calculate slope correlation matrices for the desired atmospheric statistics and subaperture array size. Referencing Fig. 3.1, a general solution will be developed to find slope correlations between any two subapertures separated by a distance $\vec{D} = \sqrt{x_o^2 + y_o^2}$ where x_o and y_o are the \hat{x} and \hat{y} distances between any two subapertures.

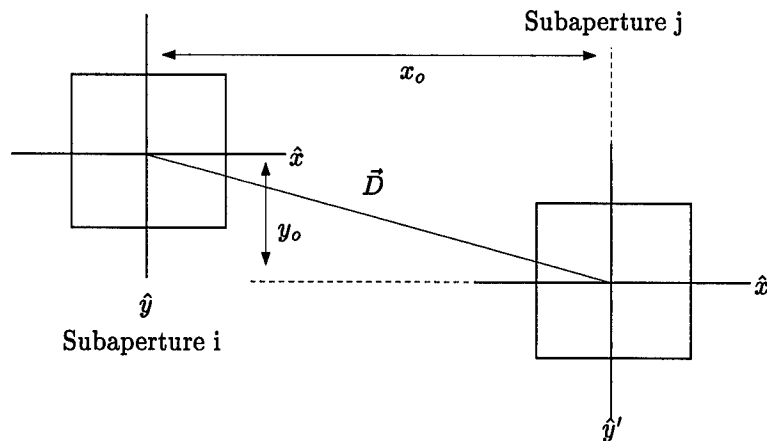


Figure 3.1 The slope correlation generalized for any two subapertures separated by a distance \vec{D} . The coordinate reference is centered on the subapertures with positive directions labeled.

The slope correlation equations are developed by first defining the slope in the subaperture as a function of the subaperture weighting function $W_i(\vec{x})$ and the phase in the subaperture $\phi(\vec{x})$. The wavefront slope for the i th subaperture can be shown to be equivalent to computing the average wavefront phase gradient over the wavefront sensor subaperture [33]:

$$s_i = \int d\vec{x} W_i(\vec{x}) (\nabla \phi(\vec{x}) \cdot \vec{d}_i), \quad (3.4)$$

where \vec{d}_i is a unit vector designating one of two orthogonal slope components for the i th subaperture and the subaperture weighting function, $W_i(\vec{x})$, is normalized such that

$$\int d\vec{x} W_i(\vec{x}) = 1. \quad (3.5)$$

Integrating Eqn. (3.4) by parts [28] allows the slope to be expressed in terms of $\phi(\vec{x})$ rather than $\nabla \phi(\vec{x})$:

$$s_i = - \int d\vec{x} (\nabla W_i(\vec{x}) \cdot \vec{d}_i) \phi(\vec{x}). \quad (3.6)$$

The slope correlation between any two subapertures i and j , R_{ij} , is the expected value of the product of the slopes in the two subapertures [22]:

$$\begin{aligned} R_{ij} &= E[s_i s_j], \\ &= \int \int d\vec{x}' d\vec{x} (\nabla W_i(\vec{x}') \cdot \vec{d}_i) (\nabla W_j(\vec{x}) \cdot \vec{d}_j) E\{\phi(\vec{x}') \phi(\vec{x})\}, \end{aligned} \quad (3.7)$$

where $s(i)$ is the i th subaperture slope measurement in the \vec{d}_i direction and $E[\cdot]$ is the expected value operator.

Given the wavefront phase correlation $\Gamma_\phi(\vec{x}' - \vec{x}) = E\{\phi(\vec{x}')\phi(\vec{x})\}$ and the definition of the structure function [11]:

$$D_\phi(\vec{x}' - \vec{x}) = 2\Gamma_\phi(\vec{x}' - \vec{x}) - 2\Gamma_\phi(0, 0), \quad (3.8)$$

the slope correlation can now be written as

$$R_{ij} = \int \int d\vec{x}' d\vec{x} (\nabla W_i(\vec{x}') \cdot \vec{d}_i) (\nabla W_j(\vec{x}) \cdot \vec{d}_j) \left(\Gamma_\phi(0, 0) - \frac{1}{2} D_\phi(\vec{x}' - \vec{x}) \right). \quad (3.9)$$

Using the definition of the subaperture weighting function from Eqn. (2.4), the gradient of the weighting function was found to be

$$\begin{aligned} \nabla W_i(x, y) = & \frac{1}{d^2} \left(\delta\left(x + \frac{d}{2}\right) - \delta\left(x - \frac{d}{2}\right) \right) \text{rect}\left(\frac{y}{d}\right) \hat{x} \\ & + \frac{1}{d^2} \left(\delta\left(y + \frac{d}{2}\right) - \delta\left(y - \frac{d}{2}\right) \right) \text{rect}\left(\frac{x}{d}\right) \hat{y}, \end{aligned} \quad (3.10)$$

where d is the telescope subaperture diameter. The telescope subaperture diameter is used in this formulation since the slope correlation values will be calculated across the aperture of the telescope.

Equations to calculate the slope correlation between any two subapertures can now be developed using Eqns. (3.9) and (3.10). It should be noted that the slope correlation, R_{ij} , is dependent on the separation of the i th and j th subapertures, x_o and y_o , and the slope components, \vec{d}_i and \vec{d}_j ,

in each subaperture. Using the notation $R_{ij} = R(x_o, y_o)$ we have,

$$\begin{aligned}
 R_{ij} = & \int \int \int \int dx dx' dy dy' \\
 & \times \left[\left(\frac{1}{d^2} \left(\delta \left(x + \frac{d}{2} \right) - \delta \left(x - \frac{d}{2} \right) \right) \text{rect} \left(\frac{y}{d} \right) \hat{x} \cdot \vec{d}_i \right) \right. \\
 & \left. + \left(\frac{1}{d^2} \left(\delta \left(y + \frac{d}{2} \right) - \delta \left(y - \frac{d}{2} \right) \right) \text{rect} \left(\frac{x}{d} \right) \hat{y} \cdot \vec{d}_i \right) \right] \\
 & \times \left[\left(\frac{1}{d^2} \left(\delta \left(x' + \frac{d}{2} - x_o \right) - \delta \left(x' - \frac{d}{2} - x_o \right) \right) \text{rect} \left(\frac{y' - y_o}{d} \right) \hat{x} \cdot \vec{d}_j \right) \right. \\
 & \left. + \left(\frac{1}{d^2} \left(\delta \left(y' + \frac{d}{2} - y_o \right) - \delta \left(y' - \frac{d}{2} - y_o \right) \right) \text{rect} \left(\frac{x' - x_o}{d} \right) \hat{y} \cdot \vec{d}_j \right) \right] \\
 & \times \left(\Gamma_\phi(0, 0) - \frac{1}{2} D_\phi(x' - x, y' - y) \right). \tag{3.11}
 \end{aligned}$$

3.4 Slope correlation matrix development

Before specific equations can be developed to complete the correlation matrix, some book-keeping information must be presented. The form of \mathbf{R} is defined by the ordering of the elements of \mathbf{s} , the vector containing the subaperture wavefront slopes:

$$\mathbf{s} = \begin{bmatrix} s_1 \\ s_2 \\ s_3 \\ s_4 \\ \vdots \\ s_{2M^2-1} \\ s_{2M^2} \end{bmatrix}, \tag{3.12}$$

where s_1 is the \hat{x} directed slope for the 1st subaperture (upper left in Fig. 3.2) and s_2 is the \hat{y} directed slope for the 1st subaperture. Since the array of subapertures is $M \times M$, with each subaperture having an \hat{x} and \hat{y} directed slope measurement, \mathbf{s} will have $2M^2$ elements. The slope

correlation matrix, \mathbf{R} is defined as $E[\mathbf{s}\mathbf{s}^T]$. The slope correlation matrix will be of size $2M^2 \times 2M^2$ and will have the following form:

$$\mathbf{R} = E \begin{bmatrix} s_1 s_1 & s_1 s_2 & \dots & s_1 s_{2M^2} \\ s_2 s_1 & s_2 s_2 & \dots & s_2 s_{2M^2} \\ s_3 s_1 & s_3 s_2 & \dots & s_3 s_{2M^2} \\ s_4 s_1 & s_4 s_2 & \dots & s_4 s_{2M^2} \\ \vdots & \vdots & \ddots & \vdots \\ s_{2M^2-1} s_1 & s_{2M^2-1} s_2 & \dots & s_{2M^2-1} s_{2M^2} \\ s_{2M^2} s_1 & s_{2M^2} s_2 & \dots & s_{2M^2} s_{2M^2} \end{bmatrix}. \quad (3.13)$$

Referring to Fig. 3.2 and Eqn. (3.13), calculating the values for \mathbf{R} requires the development of four different equations:

1. Correlation between two subapertures with \hat{x} directed slopes.
2. Correlation between two subapertures with \hat{y} directed slopes.
3. Correlation between subapertures with \hat{x} and \hat{y} directed slopes.
4. Correlation between subapertures with \hat{y} and \hat{x} directed slopes.

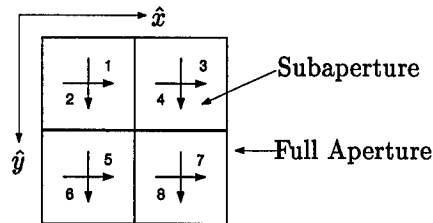


Figure 3.2 Subaperture slope geometry. The numbering depicts orthogonal components of the slope measurements.

3.5 Slope correlation equations

Equation (3.11) is further developed for specific atmospheric structure functions in Appendices A and B. Appendix A develops the slope correlation using Kolmogorov statistics. Appendix B develops the slope correlation using von Karman statistics. The following is a summary of the equations obtained using the two different structure functions.

3.5.1 Kolmogorov turbulence statistics. Using the Kolmogorov structure function the correlation between \hat{x} directed slopes is

$$R_{xx}(\tilde{x}_o, \tilde{y}_o) = \frac{-3.44}{d^2} \left(\frac{d}{r_o} \right)^{\frac{5}{3}} \int_{\tilde{y}_o-1}^{\tilde{y}_o+1} d\Delta_y (1 - |\Delta_y - \tilde{y}_o|) \times \left[2(\tilde{x}_o^2 + \Delta_y^2)^{\frac{5}{6}} - ((\tilde{x}_o + 1)^2 + \Delta_y^2)^{\frac{5}{6}} - ((\tilde{x}_o - 1)^2 + \Delta_y^2)^{\frac{5}{6}} \right], \quad (3.14)$$

where $\tilde{x}_o = x_o/d$ and $\tilde{y}_o = y_o/d$ are the normalized subaperture separations and r_o is the Fried parameter. The correlation between \hat{y} directed slopes is

$$R_{yy}(\tilde{x}_o, \tilde{y}_o) = \frac{-3.44}{d^2} \left(\frac{d}{r_o} \right)^{\frac{5}{3}} \int_{\tilde{x}_o-1}^{\tilde{x}_o+1} d\Delta_x (1 - |\Delta_x - \tilde{x}_o|) \times \left[2(\tilde{y}_o^2 + \Delta_x^2)^{\frac{5}{6}} - ((\tilde{y}_o + 1)^2 + \Delta_x^2)^{\frac{5}{6}} - ((\tilde{y}_o - 1)^2 + \Delta_x^2)^{\frac{5}{6}} \right]. \quad (3.15)$$

The correlation between \hat{x} and \hat{y} directed slopes is

$$R_{xy}(\tilde{x}_o, \tilde{y}_o) = \frac{-3.44}{d^2} \left(\frac{d}{r_o} \right)^{\frac{5}{3}} \int_{-\frac{1}{2}}^{\frac{1}{2}} \int_{\tilde{y}_o-\frac{1}{2}}^{\tilde{y}_o+\frac{1}{2}} dy dx \left[\left(\left(y + \frac{1}{2} \right)^2 + \left(-\frac{1}{2} + \tilde{x}_o - x \right)^2 \right)^{\frac{5}{6}} - \left(\left(y + \frac{1}{2} \right)^2 + \left(\frac{1}{2} + \tilde{x}_o - x \right)^2 \right)^{\frac{5}{6}} - \left(\left(y - \frac{1}{2} \right)^2 + \left(-\frac{1}{2} + \tilde{x}_o - x \right)^2 \right)^{\frac{5}{6}} + \left(\left(y - \frac{1}{2} \right)^2 + \left(\frac{1}{2} + \tilde{x}_o - x \right)^2 \right)^{\frac{5}{6}} \right]. \quad (3.16)$$

The correlation between \hat{y} and \hat{x} directed slopes is

$$R_{yx}(\tilde{x}_o, \tilde{y}_o) = \frac{-3.44}{d^2} \left(\frac{d}{r_o} \right)^{\frac{5}{6}} \int_{-\frac{1}{2}}^{\frac{1}{2}} \int_{\tilde{x}_o - \frac{1}{2}}^{\tilde{x}_o + \frac{1}{2}} dx dy \left[\left(\left(x + \frac{1}{2} \right)^2 + \left(-\frac{1}{2} + \tilde{y}_o - y \right)^2 \right)^{\frac{5}{6}} \right. \\ \left. - \left(\left(x + \frac{1}{2} \right)^2 + \left(\frac{1}{2} + \tilde{y}_o - y \right)^2 \right)^{\frac{5}{6}} - \left(\left(x - \frac{1}{2} \right)^2 + \left(-\frac{1}{2} + \tilde{y}_o - y \right)^2 \right)^{\frac{5}{6}} \right. \\ \left. + \left(\left(x - \frac{1}{2} \right)^2 + \left(\frac{1}{2} + \tilde{y}_o - y \right)^2 \right)^{\frac{5}{6}} \right]. \quad (3.17)$$

3.5.2 von Karman turbulence statistics. Similar relationships were found for the von Karman structure function. The correlation between \hat{x} directed slopes is

$$R_{xx}(\tilde{x}_o, \tilde{y}_o) = 0.08663 \left(\frac{L_o}{r_o} \right)^{\frac{5}{6}} \frac{1}{d^2} \left(\frac{\Gamma[1/6]}{\pi^{\frac{1}{6}}} \right) \int_{\tilde{y}_o - 1}^{\tilde{y}_o + 1} d\Delta_y (1 - |\Delta_y - \tilde{y}_o|) \\ \times \left[2 \left(\frac{d\sqrt{\tilde{x}_o^2 + (\Delta_y)^2}}{L_o} \right)^{\frac{5}{6}} K_{5/6} \left[2\pi \frac{d\sqrt{\tilde{x}_o^2 + (\Delta_y)^2}}{L_o} \right] \right. \\ \left. - \left(\frac{d\sqrt{(\tilde{x}_o + 1)^2 + (\Delta_y)^2}}{L_o} \right)^{\frac{5}{6}} K_{5/6} \left[2\pi \frac{d\sqrt{(\tilde{x}_o + 1)^2 + (\Delta_y)^2}}{L_o} \right] \right. \\ \left. - \left(\frac{d\sqrt{(\tilde{x}_o - 1)^2 + (\Delta_y)^2}}{L_o} \right)^{\frac{5}{6}} K_{5/6} \left[2\pi \frac{d\sqrt{(\tilde{x}_o - 1)^2 + (\Delta_y)^2}}{L_o} \right] \right], \quad (3.18)$$

where $\tilde{x}_o = x_o/d$ and $\tilde{y}_o = y_o/d$ are the normalized subaperture separations and r_o is the Fried parameter. The correlation between \hat{y} directed slopes:

$$R_{yy}(\tilde{x}_o, \tilde{y}_o) = 0.08663 \left(\frac{L_o}{r_o} \right)^{\frac{5}{6}} \frac{1}{d^2} \left(\frac{\Gamma[1/6]}{\pi^{\frac{1}{6}}} \right) \int_{\tilde{x}_o - 1}^{\tilde{x}_o + 1} d\Delta_x (1 - |\Delta_x - \tilde{x}_o|) \\ \times \left[2 \left(\frac{d\sqrt{\tilde{y}_o^2 + (\Delta_x)^2}}{L_o} \right)^{\frac{5}{6}} K_{5/6} \left[2\pi \frac{d\sqrt{\tilde{y}_o^2 + (\Delta_x)^2}}{L_o} \right] \right. \\ \left. - \left(\frac{d\sqrt{(\tilde{y}_o + 1)^2 + (\Delta_x)^2}}{L_o} \right)^{\frac{5}{6}} K_{5/6} \left[2\pi \frac{d\sqrt{(\tilde{y}_o + 1)^2 + (\Delta_x)^2}}{L_o} \right] \right. \\ \left. - \left(\frac{d\sqrt{(\tilde{y}_o - 1)^2 + (\Delta_x)^2}}{L_o} \right)^{\frac{5}{6}} K_{5/6} \left[2\pi \frac{d\sqrt{(\tilde{y}_o - 1)^2 + (\Delta_x)^2}}{L_o} \right] \right]. \quad (3.19)$$

The correlation between \hat{x} and \hat{y} directed slopes is

$$\begin{aligned}
R_{xy}(\tilde{x}_o, \tilde{y}_o) = & 0.08663 \left(\frac{L_o}{r_o} \right)^{\frac{5}{3}} \frac{1}{d^2} \left(\frac{\Gamma[1/6]}{\pi^{\frac{1}{6}}} \right) \int_{-\frac{1}{2}}^{\frac{1}{2}} \int_{\tilde{y}_o - \frac{1}{2}}^{\tilde{y}_o + \frac{1}{2}} dy dx \\
& \times \left[- \left(\frac{d\sqrt{(y+\frac{1}{2})^2 + (-\frac{1}{2} + \tilde{x}_o - x)^2}}{L_o} \right)^{\frac{5}{6}} K_{5/6} \left[2\pi \frac{d\sqrt{(y+\frac{1}{2})^2 + (-\frac{1}{2} + \tilde{x}_o - x)^2}}{L_o} \right] \right. \\
& + \left(\frac{d\sqrt{(y+\frac{1}{2})^2 + (\frac{1}{2} + \tilde{x}_o - x)^2}}{L_o} \right)^{\frac{5}{6}} K_{5/6} \left[2\pi \frac{d\sqrt{(y+\frac{1}{2})^2 + (\frac{1}{2} + \tilde{x}_o - x)^2}}{L_o} \right] \\
& + \left(\frac{d\sqrt{(y-\frac{1}{2})^2 + (-\frac{1}{2} + \tilde{x}_o - x)^2}}{L_o} \right)^{\frac{5}{6}} K_{5/6} \left[2\pi \frac{d\sqrt{(y-\frac{1}{2})^2 + (-\frac{1}{2} + \tilde{x}_o - x)^2}}{L_o} \right] \\
& \left. - \left(\frac{d\sqrt{(y-\frac{1}{2})^2 + (\frac{1}{2} + \tilde{x}_o - x)^2}}{L_o} \right)^{\frac{5}{6}} K_{5/6} \left[2\pi \frac{d\sqrt{(y-\frac{1}{2})^2 + (\frac{1}{2} + \tilde{x}_o - x)^2}}{L_o} \right] \right]. \quad (3.20)
\end{aligned}$$

The correlation between \hat{y} and \hat{x} directed slopes is

$$\begin{aligned}
R_{yx}(\tilde{x}_o, \tilde{y}_o) = & 0.08663 \left(\frac{L_o}{r_o} \right)^{\frac{5}{3}} \frac{1}{d^2} \left(\frac{\Gamma[1/6]}{\pi^{\frac{1}{6}}} \right) \int_{-\frac{1}{2}}^{\frac{1}{2}} \int_{\tilde{x}_o - \frac{1}{2}}^{\tilde{x}_o + \frac{1}{2}} dx dy \\
& \times \left[- \left(\frac{d\sqrt{(x+\frac{1}{2})^2 + (-\frac{1}{2} + \tilde{y}_o - y)^2}}{L_o} \right)^{\frac{5}{6}} K_{5/6} \left[2\pi \frac{d\sqrt{(x+\frac{1}{2})^2 + (-\frac{1}{2} + \tilde{y}_o - y)^2}}{L_o} \right] \right. \\
& + \left(\frac{d\sqrt{(x+\frac{1}{2})^2 + (\frac{1}{2} + \tilde{y}_o - y)^2}}{L_o} \right)^{\frac{5}{6}} K_{5/6} \left[2\pi \frac{d\sqrt{(x+\frac{1}{2})^2 + (\frac{1}{2} + \tilde{y}_o - y)^2}}{L_o} \right] \\
& + \left(\frac{d\sqrt{(x-\frac{1}{2})^2 + (-\frac{1}{2} + \tilde{y}_o - y)^2}}{L_o} \right)^{\frac{5}{6}} K_{5/6} \left[2\pi \frac{d\sqrt{(x-\frac{1}{2})^2 + (-\frac{1}{2} + \tilde{y}_o - y)^2}}{L_o} \right] \\
& \left. - \left(\frac{d\sqrt{(x-\frac{1}{2})^2 + (\frac{1}{2} + \tilde{y}_o - y)^2}}{L_o} \right)^{\frac{5}{6}} K_{5/6} \left[2\pi \frac{d\sqrt{(x-\frac{1}{2})^2 + (\frac{1}{2} + \tilde{y}_o - y)^2}}{L_o} \right] \right]. \quad (3.21)
\end{aligned}$$

3.5.3 Implementation. The correlation between subapertures with slopes in the same direction can be calculated using a single numerical integration where as the correlation between subapertures with \hat{x} and \hat{y} directed slopes requires two dimensional numerical integration. The correlation matrix, \mathbf{R} , for the Kolmogorov structure function, once generated, can simply be scaled as the Fried parameter (r_o) and subaperture diameter (d) changes. However, as the outer scale (L_o) and subaperture diameter (d) change in the von Karman structure function, the entire correlation matrix must be recalculated. Also, when calculating the correlation matrix using the von Karman structure function, a series expansion to the second order of the modified Bessel function of the

second kind was used when integrating across the origin. Without a series expansion, numerical integration across the origin results in an infinite value which is a result of $K_{5/6}[0]$ being equal to infinity. The use of a series expansion allowed the cancelation of the term that caused the infinite value. The code for generating the correlation matrices is listed in Appendix E.

3.6 Theoretical MAP estimator performance

In order to verify the correlation matrix was properly developed, the theoretical performance of the MAP estimator will be compared to the values obtained by Sallberg [24]. The behavior of the correction factor matrix will be examined, and the relative mean square error (MSE) performance of the MAP estimator will be examined. The MSE performance will be evaluated using both Kolmogorov statistics and von Karman statistics in the correlation matrix.

3.6.1 Correction factor matrix. First, the correction factor matrix, C^{-1} , will be examined. C^{-1} should have the following properties:

$$C^{-1} = \begin{cases} 0 & \text{as } K \rightarrow 0 \\ I & \text{as } K \rightarrow \infty. \end{cases} \quad (3.22)$$

As the average photon count per subaperture approaches zero, the data cannot be trusted and the correction factor forces the MAP estimate to zero. As the average photon count per subaperture gets very large, the data can be trusted and the correction factor becomes the identity matrix, I , and the MAP estimate is simply the centroid estimate. The behavior of the MAP estimator can be verified by examining the behavior of the correction factor matrix. Mesh plots of the correction factor matrix as defined in Eqn. (3.2) for different photon counts per subaperture (\bar{K}) are shown in Fig. 3.3. As the average photon count per subaperture increases, the correction factor becomes the identity matrix. The trend verifies the expected behavior of the correction factor matrix.

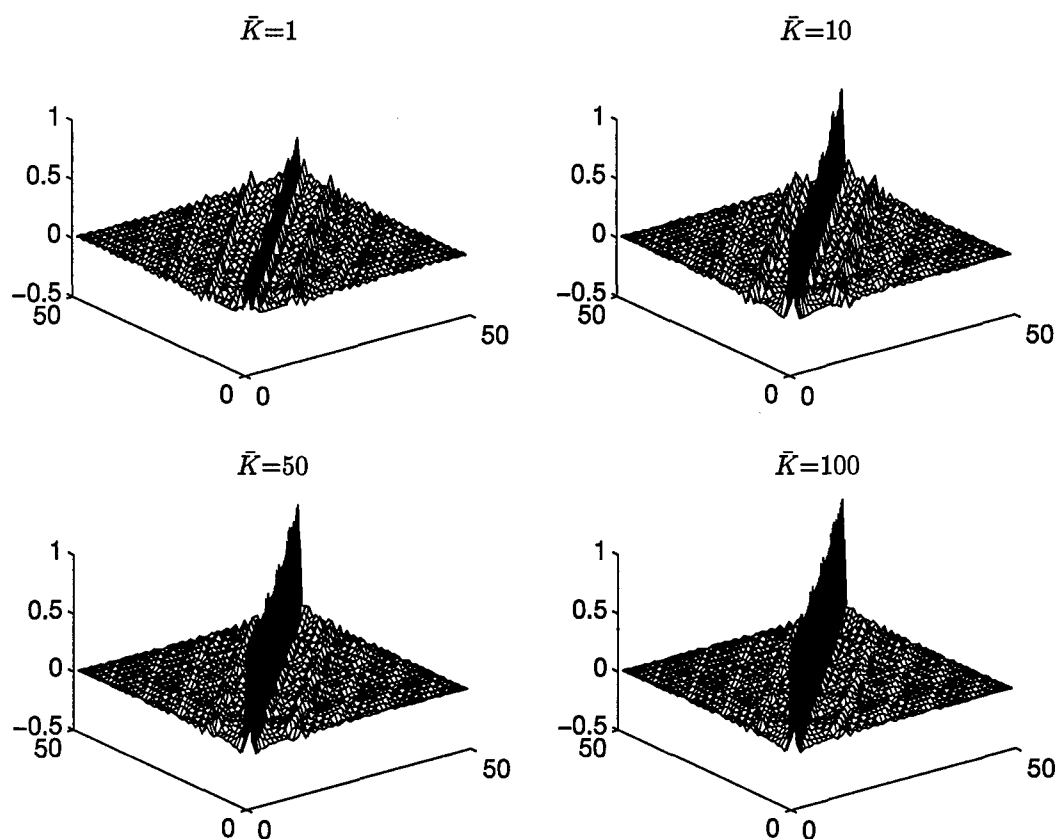


Figure 3.3 Mesh plots of the correction factor matrix for various values of \bar{K} , the average photon count per subaperture, using von Karman statistics to develop the correlation matrix. The subaperture diameter was 9.2cm, the Fried coefficient was 10cm, and the outer scale was 50m.

3.6.2 MAP estimator performance using Kolmogorov statistics. Next, the performance MAP estimator will be examined by comparing the ratio of the MSE of the MAP estimator to the MSE of the centroid estimator. In order to proceed, relationships for the MSE of the centroid estimator and the MAP estimator must be defined. The MSE for the centroid estimator is defined as [24]

$$\text{MSE}(\vec{x}) = \text{tr}[\sigma_p^2 \mathbf{K}^{-1}], \quad (3.23)$$

and the MSE for the MAP estimator is defined as [24]

$$\text{MSE}(\vec{x}) = \text{tr} \left[\left[I - \left(I + \frac{1}{\sigma_p^2} R K \right)^{-1} \right] \sigma_p^2 K^{-1} \right], \quad (3.24)$$

where $\text{tr}[\cdot]$ is the trace operator, R and K are defined by Eqns. (3.13) and (3.3), and σ_p^2 is the mean square spot size.

Figure 3.4 is a plot of the error ratio as a function of average subaperture photon count, \bar{K} , using Kolmogorov statistics in the MAP estimator correlation matrix. The correlation matrix

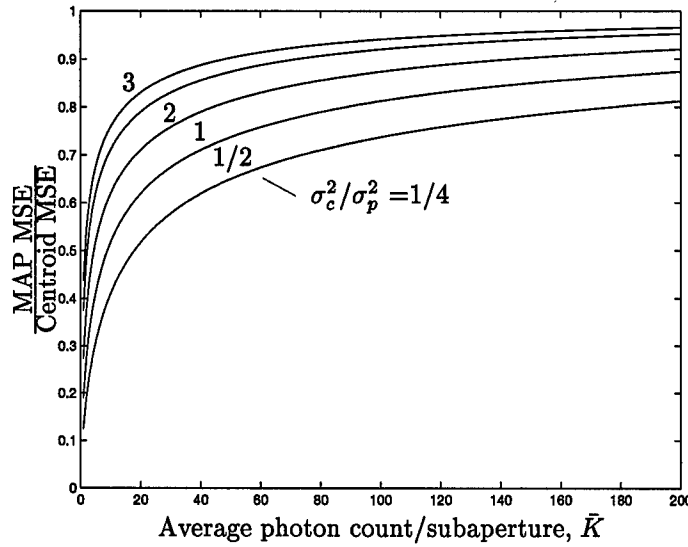


Figure 3.4 Relative MSE performance as a function of average photon count per subaperture. Kolmogorov statistics were used for a 5×5 array of unobscured subapertures with $d = 9.2\text{cm}$.

was computed using Kolmogorov statistics for a 5×5 array of unobscured subapertures with subaperture diameter = 9.2cm. The various curves in each figure correspond to a particular value of the ratio of the mean square spot motion, σ_c^2 , to mean square spot size, σ_p^2 . This ratio can be expressed as a ratio of subaperture diameter, d , to Fried parameter, r_o [24],

$$\frac{\sigma_c^2}{\sigma_p^2} = \frac{(f_l \sigma_\theta)^2}{(0.37 f_l \lambda / d)^2} = 2.37 \left(\frac{d}{r_o} \right)^{5/3}, \quad (3.25)$$

σ_c^2/σ_p^2	r_o (meters)
3	0.0799
2	0.1018
1	0.1544
1/2	0.2340
1/4	0.3547

Table 3.1 Fried parameter for various ratios of σ_c^2/σ_p^2 using Kolmogorov statistics with subaperture diameter $d = 9.2\text{cm}$.

where f_l is the subaperture focal length, and

$$\sigma_\theta^2 = 12.803/(k^2 r_o^{5/3} d^{1/3}), \quad (3.26)$$

is the measured mean square angular tilt for a square subaperture [28]. The factor 0.37 in the denominator of Eqn. (3.25) is a result of matching the e^{-1} points of a Gaussian spot distribution to the diffraction pattern of a square subaperture [18]. Table 3.1 lists the values for the Fried parameter, r_o , associated with the ratios identifying the curves in Fig. 3.4.

3.6.3 MAP estimator performance using von Karman statistics. Finally, the performance MAP estimator will be examined by comparing the ratio of the MSE of the MAP estimator to the MSE of the centroid estimator using von Karman statistics in the MAP estimator correlation matrix. Figure 3.5 is a plot of the error ratio as a function of average subaperture photon count, \bar{K} . The correlation matrix was computed using von Karman statistics for a 5×5 array of unobscured subapertures with outer scale $L_o = 50\text{m}$ and subaperture diameter $d = 9.2\text{cm}$. The various curves in each figure correspond to a particular value of the ratio of the mean square spot motion, σ_c^2 , to mean square spot size, σ_p^2 .

A relationship must now be found to relate the Fried parameter, r_o , to σ_c^2/σ_p^2 when von Karman atmospheric statistics are used. The first step is to write Eqn. (3.26) as a function of the slope correlation. The variable \hat{R}_{xx} will be used designate the normalized mean square slope and can be evaluated for Kolmogorov statistics using Eqn. (3.14) when the normalized offsets $(\tilde{x}_o, \tilde{y}_o)$

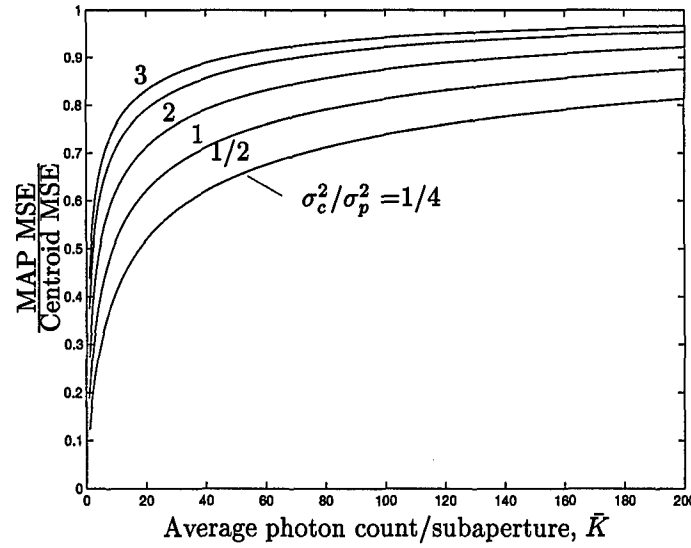


Figure 3.5 Relative MSE performance as a function of average photon count per subaperture. Von Karman statistics were used for a 5×5 array of unobscured subapertures with outer scale $L_o = 50\text{m}$ and $d = 9.2\text{cm}$.

σ_c^2 / σ_p^2	r_o (meters)
3	0.0702
2	0.0896
1	0.1358
1/2	0.2058
1/4	0.3120

Table 3.2 Fried parameter for various ratios of σ_c^2 / σ_p^2 using von Karman statistics with outer scale $L_o = 50\text{m}$ and subperture diameter $d = 9.2\text{cm}$.

are equal to zero, $r_o = 1$, and $d = 1$. Using the normalized mean square slope, Eqn. (3.26) can be written as,

$$\sigma_\theta^2 = \frac{2\hat{R}_{xx}}{k^2 r_o^{5/3} d^{1/3}}, \quad (3.27)$$

where $2\hat{R}_{xx} = 12.803$. The factor of 2 is required since the slope correlation defined by Eqn. (3.14) is valid for slopes in a single orthogonal direction and σ_θ is defined for a vector parameter in Eqn. (3.26).

A similar approach can be used to derive an equation for σ_θ^2 using von Karman statistics. The variable $\hat{R}_{xx}(d, L_o)$ will be used designate the normalized mean square slope for a specific d

and L_o using Eqn. (3.18) when the normalized offsets $(\tilde{x}_o, \tilde{y}_o)$ are equal to zero. The mean square angular tilt for a square subaperture in Eqn. (3.26) can be written:

$$\sigma_\theta^2 = \frac{2\check{R}_{xx}(d, L_o)}{k^2 r_o^{5/3}}. \quad (3.28)$$

The factor of 2 is required since the slope correlation defined by Eqn. (3.18) is valid for slopes in a single orthogonal direction. As the outer scale approaches infinity, the value of the normalized mean square slope for von Karman atmospheric statistics will approach the value of the normalized mean square slope for Kolmogorov statistics:

$$2\check{R}_{xx}(d = 1, L_o \rightarrow \infty) \rightarrow 12.803. \quad (3.29)$$

The ratio between mean square spot motion and mean square spot size in Eqn. (3.25) can now be written in terms of the normalized mean square slope using von Karman atmospheric statistics:

$$\frac{\sigma_c^2}{\sigma_p^2} = \frac{2\check{R}_{xx}(d, L_o)d^2}{r_o^{5/3}(0.37(2\pi))^2}. \quad (3.30)$$

For a given ratio of σ_c^2/σ_p^2 , the Fried parameter, r_o , can be determined. Table 3.2 lists the values of the Fried parameter, r_o , associated with the ratios identifying the curves in Fig. 3.5.

IV. Verification of simulation performance and test plan

4.1 Introduction

This chapter verifies the accuracy of the wavefront sensor simulation and maximum *a posteriori* (MAP) slope estimator implementation as well as outlining a test plan for the MAP estimator. First, the wavefront sensor simulation performance was examined. The accuracy of the wavefront sensor simulation was verified by comparing the shot limited performance to the theoretical bound. Since the wavefront sensor simulation employs a centroid estimator to determine shift estimates, the performance of the centroid estimator was compared to the shot noise limited performance. Next, the effects of read noise and atmospheric turbulence were examined. The second part of this chapter verified the performance of the MAP estimator implementation. The MAP estimator mean square error (MSE) performance was evaluated as the ratio of MAP estimator MSE to centroid estimator MSE. The curves generated from the simulations were compared to the theoretical performance curves. The final part of this chapter outlines a test plan to fully evaluate the MAP estimator performance using a variety of wavefront sensor and atmospheric parameters.

4.2 Hartmann wavefront sensor simulation verification

In order to verify the performance of the wavefront sensor simulation, the shot noise limited performance of the wavefront sensor was examined. The shot noise limited performance was evaluated using a point source irradiance while ignoring the effects of read noise on the detection process and removing any effects of atmospheric turbulence from the incident wavefront phase. Using these assumptions, each subaperture in the wavefront sensor array forms an intensity distribution centered on the optical axis. While the intensity distributions are centered on the optical axis of each subaperture, shot noise in the detection process results in an apparent shift off the optical axis. The shift off the optical axis is the error directly resulting from the presence of shot noise in the detection process. This error is the shot limited performance of the wavefront sensor simulation.

The shot noise limited performance of the simulation was compared to the theoretical bounds in order to verify the simulation accuracy. Since the shot noise limited performance of a 2×2 CCD detector array (or quad cell detector) has been agreed upon by several sources [17,27,31], a quad cell detector was used to verify the simulation performance. The theoretical shot noise limited root mean square error (RMSE) performance for a subaperture using a quad cell detector in the absence of atmospheric turbulence was derived by Welsh [31] to be

$$\text{RMSE}(\vec{x}) = \frac{\sqrt{2\pi}}{\sqrt{\bar{K}}} \frac{\lambda f_l}{2\pi d_w} \quad (\text{meters}), \quad (4.1)$$

where \bar{K} is the average photon count per subaperture, f_l is the subaperture focal length, λ is the average wavelength, and d_w is the wavefront sensor subaperture diameter. The RMSE calculation in Eqn. (4.1) is the Cramer-Rao lower bound (CRLB) for any unbiased shift estimator [32]. In order to compare the shot noise limited performance of the simulation to the theoretical limit, a centroid shift estimation technique developed by Tyler [27] was used in place of the first moment calculation defined by Eqn. (2.12). Tyler's method optimizes the centroid shift estimation for a quad cell detector by scaling the ratio of the difference in intensity falling on either half of the detector (ΔI_x and ΔI_y) to the total intensity falling of the detector (I_o) by a constant in order to obtain the centroid shifts in the \hat{x} and \hat{y} directions. The centroid shift, \vec{x} , can be determined for a square aperture and a point source irradiance using the relationship developed in Appendix C:

$$\vec{x} = -\frac{\Delta I_x}{I_o} \frac{f_l \lambda}{d_w} \hat{x} - \frac{\Delta I_y}{I_o} \frac{f_l \lambda}{d_w} \hat{y} \quad (\text{meters}), \quad (4.2)$$

where f_l is the subaperture focal length, λ is the average wavelength, and d_w is the wavefront sensor subaperture diameter. It should be noted that this shift estimator was derived for a quad cell detector with shot noise and is not valid when read noise and atmospheric turbulence are included in the wavefront sensor simulation.

Equation (4.2) was used to calculate the centroid shift in the wavefront sensor simulation. The simulation RMSE performance was compared to the theoretical RMSE performance. Figure 4.1 shows the wavefront sensor simulation performance matched the shot noise limited performance. The results were obtained by averaging the RMSE for 500 simulation runs at each value of \bar{K} .

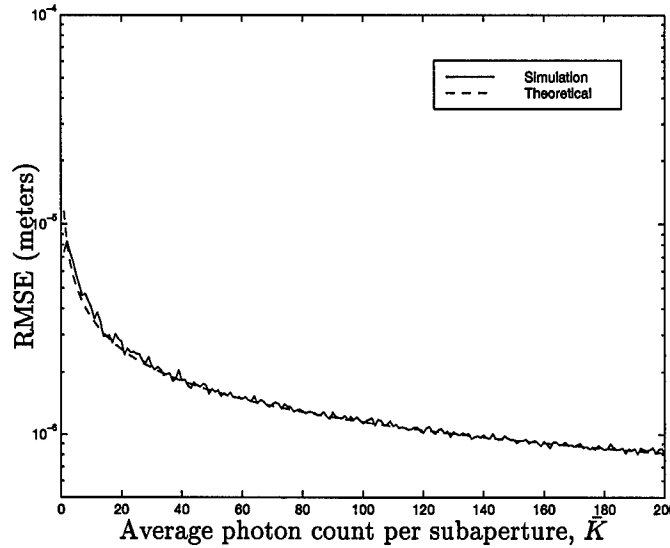


Figure 4.1 Actual vs Theoretical RMSE for a wavefront sensor using a quad cell detector. The wavefront sensor simulation used a modified shift estimator and was run in the absence of read noise or atmospheric turbulence.

4.3 Centroid estimator RMSE performance

4.3.1 Shot noise effects. The performance of the centroid estimator was examined next. As seen in Fig. 4.1, the RMSE performance of the wavefront sensor with quad cell detector approached the Cramer-Rao bound when a modified shift estimator was used to find the centroid shift. The wavefront sensor simulation employed a centroid estimator that uses a moment calculation described by Eqn. (2.12) to find the centroid shifts. Since the centroid estimator was not optimized for shot noise limited performance, as was the estimator derived in Appendix C, the use of a centroid estimator should result in shift estimates with more error. At best, the centroid estimator performance should match shot noise limited performance as the number of pixels in the

detector array gets very large. Figure 4.2 shows the performance of the centroid estimator as well as the shot noise limited performance developed in the previous section.

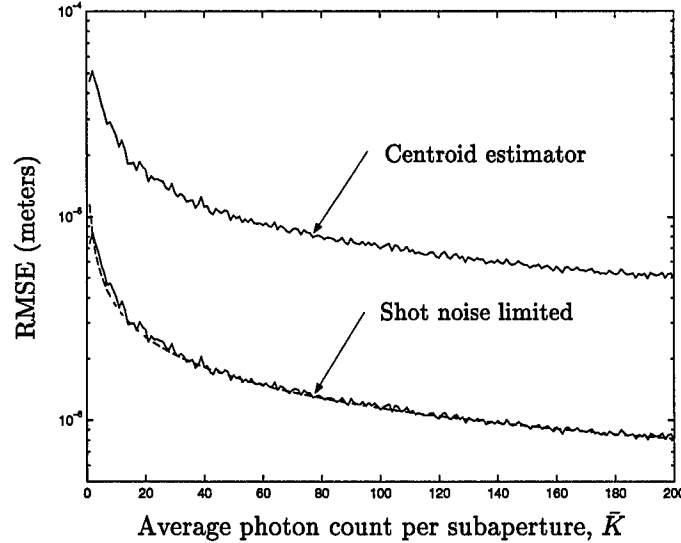


Figure 4.2 Comparison of the centroid estimator and the Cramer-Rao RMSE performance for a wavefront sensor using a quad cell detector. The wavefront sensor was a 5×5 unobscured array of detectors without read noise or atmospheric turbulence.

4.3.2 Read noise effects. Since read noise is present in the detection process, the effects it has on both the theoretical bounds and centroid estimator performance were examined. The addition of read noise in the detection process should increase the shift estimate error. First, the effects on the theoretical bounds will be examined. If the total error in the detection process is assumed to result from shot and read noise, the MSE can be written as a sum of the MSE due to shot noise and the MSE due to read noise [17]:

$$\sigma_n^2 = \sigma_{sn}^2 + \sigma_{rn}^2 \quad (4.3)$$

Parenti developed a pair of equations to describe the error resulting from shot and read noise when the wavefront sensor used a quad cell detector in each subaperture [17]. The MSE resulting from

shot noise is,

$$\sigma_{sn}^2 = \frac{2\pi^2 \left(1 + \left(\frac{d_w}{r_o}\right)^2\right)}{\bar{K}} \left(\frac{\lambda f_l}{2\pi d_w}\right)^2 \quad (\text{meters}^2), \quad (4.4)$$

and the MSE resulting from read noise is,

$$\sigma_{rn}^2 = \frac{8\pi^2 \left(1 + \left(\frac{d_w}{r_o}\right)^2\right) \sigma_R^2}{\bar{K}^2} \left(\frac{\lambda f_l}{2\pi d_w}\right)^2 \quad (\text{meters}^2), \quad (4.5)$$

where \bar{K} is the average photon count, σ_R^2 is the variance of the read noise for a single detector pixel, f_l is the subaperture focal length, d_w is the wavefront sensor subaperture diameter, λ is the average wavelength, and r_o is the Fried parameter. If no turbulence is assumed ($r_o \rightarrow \infty$), the expression for the MSE in Eqn. (4.4) is consistent with Eqn. (4.1).

Using Eqns. (4.4) and (4.5), the theoretical performance of a wavefront sensor using a quad cell detector in each subaperture was examined under two conditions. First, the performance was examined as read noise increased in the absence of atmospheric turbulence ($r_o \rightarrow \infty$). Then, the performance was examined as the level of atmospheric turbulence increased in the absence of read noise ($\sigma_R = 0$).

The curves in Fig. 4.3 show the effects of increasing read noise variance on theoretical RMSE performance. At low photon counts, the read noise significantly increases the shift error. As the photon count increases, the MSE due to read noise decreases by a factor of \bar{K}^2 , and the overall MSE performance converges to the shot noise limited performance of the centroid estimator. Similar results were obtained with the wavefront sensor simulation. The performance of the centroid estimator for increasing levels of read noise variance is shown in Fig. 4.4. At low photon counts, the read noise significantly effects the performance of the centroid estimator and as the photon count increases, the error curves converge to the shot noise limited performance curve of the centroid estimator ($\sigma_R^2 = 0$).

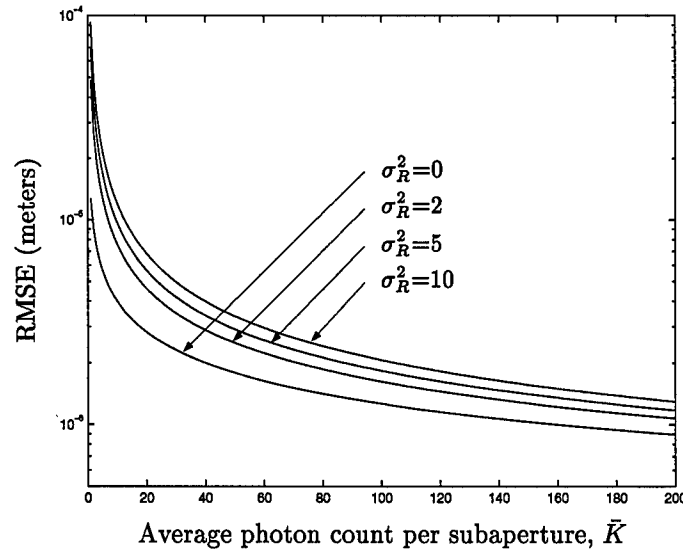


Figure 4.3 Theoretical RMSE performance as read noise variance (σ_R^2) increases for a quad cell detector. The wavefront sensor was a 5×5 unobscured array of subapertures without atmospheric turbulence.

4.3.3 Atmospheric turbulence effects. The theoretical and centroid estimator RMSE performance in the presence of atmospheric turbulence were examined next. Atmospheric turbulence deforms the overall shape of the intensity distribution that forms on the detector array. In addition to the shot noise, the deformation contributes to the shift error during the detection process. The curves in Fig. 4.5 show the effects of increasing atmospheric turbulence on theoretical RMSE performance. The individual curves correspond to a particular ratio of σ_c^2/σ_p^2 . The theoretical RMSE curves were calculated using Eqn. (4.4) using values of r_o found in Table 3.2. The theoretical RMSE increased as the atmospheric turbulence increased. Similar results were obtained with the wavefront sensor simulation. The curves in Fig. 4.6 show the centroid estimator RMSE performance as atmospheric turbulence increases.

4.4 MAP estimator performance

4.4.1 Introduction. In order to verify the MAP estimator performance, the combination of the phase screen generation program, the wavefront sensor, and the MAP estimator implementation was used to generate a set of baseline performance curves. The baseline performance curves were

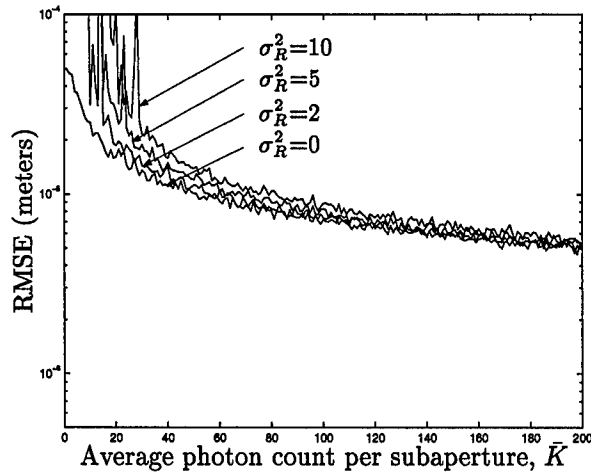


Figure 4.4 RMSE performance for a centroid estimator using a quad cell detector with read noise. The curves correspond to a particular read noise variance (σ_R^2). As σ_R^2 increases, the RMSE increases. The wavefront sensor was a 5×5 unobscured array of subapertures without atmospheric turbulence.

obtained using a set of parameters that matched the theoretical assumptions used in the derivation of the MAP estimator. The curves generated in simulation should match the theoretical curves shown in Fig 3.5.

4.4.2 Simulation flowchart. Figure 4.9 is a flow chart for the shell program that implements the MAP estimator in simulation. After choosing a desired ratio of σ_c^2/σ_p^2 , r_o was determined using Eqn. (3.30). Then, a series of phase screens were generated, and the correlation matrix was calculated for the MAP estimator implementation. For each phase screen, a centroid shift estimate vector (\hat{x}_{est}) and an actual centroid shift vector (x_{act}) was determined using the wavefront sensor simulation. The centroid shift estimate vector was then used to calculate the MAP shift estimate vector (\hat{x}_{MAP}). The average MSE for the centroid and MAP estimates were then calculated using (x_{act}) as the correct shift vector. This process was repeated for values of \bar{K} ranging from 1 to 200 photons per subaperture.

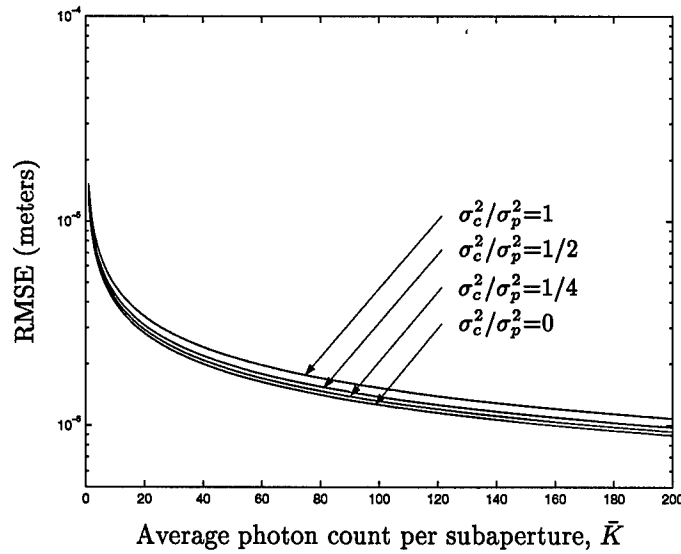


Figure 4.5 RMSE performance for a quad cell detector array with no read noise. The curves correspond to a particular value of σ_c^2/σ_p^2 . The wavefront sensor was a 5×5 unobscured array of subapertures.

4.4.3 Simulation performance. In theory, the ratio of the MAP estimator MSE to the centroid estimator MSE should match the theoretical curves shown in Fig. 3.5. The parameters used to generate the baseline performance curves are listed in Table 4.1. The physical wavefront sensor parameters were chosen to match the Generation III Hartmann wavefront sensor parameters used at the Starfire Optical Range [19]. However, instead of using a 16×16 array of subapertures, the simulation used a 5×5 array in order to keep the array sizes manageable. (Larger array sizes would have exceeded the resident memory capabilities of the computational platforms used, greatly increasing processing time for each simulation.) In addition to the decreased sensor array size, certain parameters were changed to approximate the theoretical assumptions made by Sallberg [23]: Infinite resolution of the subaperture detector array was approximated using a 20×20 detector array, the read noise was eliminated, and overlap between subapertures was not allowed.

The baseline performance curves of the ratio of the MAP estimator MSE to the the centroid estimator MSE as a function of average photon count per subaperture, \bar{K} are shown in Fig. 4.7. The dashed curves correspond to the theoretical performance shown in Fig. 3.5 while the solid curves

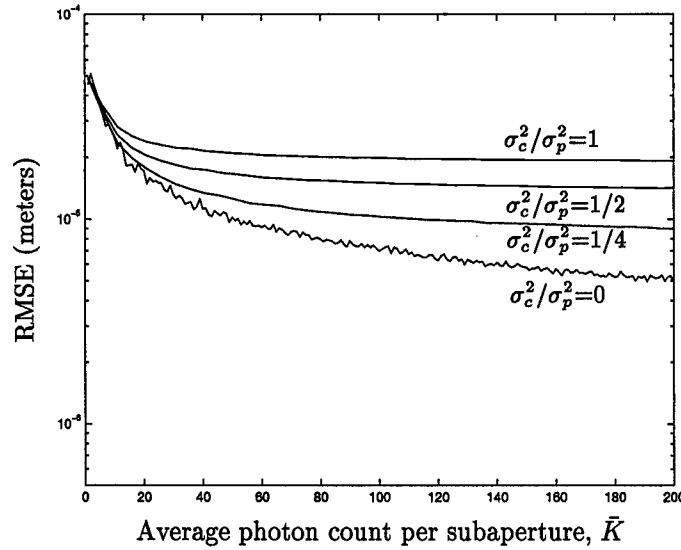


Figure 4.6 RMSE performance for a centroid estimator using a quad cell detector array with no read noise. The curves correspond to a particular value of σ_c^2/σ_p^2 . The wavefront sensor was a 5×5 unobscured array of subapertures.

correspond to the simulation performance. Von Karman statistics were used for a 5×5 array of subapertures with $L_o = 50\text{m}$ and $d = 9.2\text{cm}$. The pairs of curves correspond to a particular ratio of σ_c^2/σ_p^2 .

The MAP estimator MSE performance was upper bounded by the centroid estimator MSE as predicted by Sallberg [23]. While the baseline performance curves generated by the simulation should match the theoretical curves, the expected relative MAP estimator MSE performance was not quite achieved. In fact, the relative MAP estimator MSE performance in simulation appeared to perform better than the theoretical expectations. There were several reasons why the curves generated from simulation did not fall directly on top of the theoretical curves.

The first reason the theoretical and simulation curves do not exactly match was that the actual value of mean square motion, σ_c^2 , to the mean square spot size, σ_p^2 , calculated from the phase screens did not match the theoretical ratio. The value for the Fried parameter, r_o , was determined from the ratio of σ_c^2/σ_p^2 using Eqn. (3.30). The same r_o was used both in the phase screen generation and in the calculation of the correlation matrix for the MAP estimator. Using

Phase screen generator	Subaperture diameter (d)	9.2cm
	Outer scale (L_o)	50m
	Fried Parameter (r_o)	determined by σ_c^2/σ_p^2
Wavefront sensor	Subaperture array size	5×5
	Subaperture width (d_w)	200E-6m
	Subaperture focal length (f_t)	650E-5m
	Average wavelength (λ)	550nm
	Subaperture detector array	20×20
	CCD duty cycle	100 percent
	Read noise (σ_R^2)	Variance = 0
	Wavefront tilt	Included
MAP estimator	Subaperture overlap	Not allowed
	Atmospheric statistics	von Karman
	Outer scale (L_o)	50m
	Fried parameter (r_o)	determined by σ_c^2/σ_p^2

Table 4.1 Parameters used to verify the simulations match the theoretical performance limits.

the phase screens generated from the value of r_o , the actual mean square spot motion and mean square spot size were measured and the actual ratio of σ_c^2/σ_p^2 was calculated. The theoretical ratios did not always match the calculated ratio.

The second reason the theoretical and simulation curves do not exactly match was that the MAP estimator was not necessarily a minimum mean square error (MMSE) estimator. A MAP estimator that uses parameters with jointly Gaussian distributions will result in a MMSE estimator [15]. However, the development of the MAP estimator did not use jointly Gaussian distributions. Shot noise was modeled with a Poisson process and the irradiance distribution was only approximated by a Gaussian distribution. Since the development of the MAP estimator did not use jointly Gaussian distributions, the theoretical performance defined by Eqn. (3.24) was not necessarily the MMSE performance for the MAP estimator. As a result, the actual MSE for the MAP estimator in simulation may fall above or below the theoretical MSE performance curve.

Finally, there were errors associated with the discrete nature of the simulations. The sampling of the phase screen was done at the minimum Nyquist rate [30]. The wavefront sensor used a discrete Fourier Transform to find the intensity distributions for each subaperture. The calculation of the

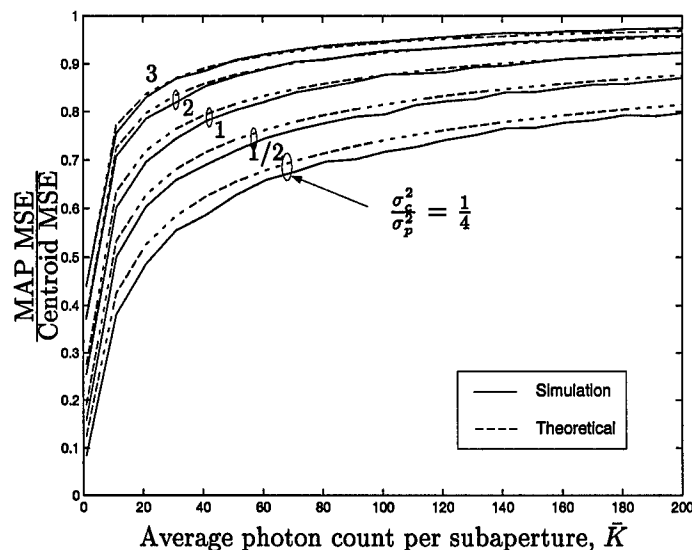


Figure 4.7 Ratio of MSE's for the MAP and the centroid estimator as a function of average photon count per subaperture, \bar{K} . Von Karman statistics were used for a 5×5 array of subapertures with $L_o = 50\text{m}$ and $d = 9.2\text{cm}$. The curves correspond to a particular ratio of σ_c^2 / σ_p^2 .

correlation values for von Karman atmospheric statistics included a finite series approximation of a modified Bessel function of the second kind as well as numerical integration. While steps were taken to minimize the errors associated with each of these simulations, it must be recognized that errors exist and propagate through the simulations.

4.5 Test plan

Two formats were used to present the simulation results. Absolute error plots will show the MAP and centroid estimator MSE as a function of average photon count per subaperture, \bar{K} . Relative error plots will show the ratio of the MAP estimator MSE to the centroid estimator MSE as a function of \bar{K} . An improvement in the relative MAP estimator MSE performance does not indicate an absolute improvement in the MAP estimator MSE performance. It simply means the the MAP estimator MSE performance relative to the centroid estimator MSE performance has improved. It is possible for the relative MAP estimator MSE performance to improve while the absolute MAP estimator MSE performance actually gets worse.

The goal of the remaining simulations was to examine the effects of changing the wavefront sensor parameters listed in Table 4.1 on the MSE performance. The eventual goal was to test the MSE performance using actual wavefront sensor and atmospheric parameters. The following list shows the order in which the wavefront sensor and atmospheric parameters will be examined in simulation.

- Remove global tilt on the incident wavefront. This was done to simulate the presence of a tip-tilt mirror in the adaptive optics system.
- Allow overlap. The effects of allowing light to spill over onto adjacent subapertures were examined. In actual wavefront sensors, there is no way to prevent spill over from occurring on the detector array short of turning off the pixels bordering adjacent subapertures.
- Decrease the size of the detector array. The MAP estimator development assumed the subaperture detector array had infinite resolution. The infinite array was approximated using a 20×20 pixel array in each subaperture. However, typical wavefront sensors utilize quad cell detectors or 4×4 detector arrays [9,19]. The simulations will investigate the performance for 8×8 , 4×4 , and 2×2 detector arrays in each subaperture.
- Add read noise. Read noise is a source of error for all CCD detection devices. Using the 4×4 and 2×2 detector arrays, the effects of read noise was examined for variances of 2, 5, and $10 \text{ (photons/pixel)}^2$.
- Incorrect atmospheric parameters in the MAP estimator. Up until this point in time, it was assumed that the atmospheric parameters were known with a high degree of certainty. While the wavefront sensor can be used to estimate atmospheric parameters [3,6,25], error within the wavefront sensor limits the degree of certainty to which the data can be trusted. Therefore, the MAP estimator was implemented using incorrect atmospheric parameters.
- Modified detector array. A modified 4×4 detector array was tested. The detector was designed such that the four center pixels were active and the pixels around the border of the

array were turned off. The goal with this design was to minimize electronic crosstalk between pixels in adjacent subapertures. This configuration was used in the SOR Generation III tests [19].

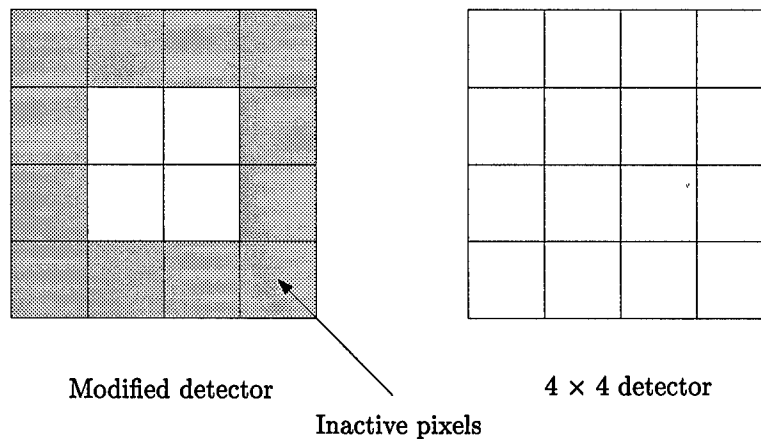


Figure 4.8 The figure on the right is the standard 4×4 detector array while the figure on the left is the modified SOR Generation III detector.

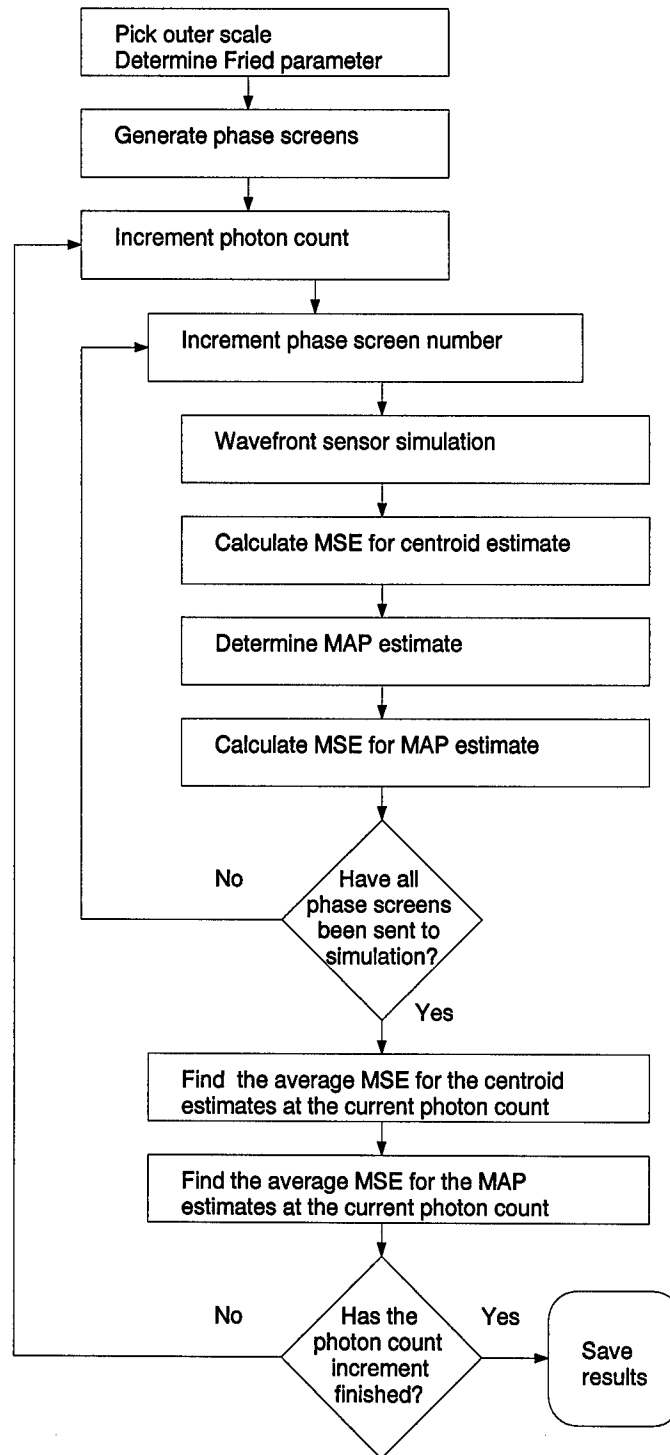


Figure 4.9 A flow chart for the combined operation of the phase screen generation program, the wavefront sensor simulation, and the MAP estimator implementation.

V. Results and Analysis

5.1 Introduction

To this point, the performance of the MAP slope estimator has been validated using wavefront sensor parameters that approximated the assumptions made in the derivation of the MAP estimator: The detection array was assumed large, read noise was not included in the detection of intensity distributions, overlap between subapertures was prohibited, and the atmospheric parameters were known with a high degree of certainty. This chapter examined the MAP and centroid estimator MSE performance as the idealized wavefront sensor parameters were changed to reflect parameters that could be found in realizable wavefront sensors. First, the global tilt was removed from the incident wavefront to simulate the presence of a tip-tilt mirror in the adaptive optics system. Next, the intensity distributions were allowed to overlap into adjacent subapertures. The number of pixels in each subaperture detector array was decreased. Finally, read noise was added to the detection process. In addition to changing the wavefront sensor parameters, the atmospheric parameters were changed as well. Up to this point, it was assumed that the atmospheric parameters were known with a high degree of certainty. Since this is rarely true, the effects of using incorrect Fried parameters and outer scales in the MAP estimator implementation were examined. The last series of simulations examined the performance of the MAP estimator when a modified subaperture detector array was used.

5.2 Global tilt

Since adaptive optics systems typically employ a tip-tilt mirror [13], the effect of removing the global tilt from the incident wavefront was examined. The theoretical results presented by Sallberg [24] showed that the relative MAP estimator MSE performance decreased when the global tilt was removed from the incident wavefront. The decreased relative MAP estimator MSE performance resulted from a loss of slope correlation between subapertures due to the tilt removal.

Similar results should occur in simulation. Removing the global tilt from the incident wavefronts should result in a decrease in the relative MAP estimator MSE performance.

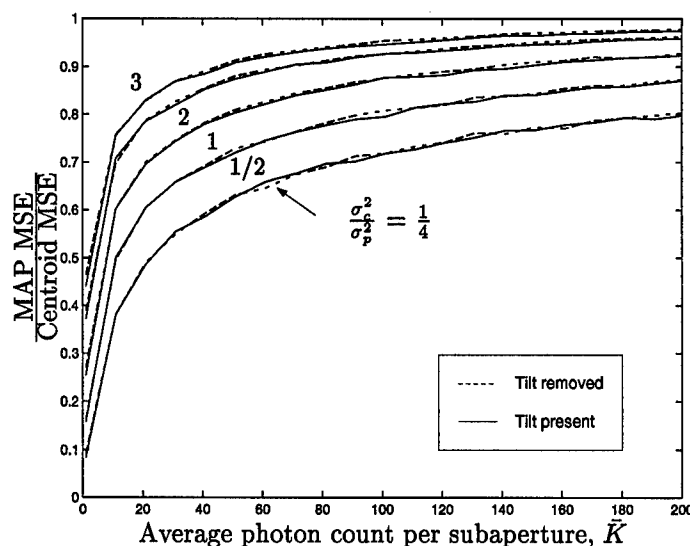


Figure 5.1 Relative MSE performance as a function of average photon count per subaperture, \bar{K} , for tilt removed wavefronts. The curves correspond to a particular ratio of σ_c^2 / σ_p^2 . Von Karman statistics were used for a 5×5 array of subapertures with $L_o = 50\text{m}$ and $d = 9.2\text{cm}$.

Figure 5.1 shows the relative MSE performance when the parameters listed in Table 4.1 were used with global tilt removed from the incident wavefronts. There was no significant decrease in relative MAP estimator MSE performance when the global tilt was removed from the incident wavefronts. The results presented by Sallberg [24] used Kolmogorov atmospheric statistics. Since von Karman atmospheric statistics were used in the simulations, there was less slope correlation between subapertures. The decrease in slope correlation resulting from the removal of global tilt from the incident wavefronts had minimal effect on the relative MAP estimator MSE performance.

5.3 Intensity overlap

The effect of allowing the intensity distributions to spill over onto adjacent subaperture detector arrays was examined next. While the ratio of mean square spot motion to mean square spot size has been used to identify specific performance curves, the actual wavefront sensor parameters

will determine the actual mean square spot size and mean square spot motion. If a wavefront sensor is correctly designed to operate below a known maximum level of turbulence, the mean square spot motion within a particular subaperture will be small enough to prevent the intensity distribution from overlapping onto adjacent subaperture detector arrays. Since the wavefront sensor parameters used for these simulations were optimized for the selected turbulence levels, there should be no significant decrease in relative MAP estimator MSE performance due to overlap.

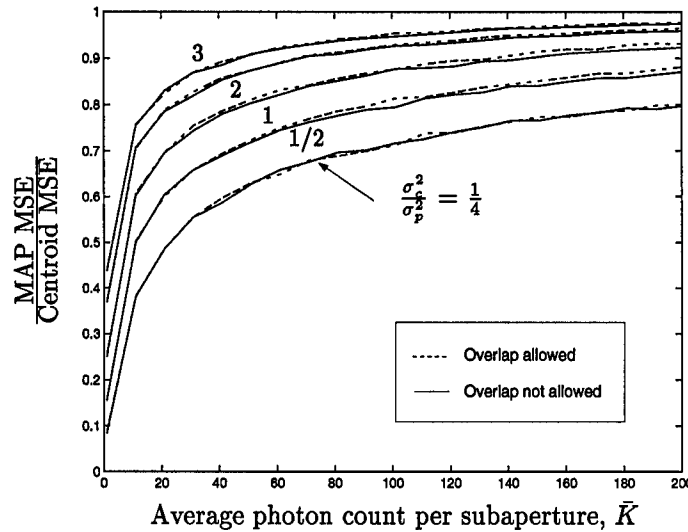


Figure 5.2 Relative MSE performance as a function of average photon count per subaperture count, \bar{K} , for overlap allowed. The curves correspond to a particular value of the ratio of σ_c^2/σ_p^2 . Von Karman statistics were used for a 5×5 array of subapertures with $L_o = 50\text{m}$ and $d = 9.2\text{cm}$.

Figure 5.2 shows the relative MAP estimator MSE performance when the parameters listed in Table 4.1 were used while allowing intensity distributions to overlap onto adjacent subapertures. There was only a slight decrease in relative MAP estimator MSE performance. The SOR Generation III parameters resulted in a spot that was about 1/6 the width of the subaperture diameter. The largest value of σ_c^2/σ_p^2 used in the simulations constrained the mean square spot motion to the center 25 percent of the detector array 99 percent of the time. As a result of the limited mean square spot motion on the detector array, overlap had little effect of the relative MAP estimator MSE performance. While the relative MAP estimator MSE performance showed minimal change,

there was a slight increase in the absolute MSE performance of the MAP estimator when overlap was allowed. Figure 5.3 shows the increase in MAP estimator MSE performance when overlap was allowed for $\sigma_c^2/\sigma_p^2 = 1$.

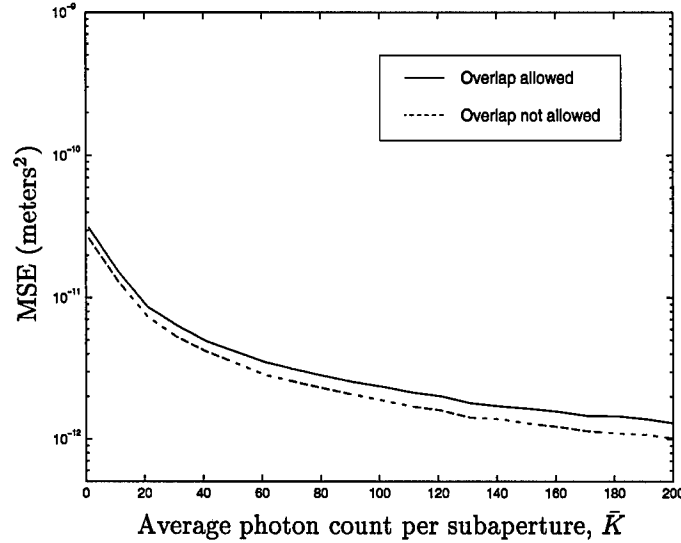


Figure 5.3 MAP estimator MSE performance as a function of average photon count per subaperture count, \bar{K} , for $\sigma_c^2/\sigma_p^2 = 1$. Von Karman statistics were used for a 5×5 array of unobscured subapertures with $L_o = 50\text{m}$ and $d = 9.2\text{cm}$.

In order to observe a decrease in the relative MAP estimator MSE performance, the wavefront sensor parameters were changed to be non-optimal for the selected turbulence levels by increasing the subaperture focal length by a factor of five. This will cause the irradiance distribution to overlap onto adjacent subapertures as it roams about the detector array. For the same ratio of $\sigma_c^2/\sigma_p^2 = 1$ used in the previous simulation, both the mean square spot size and the mean square spot motion were larger due to the increased subaperture focal length. The effect of overlap on the relative MAP estimator MSE performance became obvious. Figure 5.4 shows that when the focal length was increased to reduce the optimality of the wavefront sensor design, the intensity overlap into adjacent subapertures significantly decreased the relative MAP estimator MSE performance as expected.

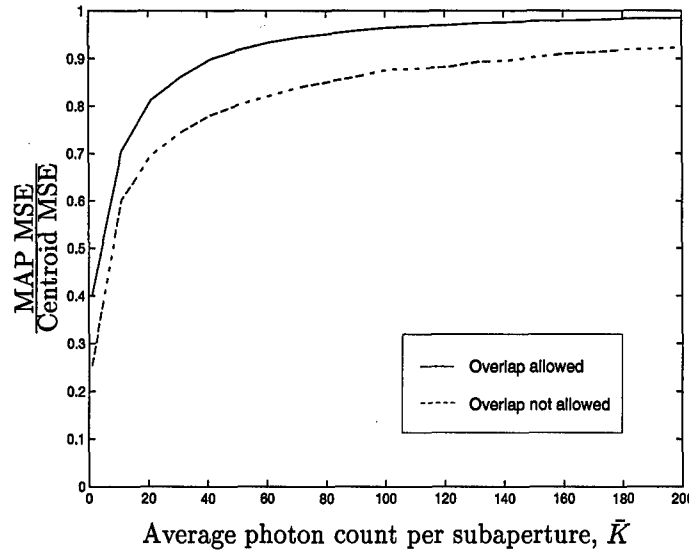


Figure 5.4 Relative MSE performance as a function of average photon count per subaperture count, \bar{K} . The subaperture focal length has been increased to $150 \times$ subaperture diameter. Von Karman statistics were used for a 5×5 array of unobscured subapertures with $\sigma_c^2/\sigma_p^2 = 1$, $L_o = 50\text{m}$ and $d = 9.2\text{cm}$.

5.4 Detector array size

For the derivation of the MAP estimator, the detection array in each subaperture was assumed to have an infinite resolution. Wavefront sensors typically use a small number of CCD detector pixels in each subaperture. The number of CCD pixels per subaperture is limited by many physical and wavefront sensor design related factors including the physical size of each CCD pixel, how closely the CCD pixels can be packed together, and the read noise variance for each pixel. Wavefront sensors typically use a quadcell or 4×4 subaperture detector array.

The centroid estimator MSE performance should increase as the number of pixels in each subaperture detector array decreases. As the error in the centroid shift estimates increases the MAP shift estimates will not be as accurate. The relative MAP estimator MSE performance should decrease as the number of pixels in each subaperture detection array decreases.

5.4.1 Relative MSE for a fixed ratio of σ_c^2/σ_p^2 . The next series of simulations examined the relative MAP estimator MSE performance using parameters listed in Table 4.1 with global

tilt removed, overlap allowed, and subaperture detection array sizes of 8×8 , 4×4 , and 2×2 . Figures 5.5 - 5.8 show the relative MAP estimator MSE performance as a function of average photon count per subaperture, \bar{K} , for a specific value of σ_c^2/σ_p^2 , with tilt removed wavefronts and overlap allowed. The individual curves in each figure correspond to the labeled subaperture detector array size. For all levels of atmospheric turbulence, the relative MAP estimator MSE performance decreased as the detector array size decreased. The grouping of the 20×20 and 8×8 curves and the 4×4 and 2×2 curves resulted from increased centroid shift estimate error. The denser 20×20 and 8×8 detector arrays allowed for a significantly lower centroid shift estimate error than the 4×4 and 2×2 detector arrays. The increased shift error decreased the relative MSE performance for the MAP estimator.

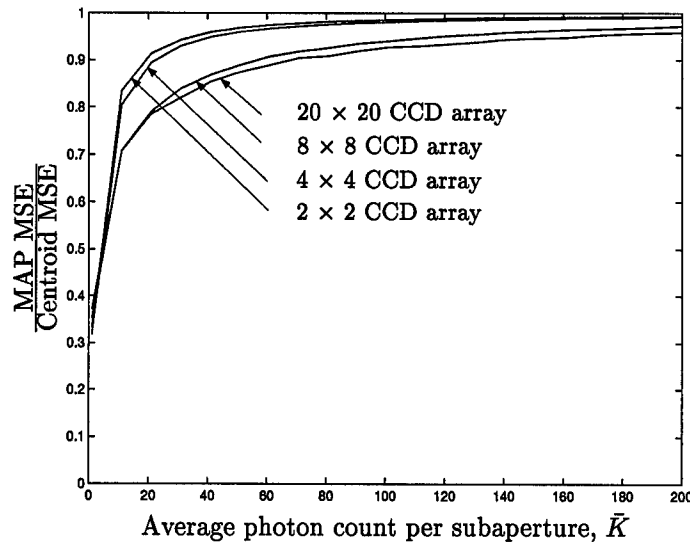


Figure 5.5 Relative MSE performance as a function of average photon count per subaperture, \bar{K} , for $\sigma_c^2/\sigma_p^2 = 2$. The curves correspond to a specific CCD detector array size. Von Karman statistics were used for a 5×5 array of unobscured subapertures with $L_o = 50\text{m}$, $d = 9.2\text{cm}$, tilt removed, and overlap allowed.

5.4.2 Absolute MSE for a fixed ratio of σ_c^2/σ_p^2 . The absolute MAP and centroid estimator MSE performance using the ratio of $\sigma_c^2/\sigma_p^2 = 1/2$ with tilt removed wavefronts and overlap allowed is shown in Fig. 5.9. As the number of pixels in the detector array decreased, both the MAP and centroid estimator MSE performance increased as expected. While the relative MAP estimator

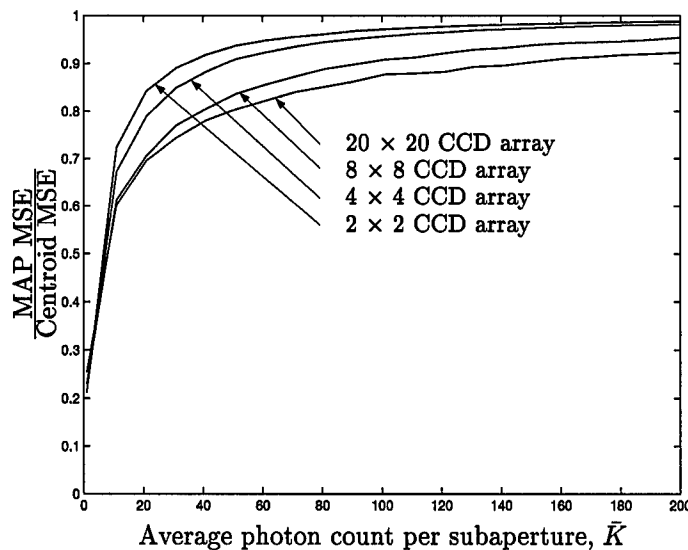


Figure 5.6 Relative MSE performance as a function of average photon count per subaperture, \bar{K} , for $\sigma_c^2/\sigma_p^2 = 1$. The curves correspond to a specific CCD detector array size. Von Karman statistics were used for a 5×5 array of unobscured subapertures with $L_o = 50\text{m}$, $d = 9.2\text{cm}$, tilt removed, and overlap allowed.

MSE performance in Fig. 5.7 indicated a slight decrease as the number of pixels in the detector array decreased for $\sigma_c^2/\sigma_p^2 = 1/2$, the absolute MAP and centroid estimator MSE performance increased by an order of 10^2 between the 2×2 and the 20×20 CCD array. This shows that the resolution of the detector array contributes significantly to the accuracy of both the MAP and centroid shift estimates.

5.4.3 Relative MSE for a fixed detector array size. The same MSE performance data was presented in another format. Figures 5.10 - 5.12 show the relative MAP estimator MSE performance as a function of average photon count per subaperture, \bar{K} , for a specific detector array size with tilt removed wavefronts and overlap allowed. The curves correspond to a specific value of σ_c^2/σ_p^2 . As expected, the relative MAP shift estimator MSE performance decreased as the level of atmospheric turbulence increased. For detector arrays with few pixels, there was only a slight decrease in relative MAP estimator MSE performance as the turbulence levels increased.

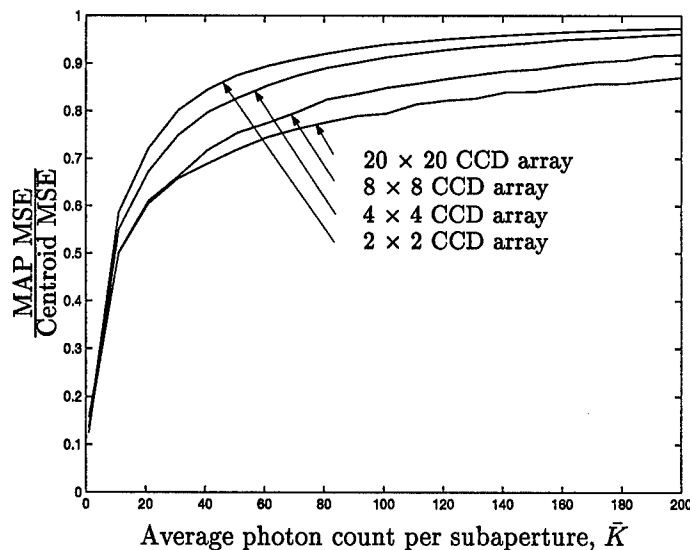


Figure 5.7 Relative MSE performance as a function of average photon count per subaperture, \bar{K} , for $\sigma_c^2/\sigma_p^2 = 1/2$. The curves correspond to a specific CCD detector array size. Von Karman statistics were used for a 5×5 array of unobscured subapertures with $L_o = 50\text{m}$, $d = 9.2\text{cm}$, tilt removed, and overlap allowed.

5.4.4 Absolute MSE for a fixed detector array size. The absolute MSE performance for the MAP and centroid estimators using a 4×4 detector array with tilt removed wavefronts and overlap allowed for various turbulence levels is shown in Fig. 5.13. As the level of atmospheric turbulence increased, the MAP and centroid estimator MSE performance increased as expected. While the relative MAP estimator MSE performance only showed a slight change for differing atmospheric turbulence levels in Fig. 5.11, the absolute MAP and centroid estimator MSE performance increased by an order of 10 as the ratio of σ_c^2/σ_p^2 increased from $1/4$ to 2 .

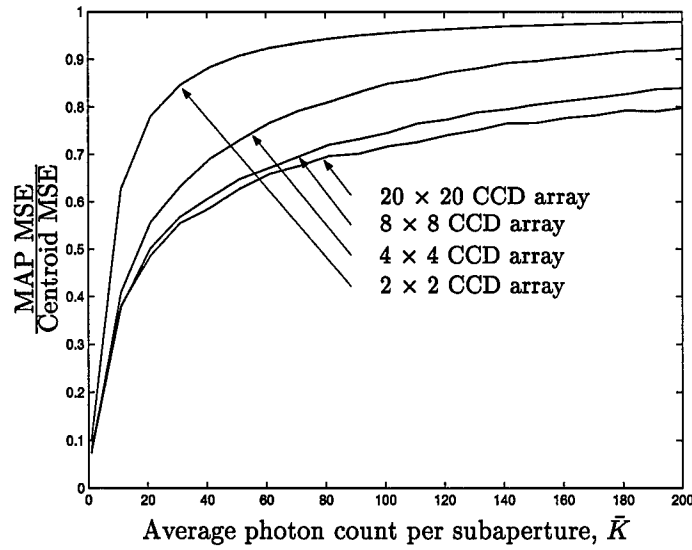


Figure 5.8 Relative MSE performance as a function of average photon count per subaperture, \bar{K} , for $\sigma_c^2/\sigma_p^2 = 1/4$. The curves correspond to a specific CCD detector array size. Von Karman statistics were used for a 5×5 array of unobscured subapertures with $L_o = 50\text{m}$, $d = 9.2\text{cm}$, tilt removed, and overlap allowed.

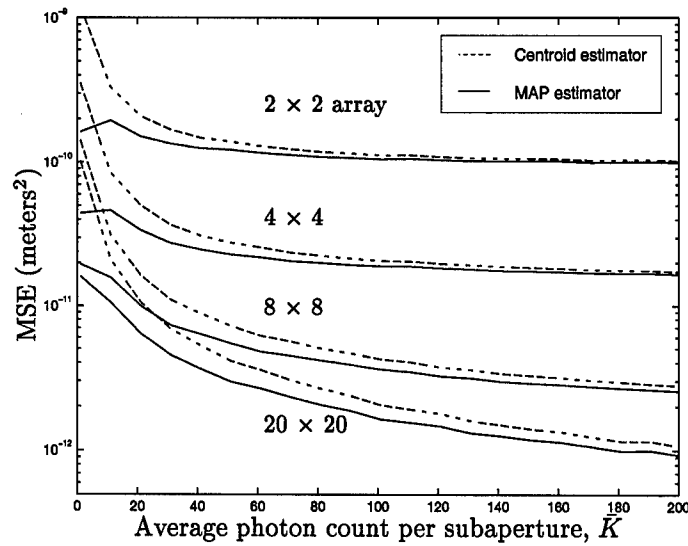


Figure 5.9 MAP and centroid estimator MSE performance as a function of average photon count per subaperture, \bar{K} , for $\sigma_c^2/\sigma_p^2 = 1/2$. Von Karman statistics were used for a 5×5 array of unobscured subapertures with $L_o = 50\text{m}$, $d = 9.2\text{cm}$, tilt removed, and overlap allowed.

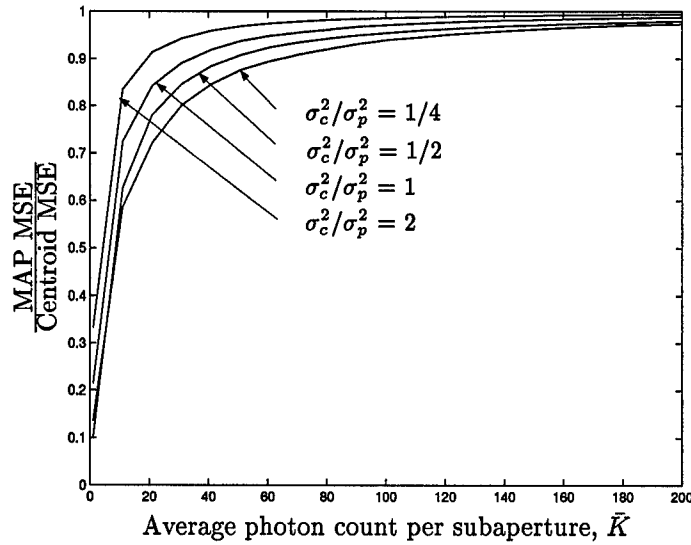


Figure 5.10 Relative MSE performance as a function of average photon count per subaperture, \bar{K} , for a 2×2 detector array. The curves correspond to a specific ratio of σ_c^2/σ_p^2 . Von Karman statistics were used for a 5×5 array of unobscured subapertures with $L_o = 50\text{m}$, $d = 9.2\text{cm}$, tilt removed, and overlap allowed.

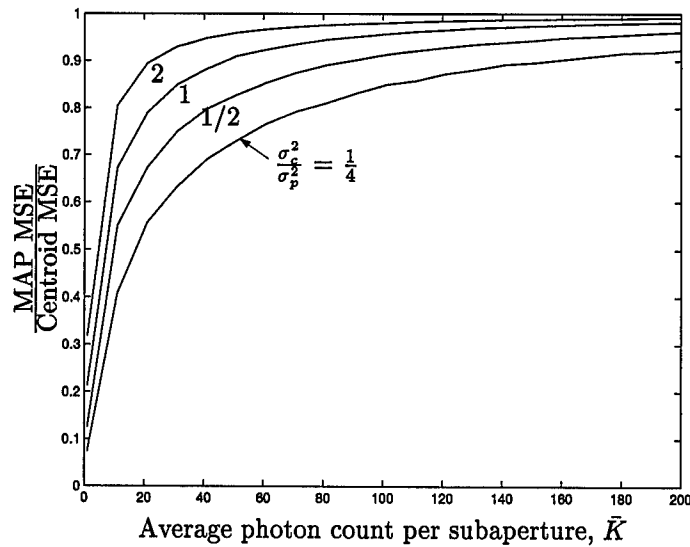


Figure 5.11 Relative MSE performance as a function of average photon count per subaperture, \bar{K} , for a 4×4 detector array. The curves correspond to a specific ratio of σ_c^2/σ_p^2 . Von Karman statistics were used for a 5×5 array of unobscured subapertures with $L_o = 50\text{m}$, $d = 9.2\text{cm}$, tilt removed, and overlap allowed.

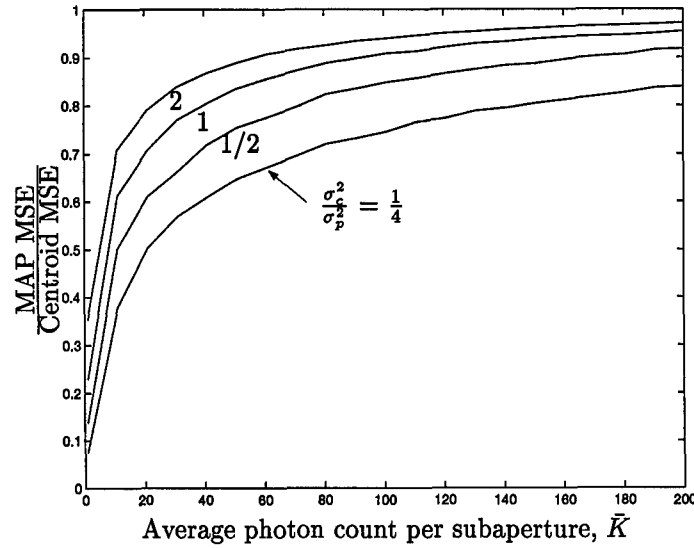


Figure 5.12 Relative MSE performance as a function of average photon count per subaperture, \bar{K} , for a 8×8 detector array. The curves correspond to a specific ratio of σ_c^2/σ_p^2 . Von Karman statistics were used for a 5×5 array of unobscured subapertures with $L_o = 50\text{m}$, $d = 9.2\text{cm}$, tilt removed, and overlap allowed.

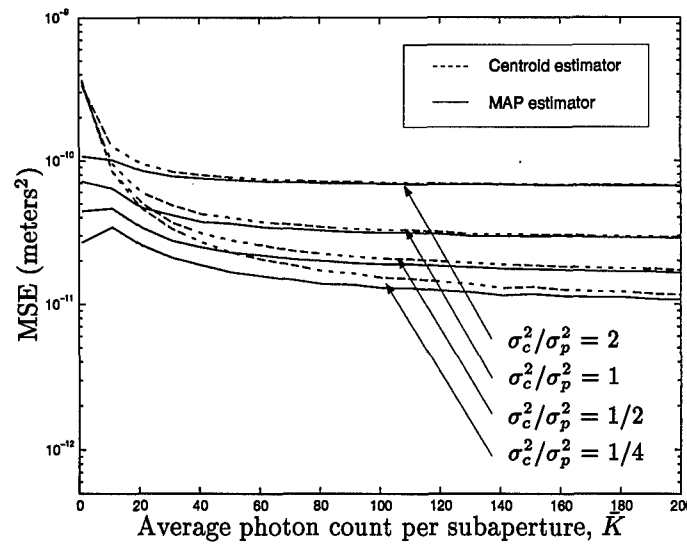


Figure 5.13 MAP and centroid estimator MSE performance as a function of average photon count per subaperture, \bar{K} , for a 4×4 detector array. The curves correspond to a specific ratio of σ_c^2/σ_p^2 . Von Karman statistics were used for a 5×5 array of unobscured subapertures with $L_o = 50\text{m}$, $d = 9.2\text{cm}$, tilt removed, and overlap allowed.

5.5 Read noise

The effect of read noise on the MSE performance was examined next. Read noise was modeled as an additive zero mean, Gaussian noise. Read noise corrupts the detector array pixel values resulting in an increase in the centroid shift MSE. The noisy centroid estimates should result in MAP shift estimates with higher MSE. The expected effect of adding read noise to the detection process should be a decreased in the relative MAP estimator MSE performance.

5.5.1 Relative MSE as detector read noise increases. The next series of simulations examined the relative MAP estimator MSE performance using parameters listed in Table 4.1 with read noise, global tilt removed, overlap allowed, and small subaperture detection arrays. The relative MAP estimator MSE performance was examined for detector sizes of 2×2 and 4×4 with read noise variances, σ_R^2 , of 2, 5, and 10 (photons/pixel)². Figures 5.14 - 5.21 show the results of read noise on the MSE performance with tilt removed and overlap allowed. Surprisingly, the relative MAP estimator MSE performance improved for both detector array sizes as the read noise variance increased. This implied that the MAP estimator was more robust than the centroid estimator in the presence of read noise.

As the read noise variance increased, there was more uncertainty in the MAP estimation at low average photon counts per subaperture. This was evident by the random fluxuations of the σ_R^2 curves in the relative MSE plots. As the average photon count per subaperture increased, the effects of the read noise were negated and the curves smoothed out and converged towards the $\sigma_R^2 = 0$ curve as expected.

5.5.2 Absolute MSE as detector read noise increases. Figures 5.16, 5.19, and 5.22 show the absolute MSE performance for the MAP and centroid estimator with tilt removed wavefronts and overlap allowed. These results were not surprising. For all cases, the MAP and centroid estimator MSE performance increased as the read noise variance increased. The MSE performance

for all values of read noise converged towards the $\sigma_R^2 = 0$ curve as \bar{K} gets large. This behavior was expected since the effects of read noise become insignificant as \bar{K} gets large. As the level of atmospheric turbulence decreased, the absolute MSE curves also decreased as expected.

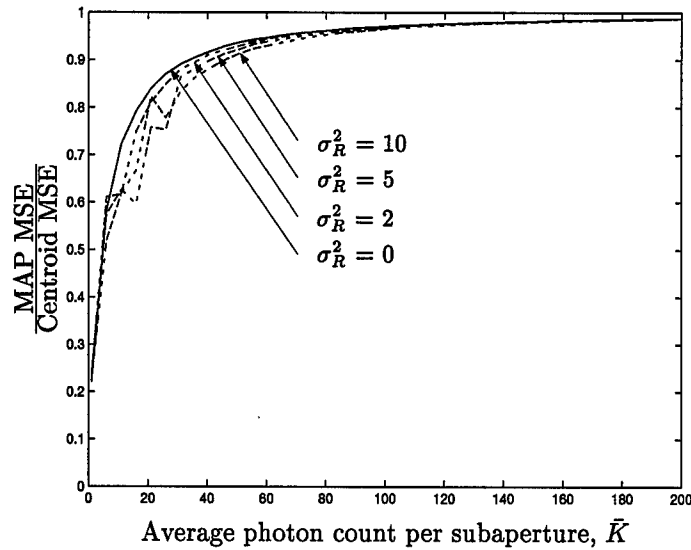


Figure 5.14 Relative MSE performance as a function of average photon count per subaperture, \bar{K} , for a 2×2 detector array with read noise. The individual curves correspond to a specific read noise variance, σ_R^2 . Von Karman statistics were used for a 5×5 array of unobscured subapertures with $L_o = 50\text{m}$, $d = 9.2\text{cm}$, $\sigma_c^2/\sigma_p^2 = 1$, tilt removed, and overlap allowed.

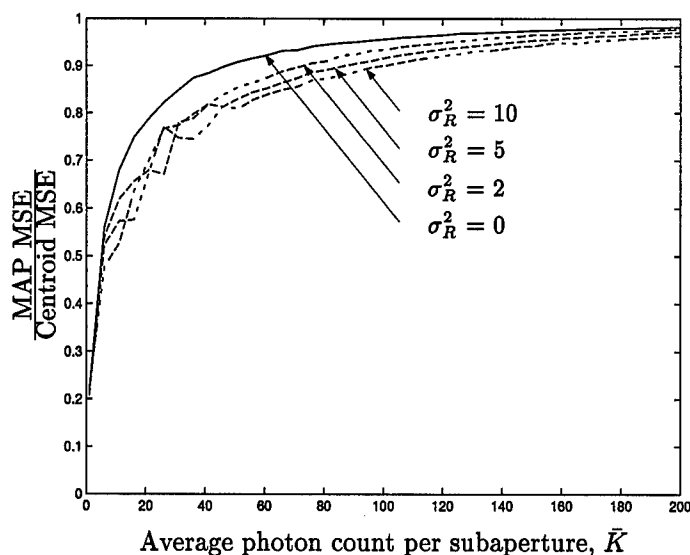


Figure 5.15 Relative MSE performance as a function of average photon count per subaperture, \bar{K} , for a 4×4 detector array with read noise. The individual curves correspond to a specific read noise variance, σ_R^2 . Von Karman statistics were used for a 5×5 array of unobscured subapertures with $L_o = 50\text{m}$, $d = 9.2\text{cm}$, $\sigma_c^2/\sigma_p^2 = 1$, tilt removed, and overlap allowed.

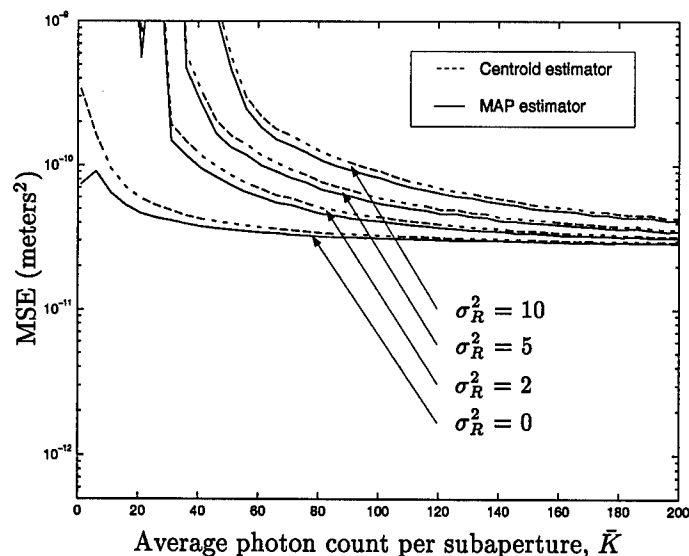


Figure 5.16 MAP and centroid estimator MSE performance as a function of average photon count per subaperture, \bar{K} , for a 4×4 detector array with read noise. The individual curves correspond to a specific read noise variance, σ_R^2 . Von Karman statistics were used for a 5×5 array of unobscured subapertures with $L_o = 50\text{m}$, $d = 9.2\text{cm}$, $\sigma_c^2/\sigma_p^2 = 1$, tilt removed, and overlap allowed.

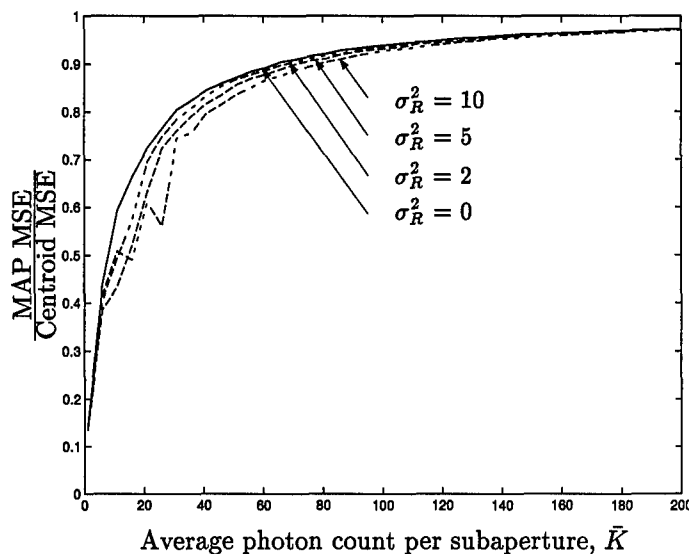


Figure 5.17 Relative MSE performance as a function of average photon count per subaperture, \bar{K} , for a 2×2 detector array with read noise. The individual curves correspond to a specific read noise variance, σ_R^2 . Von Karman statistics were used for a 5×5 array of unobscured subapertures with $L_o = 50\text{m}$, $d = 9.2\text{cm}$, $\sigma_c^2/\sigma_p^2 = 1/2$, tilt removed, and overlap allowed.

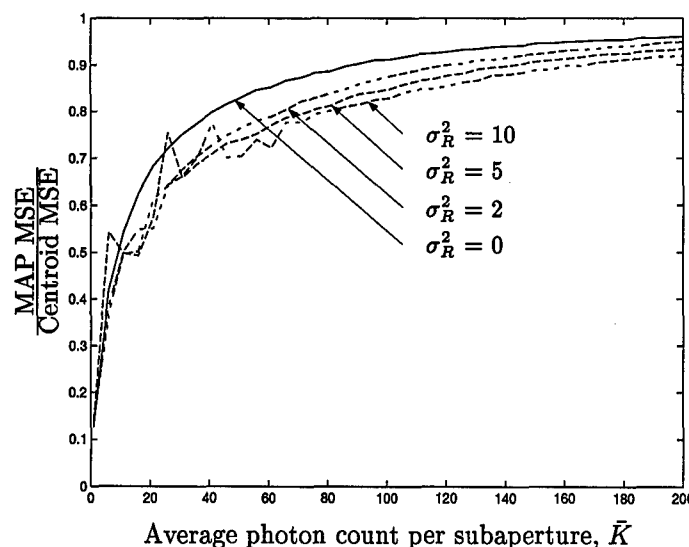


Figure 5.18 Relative MSE performance as a function of average photon count per subaperture, \bar{K} , for a 4×4 detector array with read noise. The individual curves correspond to a specific read noise variance, σ_R^2 . Von Karman statistics were used for a 5×5 array of unobscured subapertures with $L_o = 50\text{m}$, $d = 9.2\text{cm}$, $\sigma_c^2/\sigma_p^2 = 1/2$, tilt removed, and overlap allowed.

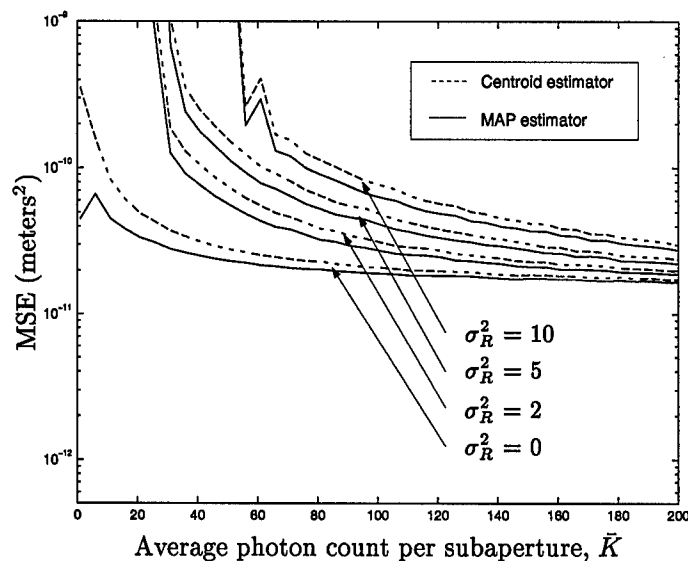


Figure 5.19 MAP and centroid estimator MSE performance as a function of average photon count per subaperture, \bar{K} , for a 4×4 detector array with read noise. The individual curves correspond to a specific read noise variance, σ_R^2 . Von Karman statistics were used for a 5×5 array of unobscured subapertures with $L_o = 50\text{m}$, $d = 9.2\text{cm}$, $\sigma_c^2/\sigma_p^2 = 1/2$, tilt removed, and overlap allowed.

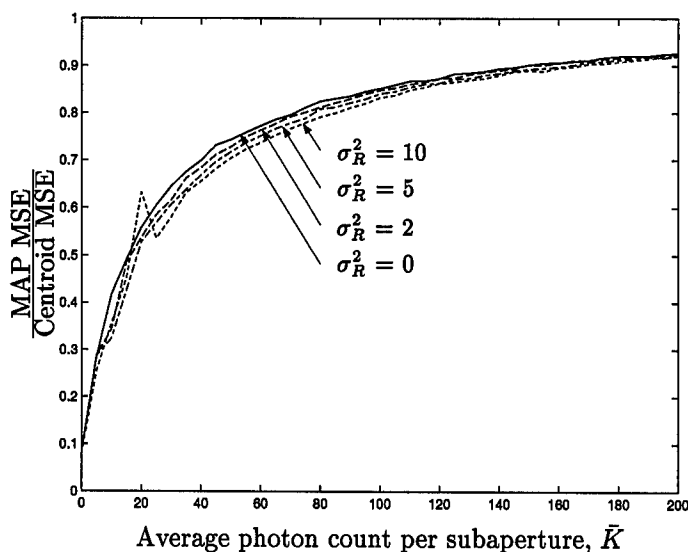


Figure 5.20 Relative MSE performance as a function of average photon count per subaperture, \bar{K} , for a 2×2 detector array with read noise. The individual curves correspond to a specific read noise variance, σ_R^2 . Von Karman statistics were used for a 5×5 array of unobscured subapertures with $L_o = 50\text{m}$, $\sigma_c^2/\sigma_p^2 = 1/4$, tilt removed, and overlap allowed.

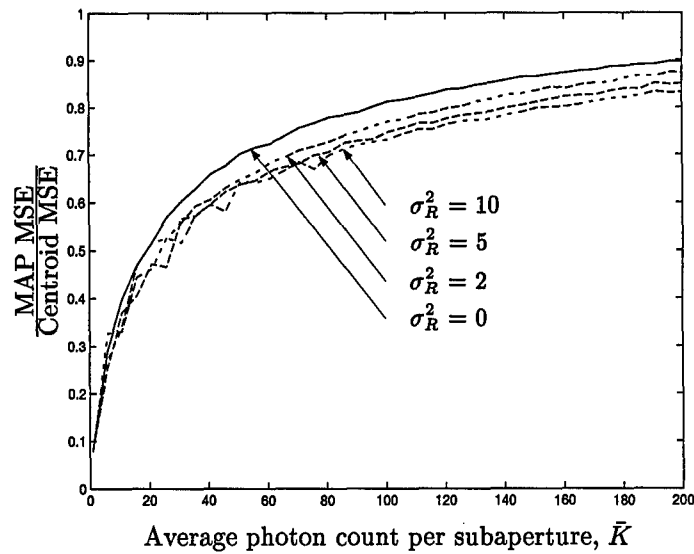


Figure 5.21 Relative MSE performance as a function of average photon count per subaperture, \bar{K} , for a 4×4 detector array with read noise. The individual curves correspond to a specific read noise variance, σ_R^2 . Von Karman statistics were used for a 5×5 array of unobscured subapertures with $L_o = 50\text{m}$, $\sigma_c^2/\sigma_p^2 = 1/4$, tilt removed, and overlap allowed.

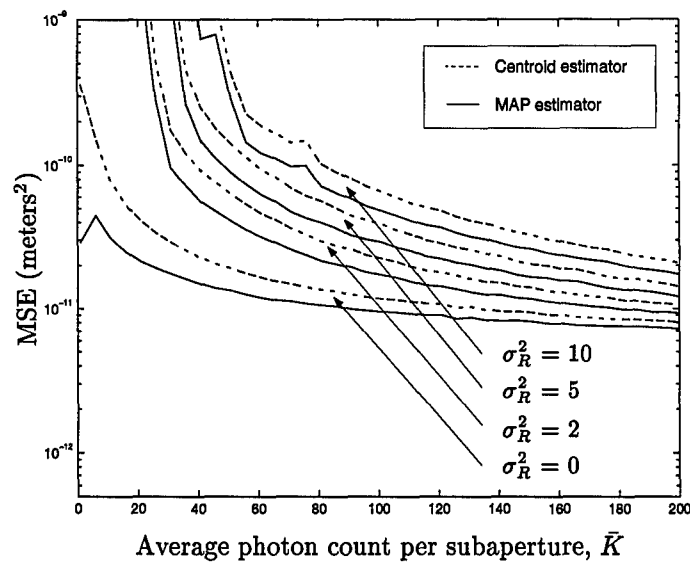


Figure 5.22 MAP and centroid estimator MSE performance as a function of average photon count per subaperture, \bar{K} , for a 4×4 detector array with read noise. The individual curves correspond to a specific read noise variance, σ_R^2 . Von Karman statistics were used for a 5×5 array of unobscured subapertures with $L_o = 50\text{m}$, $d = 9.2\text{cm}$, $\sigma_c^2/\sigma_p^2 = 1/4$, tilt removed, and overlap allowed.

5.6 Using incorrect atmospheric parameters in the MAP estimator

Up to this point, it was assumed that the atmospheric parameters were known with a high degree of certainty. This section will investigate what happens to the MSE performance when incorrect Fried parameters and outer scales were used in the development of the correlation matrix for the MAP estimator. Since the Fried parameter has greater impact on the mean square spot motion, σ_c^2 , than the outer scale, more significant effects should be observed when the incorrect Fried parameter is used.

The graphs in Figs. 5.23 and 5.26 show the results of using incorrect Fried parameter (r_o) estimates for various read noise variance for a 4×4 detector array with tilt removed from incident wavefronts, and overlap allowed. The dashed curves represent the relative MAP estimator MSE performance when the correct Fried parameter was used in the MAP estimator and the solid curves correspond to the performance when the incorrect Fried parameter was used. It was obvious that the choice of r_o has a significant impact on the performance of the MAP estimator. When r_o was estimated as higher than actual (turbulence levels are lower than estimated), there was an improvement in relative MAP estimator MSE performance. When r_o was estimated lower than actual, there was a decrease in relative MAP estimator MSE performance. The change in relative MSE performance directly resulted from the values in the slope correlation matrix varying as a function of $(1/r_o)^{5/3}$. As r_o gets smaller, the correlation values become larger. As \bar{K} becomes small, the larger correlation values force the MAP shift to zero faster than if the correct value for r_o is used. Since the slope correlation matrix determines how fast the MAP shift estimates are driven to zero as \bar{K} gets small, the choice of r_o will directly effect the relative MSE performance.

The graphs in Figs. 5.27 and 5.28 show the results of using incorrect outer scale estimates. Since the correlation values do not significantly change as the outer scale varied from 10 to 100 meters, the outer scale had little effect on the relative MAP shift estimator MSE performance.

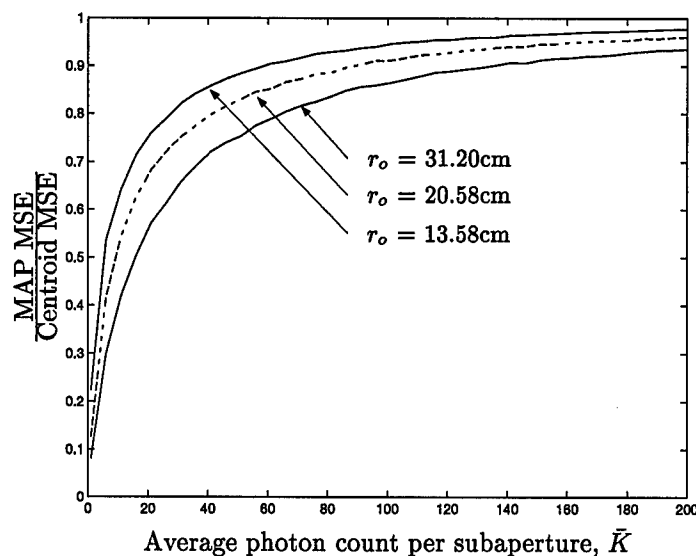


Figure 5.23 Relative MSE performance as a function of average photon count per subaperture, \bar{K} , using incorrect Fried parameters. The individual curves correspond to a particular Fried parameter, r_o . The actual Fried parameter was 20.58cm. The CCD detector array size was 4×4 . Von Karman statistics were used for a 5×5 array of unobscured subapertures with $L_o = 50\text{m}$, $d = 9.2\text{cm}$, $\sigma_R^2 = 0$, tilt removed, and overlap allowed.

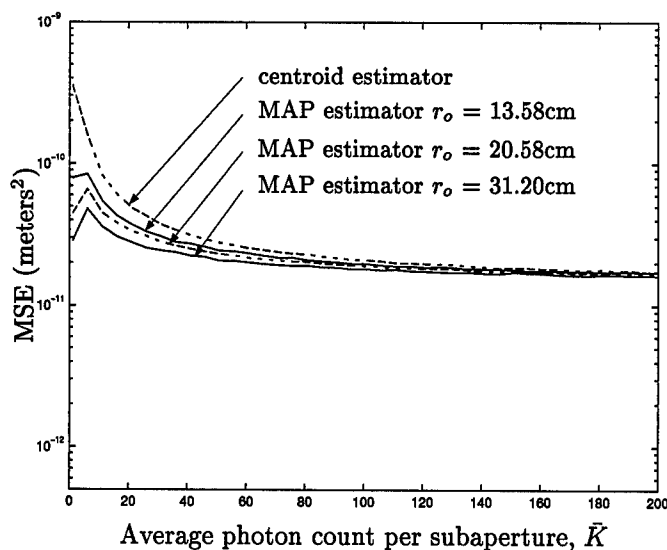


Figure 5.24 MAP and centroid MSE performance as a function of average photon count per subaperture, \bar{K} , using incorrect Fried parameters. The individual curves correspond to a particular Fried parameter, r_o . The actual Fried parameter was 20.58cm. The CCD detector array size was 4×4 . Von Karman statistics were used for a 5×5 array of unobscured subapertures with $L_o = 50\text{m}$, $d = 9.2\text{cm}$, $\sigma_R^2 = 0$, tilt removed, and overlap allowed.

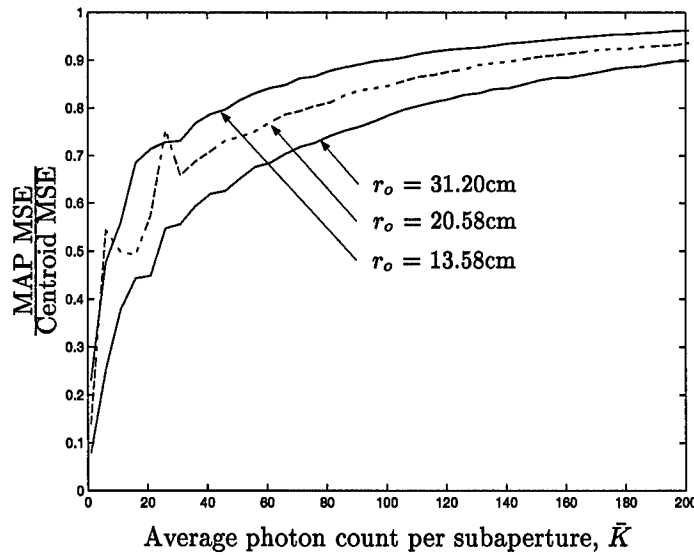


Figure 5.25 Relative MSE performance as a function of average photon count per subaperture, \bar{K} , using incorrect Fried parameters. The individual curves correspond to a particular Fried parameter, r_o . The actual Fried parameter was 20.58cm. The CCD detector array size was 4×4 . Von Karman statistics were used for a 5×5 array of unobscured subapertures with $L_o = 50\text{m}$, $d = 9.2\text{cm}$, $\sigma_R^2 = 5$, tilt removed, and overlap allowed.

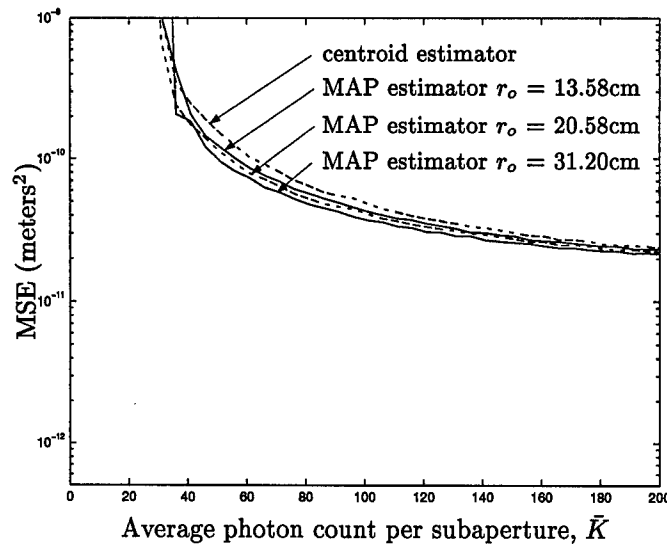


Figure 5.26 MAP and centroid MSE performance as a function of average photon count per subaperture, \bar{K} , using incorrect Fried parameters. The individual curves correspond to a particular Fried parameter, r_o . The actual Fried parameter was 20.58cm. The CCD detector array size was 4×4 . Von Karman statistics were used for a 5×5 array of unobscured subapertures with $L_o = 50\text{m}$, $d = 9.2\text{cm}$, $\sigma_R^2 = 5$, tilt removed, and overlap allowed.

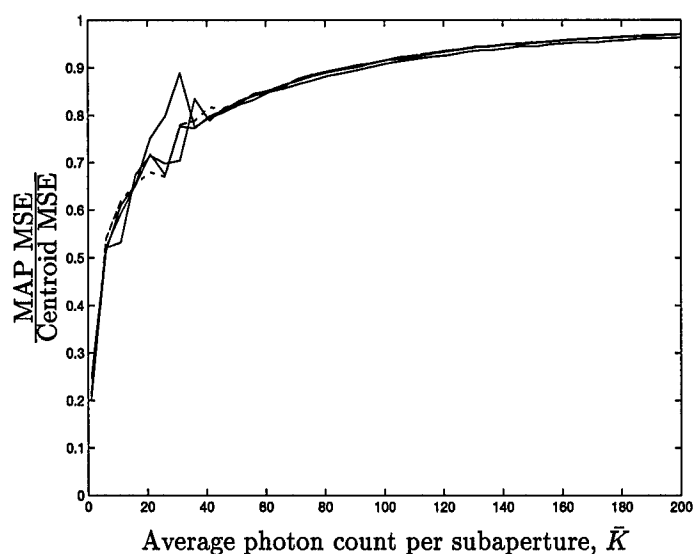


Figure 5.27 Relative MSE performance as a function of average photon count per subaperture, \bar{K} , using incorrect outer scales. The individual curves correspond to a particular outer scale value, L_o . The actual outer scale was 50m. The CCD detector array size was 2×2 . Read noise variance was 5 (photo events/pixel)². Von Karman statistics were used for a 5×5 array of unobscured subapertures with $r_o = 13.58\text{cm}$, $d = 9.2\text{cm}$, tilt removed, and overlap allowed.

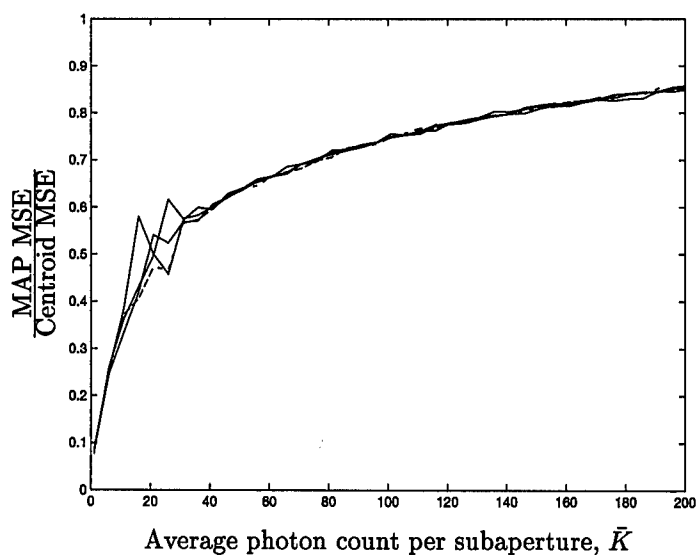


Figure 5.28 Relative MSE performance as a function of average photon count per subaperture, \bar{K} , using incorrect outer scales. The individual curves correspond to a particular outer scale value, L_o . The actual outer scale was 50m. The CCD detector array size was 4×4 . Read noise variance was 5 (photo events/pixel)². Von Karman statistics were used for a 5×5 array of unobscured subapertures with $r_o = 13.58\text{cm}$, $d = 9.2\text{cm}$, tilt removed, and overlap allowed.

5.7 SOR Generation III detector configuration

The next set of simulations examined the MSE performance when the subaperture detector array was configured to match those in the SOR generation III [19] tests. Each subaperture used a 4×4 detector array. In the modified configuration, the outer row of pixels was disabled to eliminate electronic crosstalk between subapertures. This left a 2×2 array of pixels centered on the optical axis as shown in Fig. 4.8. The performance of this modified array was compared to the performance of a conventional 4×4 detector array at various levels of read noise.

Figures 5.29 - 5.31 show that the standard 4×4 detector array had a better relative MAP estimator MSE performance than the modified detector array for all levels of read noise tested. The dashed lines correspond to the relative MSE performance when the standard 4×4 detector array was used and the solid lines correspond to the relative MSE performance when the modified detector array was used. As the read noise variance increased, the relative MSE of the standard detector array outperformed the relative MSE of the modified detector array.

However, the relative MAP estimator MSE performance does not mean that the standard 4×4 detector array had better absolute MSE performance than the modified detector array. The curves in Fig. 5.32 show that the MAP and centroid estimator MSE performance for the modified 4×4 detector array was better than the standard 4×4 detector array for non zero read noise variance. These results were not surprising since the modified detector array only had 4 pixels effected by read noise, and these pixels were all centrally located on the detector array. The standard detector array has 16 pixels, most of which are on the boundary of the detector array. Given these conditions, the standard detector array should have a higher MSE performance than the modified detector array.

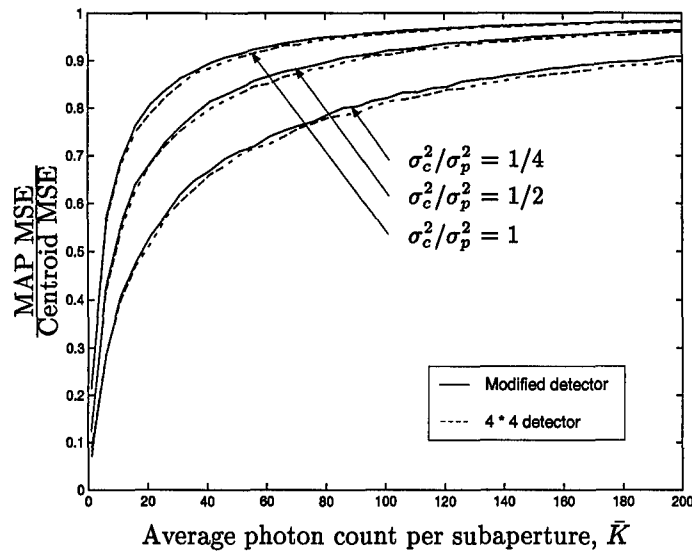


Figure 5.29 Relative MSE performance as a function of average photon count per subaperture, \bar{K} , using a SOR Generation III detector with no read noise. The pairs of curves correspond to a specific ratio of σ_c^2/σ_p^2 . Von Karman statistics were used for a 5×5 array of unobscured subapertures with $L_o = 50\text{m}$, $d = 9.2\text{cm}$, tilt removed, and overlap allowed.

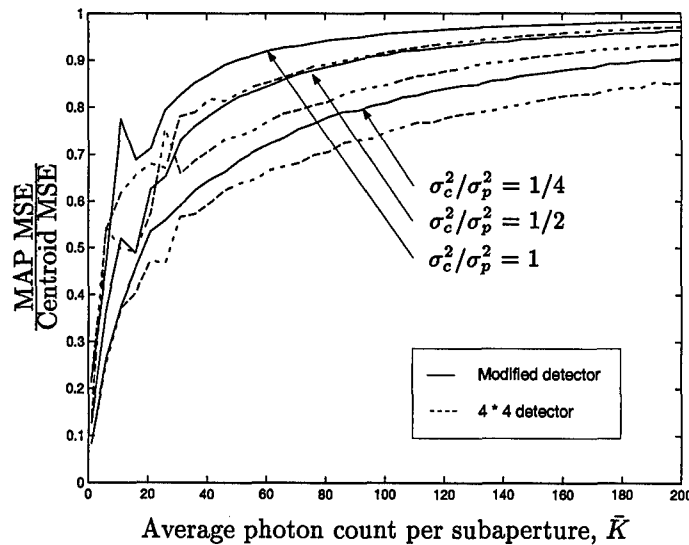


Figure 5.30 Relative MSE performance as a function of average photon count per subaperture, \bar{K} , using a SOR Generation III detector with $\sigma_R^2 = 5$. The pairs of curves correspond to a specific ratio of σ_c^2/σ_p^2 . Von Karman statistics were used for a 5×5 array of unobscured subapertures with $L_o = 50\text{m}$, $d = 9.2\text{cm}$, tilt removed, and overlap allowed.

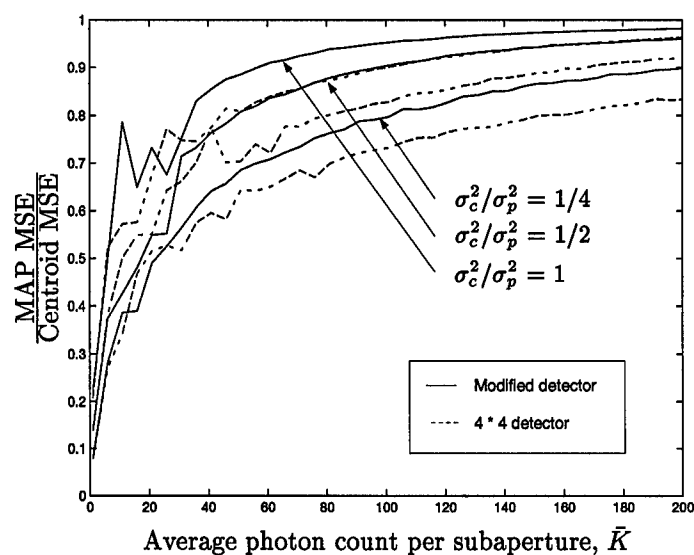


Figure 5.31 Relative MSE performance as a function of average photon count per subaperture, \bar{K} , using a SOR Generation III detector with $\sigma_R^2 = 10$. The pairs of curves correspond to a specific ratio of σ_c^2/σ_p^2 . Von Karman statistics were used for a 5×5 array of unobscured subapertures with $L_o = 50\text{m}$, $d = 9.2\text{cm}$, tilt removed, and overlap allowed.

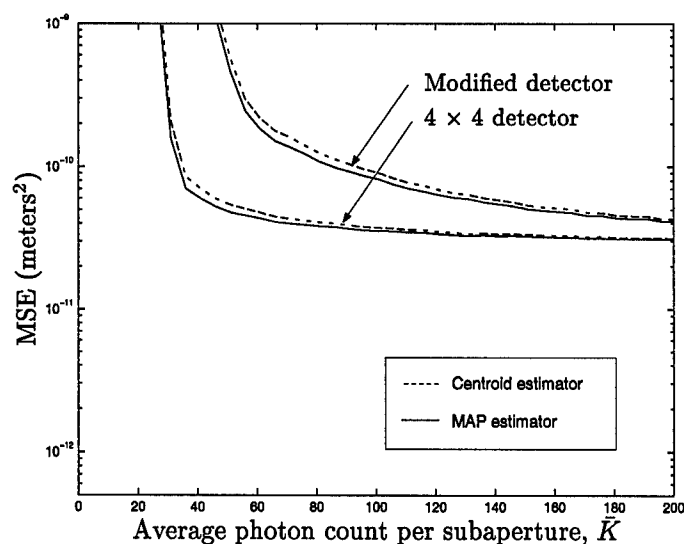


Figure 5.32 MSE performance for the MAP and the centroid estimator as a function of average photon count per subaperture, \bar{K} , for standard and modified detector arrays. The read noise variance = 10 (photons/pixel)² and $\sigma_c^2/\sigma_p^2 = 1$. Von Karman statistics were used for a 5×5 array of unobscured subapertures with $L_o = 50\text{m}$, $d = 9.2\text{cm}$, tilt removed, and overlap allowed.

VI. Conclusions

6.1 Introduction

Atmospheric turbulence reduces the resolution of imaging systems. One method to compensate for the effects of atmospheric turbulence is to remove the phase perturbations using an adaptive optics system. The two key components to remove the perturbations are the wavefront sensor and the deformable mirror. A Hartmann wavefront sensor segments the incident wavefront over an array of subapertures and measures the centroid shift in each. From this shift data, the incident wavefront can be reconstructed and the phase perturbations removed. The accuracy of the shift measurements will directly impact the accuracy of the wavefront reconstruction and the ability of the adaptive optics system to remove perturbations. A maximum *a-posteriori* (MAP) slope estimator developed by Sallberg [23] incorporated atmospheric statistics and intensity levels within the wavefront sensor to improve centroid shift estimates.

6.2 Summary of Methodology

The Hartmann wavefront sensor was modeled in simulation in order to evaluate the performance of the MAP estimator. The goal was to evaluate the MAP estimator performance using realizable wavefront sensor parameters. The MAP estimator had to be evaluated in simulation as a closed form solution for a MAP estimator using realizable wavefront sensor parameters was not possible. In addition to the wavefront sensor simulation, an implementation for the MAP estimator was developed and phase screen data was generated using von Karman atmospheric statistics and a Fourier Series phase screen generation algorithm. The MAP estimator MSE performance was examined relative to the centroid estimator MSE performance as both the wavefront sensor and atmospheric parameters were varied.

6.3 MAP estimator performance

The MAP estimator was found to perform better than the centroid estimator in all cases. Global tilt removal had minimal impact due to the decreased wavefront correlation statistics resulting from the von Karman atmospheric model. Intensity overlap onto adjacent subapertures had little effect on the relative performance of the MAP estimator as a result of the optimized parameter selection used in the wavefront sensor simulation. The relative MSE performance of the MAP estimator decreased as the number of pixels in the subaperture detector arrays were decreased. The MAP estimator was found to be less effected by read noise than the centroid estimator. When incorrect atmospheric parameters were used in the development of the MAP estimator correlation matrix, it was found that incorrect outer scale had little impact on the relative MSE performance while the selection of the Fried parameter significantly affected the relative MSE performance. Choosing r_o smaller than actual resulted in increased relative MAP estimate MSE while choosing r_o larger than actual resulted in a decrease in relative MAP estimate MSE. While the modified 4×4 detector array exhibited better overall MSE performance, the relative MAP estimator MSE performance decreased as expected. In all cases, the MAP estimator MSE performance was upper bounded by the centroid estimator MSE.

6.4 Recommendations

The feasibility of using the MAP estimator as part of a real time adaptive optics system should be studied. Real time implementation of the estimator raises several issues. These include operation with a deformable mirror using a least squares fitting algorithm in an adaptive optics system, the speed at which the MAP estimator calculation can be made, and the rate of change of the atmospheric parameters.

This thesis examined the performance of a MAP estimator using a 'snapshot' approach. Centroid shift estimates were made for individual wavefronts that were not subject to a deformable

mirror. In a real time adaptive optics system, the wavefronts will be altered by a deformable mirror prior to reaching the wavefront sensor. Since the deformable mirror will significantly change the wavefront statistics, the performance of the MAP estimator should be examined in an adaptive optics system.

Additionally, the MAP estimator inherently requires significant computational overhead. The correlation matrix for a MAP estimator implementation with a 16×16 array of subapertures will require 481 calculations. As the atmospheric parameters fluctuate, the correlation matrix will have to be updated. Since the outer scale has a minimal effect on the correlation values, the correlation matrix can be calculated for a normalized Fried parameter ($r_o = 1$) and the correlation matrix scaled as r_o changes. Another source of computational overhead arises from the additional 512^2 calculations required to make the MAP estimate. In order to decrease the number of calculations required to make the MAP shift estimate, approaches using less correlation data could be investigated.

Appendix A. Slope correlation for Kolmogorov Statistics

This appendix provides the derivation for the equations used to develop the slope correlation matrix using the Kolmogorov structure function. Beginning with Eqn. (3.11), the dot products $\hat{x} \cdot \vec{d}_{i,j}$ and $\hat{y} \cdot \vec{d}_{i,j}$ yield four possible cases that must be evaluated:

- When \vec{d}_i and \vec{d}_j denote \hat{x} directed slopes.
- When \vec{d}_i and \vec{d}_j denote \hat{y} directed slopes.
- When \vec{d}_i denotes a \hat{y} directed slope and \vec{d}_j denotes a \hat{x} directed slope.
- When \vec{d}_i denotes a \hat{x} directed slope and \vec{d}_j denotes a \hat{y} directed slope.

The first derivation will be for the correlation between subapertures with \hat{x} directed slopes. Using the notation $R_{xx} = R_{xx}(x_o, y_o)$, Eqn. (3.11) can be written as

$$\begin{aligned}
 R_{xx} = & \int \int \int \int dx dx' dy dy' \left[\frac{1}{d^2} \left(\delta(x + \frac{d}{2}) - \delta(x - \frac{d}{2}) \right) \text{rect} \left(\frac{y}{d} \right) \right] \\
 & \times \left[\frac{1}{d^2} \left(\delta(x' + \frac{d}{2} - x_o) - \delta(x' - \frac{d}{2} - x_o) \right) \text{rect} \left(\frac{y' - y_o}{d} \right) \right] \\
 & \times \left(\Gamma_\phi(0, 0) - \frac{1}{2} D_\phi(x' - x, y' - y) \right). \tag{A.1}
 \end{aligned}$$

Rearranging terms, the equation can be written

$$\begin{aligned}
 R_{xx} = & \frac{1}{d^4} \int \int \int \int dx dx' dy dy' \text{rect} \left(\frac{y}{d} \right) \text{rect} \left(\frac{y' - y_o}{d} \right) \\
 & \times \left[\delta(x + \frac{d}{2}) \delta(x' + \frac{d}{2} - x_o) - \delta(x - \frac{d}{2}) \delta(x' + \frac{d}{2} - x_o) \right. \\
 & \quad \left. - \delta(x + \frac{d}{2}) \delta(x' - \frac{d}{2} - x_o) + \delta(x - \frac{d}{2}) \delta(x' - \frac{d}{2} - x_o) \right] \\
 & \times \left(\Gamma_\phi(0, 0) - \frac{1}{2} D_\phi(x' - x, y' - y) \right). \tag{A.2}
 \end{aligned}$$

Expanding the previous equation:

$$\begin{aligned}
R_{xx} = & \frac{1}{d^4} \int \int \int \int dx dx' dy dy' \text{rect} \left(\frac{y}{d} \right) \text{rect} \left(\frac{y' - y_o}{d} \right) \\
& \times \left[\delta(x + \frac{d}{2}) \delta(x' + \frac{d}{2} - x_o) \left(\Gamma_\phi(0,0) - \frac{1}{2} D_\phi(x' - x, y' - y) \right) \right. \\
& - \delta(x - \frac{d}{2}) \delta(x' + \frac{d}{2} - x_o) \left(\Gamma_\phi(0,0) - \frac{1}{2} D_\phi(x' - x, y' - y) \right) \\
& - \delta(x + \frac{d}{2}) \delta(x' - \frac{d}{2} - x_o) \left(\Gamma_\phi(0,0) - \frac{1}{2} D_\phi(x' - x, y' - y) \right) \\
& \left. + \delta(x - \frac{d}{2}) \delta(x' - \frac{d}{2} - x_o) \left(\Gamma_\phi(0,0) - \frac{1}{2} D_\phi(x' - x, y' - y) \right) \right]. \quad (\text{A.3})
\end{aligned}$$

The derivation will make use of the Kolmogorov phase structure function:

$$D_\phi(x' - x, y' - y) = 6.88 \left(\frac{\sqrt{(x' - x)^2 + (y' - y)^2}}{r_o} \right)^{\frac{5}{3}}. \quad (\text{A.4})$$

Using the sifting property of dirac delta functions [12] and recognizing that $\Gamma_\phi(0,0)$ factors out,

Eqn. (A.3) can be written as

$$\begin{aligned}
R_{xx} = & \frac{-3.44}{d^4} \left(\frac{1}{r_o} \right)^{\frac{5}{3}} \int \int dy dy' \text{rect} \left(\frac{y}{d} \right) \text{rect} \left(\frac{y' - y_o}{d} \right) \\
& \times \left[\left(\left(-\frac{d}{2} + x_o + \frac{d}{2} \right)^2 + (y' - y)^2 \right)^{\frac{5}{6}} - \left(\left(-\frac{d}{2} + x_o - \frac{d}{2} \right)^2 + (y' - y)^2 \right)^{\frac{5}{6}} \right. \\
& \left. - \left(\left(\frac{d}{2} + x_o + \frac{d}{2} \right)^2 + (y' - y)^2 \right)^{\frac{5}{6}} + \left(\left(\frac{d}{2} + x_o - \frac{d}{2} \right)^2 + (y' - y)^2 \right)^{\frac{5}{6}} \right]. \quad (\text{A.5})
\end{aligned}$$

Combining like terms

$$\begin{aligned}
R_{xx} = & \frac{-3.44}{d^4} \left(\frac{1}{r_o} \right)^{\frac{5}{3}} \int \int dy dy' \text{rect} \left(\frac{y}{d} \right) \text{rect} \left(\frac{y' - y_o}{d} \right) \left[2 (x_o^2 + (y' - y)^2)^{\frac{5}{6}} \right. \\
& \left. - ((x_o + d)^2 + (y' - y)^2)^{\frac{5}{6}} - ((x_o - d)^2 + (y' - y)^2)^{\frac{5}{6}} \right]. \quad (\text{A.6})
\end{aligned}$$

Perform the following change of variables:

$$\begin{aligned}\Sigma_y &= \frac{y' + y}{2} \quad \text{and} \quad \Delta_y = y' - y, \\ y' &= \Sigma_y + \frac{\Delta_y}{2} \quad \text{and} \quad y = \Sigma_y - \frac{\Delta_y}{2}.\end{aligned}\tag{A.7}$$

The Jacobian is 1 and the equation becomes

$$\begin{aligned}R_{xx} &= \frac{-3.44}{d^4} \left(\frac{1}{r_o} \right)^{\frac{5}{3}} \int \int d\Delta_y d\Sigma_y \text{rect} \left(\frac{\Sigma_y - \frac{\Delta_y}{2}}{d} \right) \text{rect} \left(\frac{\Sigma_y + \frac{\Delta_y}{2} - y_o}{d} \right) \\ &\quad \times \left[2 (x_o^2 + (\Delta_y)^2)^{\frac{5}{6}} - ((x_o + d)^2 + (y' - y)^2)^{\frac{5}{6}} \right. \\ &\quad \left. - ((x_o - d)^2 + (y' - y)^2)^{\frac{5}{6}} \right].\end{aligned}\tag{A.8}$$

The equation can be simplified to a single integral by eliminating one variable. Consider the terms in the previous equation that depend only on Σ_y :

$$\int d\Sigma_y \text{rect} \left(\frac{\Sigma_y - \frac{\Delta_y}{2}}{d} \right) \text{rect} \left(\frac{\Sigma_y + \frac{\Delta_y}{2} - y_o}{d} \right).\tag{A.9}$$

Define:

$$\alpha = \frac{\Sigma_y - \frac{\Delta_y}{2}}{d} \quad \text{and} \quad d\alpha = \frac{1}{d} d\Sigma_y.\tag{A.10}$$

The equation can then be written as

$$d \int d\alpha \text{rect}(\alpha) \text{rect} \left(\alpha - \frac{(-\Delta_y + y_o)}{d} \right).\tag{A.11}$$

Since $(-\Delta_y + y_o)/d$ is constant, this integral is the correlation of the two rect functions. Referencing Goodman and using Fourier Transform analysis, the integral becomes

$$\int d\Sigma_y \text{ rect} \left(\frac{\Sigma_y - \frac{\Delta_y}{2}}{d} \right) \text{ rect} \left(\frac{\Sigma_y + \frac{\Delta_y}{2} - y_o}{d} \right) = d \text{tri} \left(\frac{-\Delta_y + y_o}{d} \right). \quad (\text{A.12})$$

The triangle function defines the limits of the remaining integral:

$$\text{tri} \left(\frac{-\Delta_y + y_o}{d} \right) = \begin{cases} \left(\frac{d - |-\Delta_y + y_o|}{d} \right) & y_o - d \leq \Delta_y \leq y_o + d \\ 0 & \text{otherwise} \end{cases} \quad (\text{A.13})$$

Substituting this into Eqn. (A.8)

$$\begin{aligned} R_{xx} = & \frac{-3.44}{d^4} \left(\frac{1}{r_o} \right)^{\frac{5}{8}} \int_{y_o-d}^{y_o+d} d\Delta_y d \left(\frac{d - |-\Delta_y + y_o|}{d} \right) \left[2 (x_o^2 + (y' - y)^2)^{\frac{5}{8}} \right. \\ & \left. - ((x_o + d)^2 + (y' - y)^2)^{\frac{5}{8}} - ((x_o - d)^2 + (y' - y)^2)^{\frac{5}{8}} \right]. \end{aligned} \quad (\text{A.14})$$

Perform the following change of variables to put the integral in dimensionless quantities:

$$\begin{aligned} \tilde{x}_o &= \frac{x_o}{d} & \tilde{y}_o &= \frac{y_o}{d}, \\ \Delta_{\tilde{y}} &= \frac{\Delta_y}{d} & d\Delta_{\tilde{y}} &= \frac{d\Delta_y}{d}. \end{aligned} \quad (\text{A.15})$$

The final equation for the correlation between subapertures with \hat{x} directed slopes is

$$\begin{aligned} R_{xx} = & \frac{-3.44}{d^2} \left(\frac{d}{r_o} \right)^{\frac{5}{8}} \int_{\tilde{y}_o-1}^{\tilde{y}_o+1} d\Delta_{\tilde{y}} (1 - |\Delta_{\tilde{y}} - \tilde{y}_o|) \\ & \times \left[2 (\tilde{x}_o^2 + \Delta_{\tilde{y}}^2)^{\frac{5}{8}} - ((\tilde{x}_o + 1)^2 + \Delta_{\tilde{y}}^2)^{\frac{5}{8}} - ((\tilde{x}_o - 1)^2 + \Delta_{\tilde{y}}^2)^{\frac{5}{8}} \right], \end{aligned} \quad (\text{A.16})$$

where R_{xx} is a function of \tilde{x}_o and \tilde{y}_o , the normalized \hat{x} and \hat{y} separation of the subapertures. The development of the correlation when both subapertures have \hat{y} directed slopes, $\vec{d}_i, \vec{d}_j = \hat{y}$, is identical. The result can simply be written as

$$R_{yy} = \frac{-3.44}{d^2} \left(\frac{d}{r_o} \right)^{\frac{5}{3}} \int_{\tilde{x}_o-1}^{\tilde{x}_o+1} d\Delta_{\tilde{x}} (1 - |\Delta_{\tilde{x}} - \tilde{x}_o|) \times \left[2(\tilde{y}_o^2 + \Delta_{\tilde{x}}^2)^{\frac{5}{6}} - ((\tilde{y}_o + 1)^2 + \Delta_{\tilde{x}}^2)^{\frac{5}{6}} - ((\tilde{y}_o - 1)^2 + \Delta_{\tilde{x}}^2)^{\frac{5}{6}} \right]. \quad (\text{A.17})$$

The development for correlations when subapertures have slopes in orthogonal directions follows. The specific case for correlation between \hat{y} directed slope and \hat{x} directed slope follows. With $\vec{d}_i = \hat{y}$ and $\vec{d}_j = \hat{x}$, the cross correlation equations can be found. Using the notation $R_{yx} = R_{yx}(x_o, y_o)$, Eqn. (3.11) can be written as

$$R_{yx} = \int \int \int \int dx dx' dy dy' \left(\frac{1}{d^2} \left(\delta(x + \frac{d}{2}) - \delta(x - \frac{d}{2}) \right) \text{rect} \left(\frac{y}{d} \right) \right) \times \left(\frac{1}{d^2} \left(\delta(y' + \frac{d}{2} - y_o) - \delta(y' - \frac{d}{2} - y_o) \right) \text{rect} \left(\frac{x' - x_o}{d} \right) \right) \times \left(\Gamma_{\phi}(0, 0) - \frac{1}{2} D_{\phi}(x - x', y - y') \right). \quad (\text{A.18})$$

Rearranging terms, the equation can be written

$$R_{yx} = \frac{1}{d^4} \int \int \int \int dx dx' dy dy' \text{rect} \left(\frac{y}{d} \right) \text{rect} \left(\frac{x' - x_o}{d} \right) \times \left[\delta(x + \frac{d}{2}) \delta(y' + \frac{d}{2} - y_o) - \delta(x + \frac{d}{2}) \delta(y' - \frac{d}{2} - y_o) - \delta(x - \frac{d}{2}) \delta(y' + \frac{d}{2} - y_o) + \delta(x - \frac{d}{2}) \delta(y' - \frac{d}{2} - y_o) \right] \times \left(\Gamma_{\phi}(0, 0) - \frac{1}{2} D_{\phi}(x - x', y - y') \right). \quad (\text{A.19})$$

After substituting in the structure function from Eqn. (A.4) and using the sifting property of dirac delta functions [12], the equation can be reduced to a double integration. Unlike the correlation between subapertures with slopes in the same direction, this equation will not reduce to a single integration.

$$\begin{aligned}
 R_{yx} = & \frac{-3.44}{d^4} \left(\frac{1}{r_o} \right)^{\frac{5}{8}} \int \int dx' dy \operatorname{rect} \left(\frac{x' - x_o}{d} \right) \operatorname{rect} \left(\frac{y}{d} \right) \\
 & \times \left[\left(\left(x' + \frac{d}{2} \right)^2 + \left(-\frac{d}{2} + y_o - y \right)^2 \right)^{\frac{5}{8}} - \left(\left(x' + \frac{d}{2} \right)^2 + \left(\frac{d}{2} + y_o - y \right)^2 \right)^{\frac{5}{8}} \right. \\
 & \left. - \left(\left(x' - \frac{d}{2} \right)^2 + \left(-\frac{d}{2} + y_o - y \right)^2 \right)^{\frac{5}{8}} + \left(\left(x' - \frac{d}{2} \right)^2 + \left(\frac{d}{2} + y_o - y \right)^2 \right)^{\frac{5}{8}} \right]. \quad (\text{A.20})
 \end{aligned}$$

The rect functions define the limits of integration:

$$\begin{aligned}
 R_{yx} = & \frac{-3.44}{d^4} \left(\frac{1}{r_o} \right)^{\frac{5}{8}} \int_{-\frac{d}{2}}^{\frac{d}{2}} \int_{x_o - \frac{d}{2}}^{x_o + \frac{d}{2}} dx' dy \\
 & \times \left[\left(\left(x' + \frac{d}{2} \right)^2 + \left(-\frac{d}{2} + y_o - y \right)^2 \right)^{\frac{5}{8}} - \left(\left(x' + \frac{d}{2} \right)^2 + \left(\frac{d}{2} + y_o - y \right)^2 \right)^{\frac{5}{8}} \right. \\
 & \left. - \left(\left(x' - \frac{d}{2} \right)^2 + \left(-\frac{d}{2} + y_o - y \right)^2 \right)^{\frac{5}{8}} + \left(\left(x' - \frac{d}{2} \right)^2 + \left(\frac{d}{2} + y_o - y \right)^2 \right)^{\frac{5}{8}} \right]. \quad (\text{A.21})
 \end{aligned}$$

Perform the following change of variables to put the integral in dimensionless quantities:

$$\begin{aligned}
 \tilde{x}_o &= \frac{x_o}{d} \quad \text{and} \quad \tilde{y}_o = \frac{y_o}{d}, \\
 \tilde{x} &= \frac{x}{d} \quad \text{and} \quad d\tilde{x} = \frac{dx}{d} \\
 \tilde{y} &= \frac{y}{d} \quad \text{and} \quad d\tilde{y} = \frac{dy}{d}.
 \end{aligned} \quad (\text{A.22})$$

The correlation between \hat{y} directed slope and \hat{x} directed slope is

$$\begin{aligned}
R_{yx} = & \frac{-3.44}{d^2} \left(\frac{d}{r_o} \right)^{\frac{5}{8}} \int_{-\frac{1}{2}}^{\frac{1}{2}} \int_{\tilde{x}_o - \frac{1}{2}}^{\tilde{x}_o + \frac{1}{2}} d\tilde{x}' d\tilde{y} \\
& \times \left[\left(\left(\tilde{x}' + \frac{1}{2} \right)^2 + \left(-\frac{1}{2} + \tilde{y}_o - \tilde{y} \right)^2 \right)^{\frac{5}{8}} - \left(\left(\tilde{x}' + \frac{1}{2} \right)^2 + \left(\frac{1}{2} + \tilde{y}_o - \tilde{y} \right)^2 \right)^{\frac{5}{8}} \right. \\
& \left. - \left(\left(\tilde{x}' - \frac{1}{2} \right)^2 + \left(-\frac{1}{2} + \tilde{y}_o - \tilde{y} \right)^2 \right)^{\frac{5}{8}} + \left(\left(\tilde{x}' - \frac{1}{2} \right)^2 + \left(\frac{1}{2} + \tilde{y}_o - \tilde{y} \right)^2 \right)^{\frac{5}{8}} \right], \quad (\text{A.23})
\end{aligned}$$

where R_{yx} is a function of \tilde{x}_o and \tilde{y}_o , the normalized \hat{x} and \hat{y} separation of the subapertures. The correlation between subapertures with a \hat{x} directed slope and a \hat{y} directed slope is developed in the same manner.

$$\begin{aligned}
R_{xy} = & \frac{-3.44}{d^2} \left(\frac{d}{r_o} \right)^{\frac{5}{8}} \int_{-\frac{1}{2}}^{\frac{1}{2}} \int_{\tilde{y}_o - \frac{1}{2}}^{\tilde{y}_o + \frac{1}{2}} d\tilde{y}' d\tilde{x} \\
& \times \left[\left(\left(\tilde{y}' + \frac{1}{2} \right)^2 + \left(-\frac{1}{2} + \tilde{x}_o - \tilde{x} \right)^2 \right)^{\frac{5}{8}} - \left(\left(\tilde{y}' + \frac{1}{2} \right)^2 + \left(\frac{1}{2} + \tilde{x}_o - \tilde{x} \right)^2 \right)^{\frac{5}{8}} \right. \\
& \left. - \left(\left(\tilde{y}' - \frac{1}{2} \right)^2 + \left(-\frac{1}{2} + \tilde{x}_o - \tilde{x} \right)^2 \right)^{\frac{5}{8}} + \left(\left(\tilde{y}' - \frac{1}{2} \right)^2 + \left(\frac{1}{2} + \tilde{x}_o - \tilde{x} \right)^2 \right)^{\frac{5}{8}} \right]. \quad (\text{A.24})
\end{aligned}$$

Appendix B. Slope correlation for von Karman Statistics

This appendix provides the derivation for the equations used to develop the slope correlation matrix for the slope correlation matrix using the Von Karman structure function. Beginning with Eqn.(3.11), the dot products $\hat{x} \cdot \vec{d}_{i,j}$ and $\hat{y} \cdot \vec{d}_{i,j}$ yield four possible cases that must be evaluated:

- When \vec{d}_i and \vec{d}_j denote \hat{x} directed slopes.
- When \vec{d}_i and \vec{d}_j denote \hat{y} directed slopes.
- When \vec{d}_i denotes a \hat{y} directed slope and \vec{d}_j denotes a \hat{x} directed slope.
- When \vec{d}_i denotes a \hat{x} directed slope and \vec{d}_j denotes a \hat{y} directed slope.

The first derivation will be for the correlation between subapertures with \hat{x} directed slopes. Using the notation $R_{xx} = R_{xx}(x_o, y_o)$, Eqn. (3.11) can be written as

$$\begin{aligned}
 R_{xx} = & \int \int \int \int dx dx' dy dy' \left[\frac{1}{d^2} \left(\delta(x + \frac{d}{2}) - \delta(x - \frac{d}{2}) \right) \text{rect} \left(\frac{y}{d} \right) \right] \\
 & \times \left[\frac{1}{d^2} \left(\delta(x' + \frac{d}{2} - x_o) - \delta(x' - \frac{d}{2} - x_o) \right) \text{rect} \left(\frac{y' - y_o}{d} \right) \right] \\
 & \times \left(\Gamma_\phi(0, 0) - \frac{1}{2} D_\phi(x' - x, y' - y) \right). \tag{B.1}
 \end{aligned}$$

Rearranging terms, the equation can be written

$$\begin{aligned}
 R_{xx} = & \frac{1}{d^4} \int \int \int \int dx dx' dy dy' \text{rect} \left(\frac{y}{d} \right) \text{rect} \left(\frac{y' - y_o}{d} \right) \\
 & \times \left[\delta(x + \frac{d}{2}) \delta(x' + \frac{d}{2} - x_o) - \delta(x - \frac{d}{2}) \delta(x' + \frac{d}{2} - x_o) \right. \\
 & \quad \left. - \delta(x + \frac{d}{2}) \delta(x' - \frac{d}{2} - x_o) + \delta(x - \frac{d}{2}) \delta(x' - \frac{d}{2} - x_o) \right] \\
 & \times \left(\Gamma_\phi(0, 0) - \frac{1}{2} D_\phi(x' - x, y' - y) \right). \tag{B.2}
 \end{aligned}$$

Expanding the previous equation,

$$\begin{aligned}
R_{xx} = & \frac{1}{d^4} \int \int \int \int dx dx' dy dy' \text{rect} \left(\frac{y}{d} \right) \text{rect} \left(\frac{y' - y_o}{d} \right) \\
& \times \left[\delta(x + \frac{d}{2}) \delta(x' + \frac{d}{2} - x_o) \left(\Gamma_\phi(0, 0) - \frac{1}{2} D_\phi(x' - x, y' - y) \right) \right. \\
& \quad - \delta(x - \frac{d}{2}) \delta(x' + \frac{d}{2} - x_o) \left(\Gamma_\phi(0, 0) - \frac{1}{2} D_\phi(x' - x, y' - y) \right) \\
& \quad - \delta(x + \frac{d}{2}) \delta(x' - \frac{d}{2} - x_o) \left(\Gamma_\phi(0, 0) - \frac{1}{2} D_\phi(x' - x, y' - y) \right) \\
& \quad \left. + \delta(x - \frac{d}{2}) \delta(x' - \frac{d}{2} - x_o) \left(\Gamma_\phi(0, 0) - \frac{1}{2} D_\phi(x' - x, y' - y) \right) \right]. \quad (\text{B.3})
\end{aligned}$$

The derivation will make use of the von Karman phase structure function [30]:

$$D_\phi(\vec{x}) = \frac{3.089}{(2\pi)^{\frac{5}{3}}} \frac{6}{5} \left(\frac{L_o}{r_o} \right)^{\frac{5}{3}} \left(1 - \frac{\Gamma[1/6]}{\pi^{\frac{1}{6}}} \left(\frac{|\vec{x}|}{L_o} \right)^{\frac{5}{6}} K_{5/6} \left[2\pi \frac{|\vec{x}|}{L_o} \right] \right), \quad (\text{B.4})$$

where $\Gamma[\cdot]$ is the Gamma function, $K_{5/6}[\cdot]$ is a modified Bessel function of the second kind of order 5/6, L_o is the outer scale parameter, r_o is the Fried parameter, and $|\vec{x}| = \sqrt{(x' - x)^2 + (y' - y)^2}$.

Using the sifting property of dirac delta functions [12] and recognizing that $\Gamma_\phi(0, 0)$ factors out, Eqn. (B.3) can be written as

$$\begin{aligned}
R_{xx} = & 0.08663 \left(\frac{L_o}{r_o} \right)^{\frac{5}{3}} \frac{1}{d^4} \int \int dy dy' \text{rect} \left(\frac{y}{d} \right) \text{rect} \left(\frac{y' - y_o}{d} \right) \\
& \times \left[\left(1 - \frac{\Gamma[1/6]}{\pi^{\frac{1}{6}}} \left(\frac{\sqrt{(x_o - d)^2 + (y' - y)^2}}{L_o} \right)^{\frac{5}{6}} K_{5/6} \left[2\pi \frac{\sqrt{(x_o - d)^2 + (y' - y)^2}}{L_o} \right] \right) \right. \\
& \quad + \left(1 - \frac{\Gamma[1/6]}{\pi^{\frac{1}{6}}} \left(\frac{\sqrt{(x_o + d)^2 + (y' - y)^2}}{L_o} \right)^{\frac{5}{6}} K_{5/6} \left[2\pi \frac{\sqrt{(x_o + d)^2 + (y' - y)^2}}{L_o} \right] \right) \\
& \quad \left. - 2 \left(1 - \frac{\Gamma[1/6]}{\pi^{\frac{1}{6}}} \left(\frac{\sqrt{x_o^2 + (y' - y)^2}}{L_o} \right)^{\frac{5}{6}} K_{5/6} \left[2\pi \frac{\sqrt{x_o^2 + (y' - y)^2}}{L_o} \right] \right) \right]. \quad (\text{B.5})
\end{aligned}$$

Perform the following change of variables:

$$\begin{aligned}\Sigma_y &= \frac{y' + y}{2} \quad \text{and} \quad \Delta_y = y' - y, \\ y' &= \Sigma_y + \frac{\Delta_y}{2} \quad \text{and} \quad y = \Sigma_y - \frac{\Delta_y}{2}.\end{aligned}\tag{B.6}$$

The Jacobian is 1 and the equation becomes

$$\begin{aligned}R_{xx} &= 0.08663 \left(\frac{L_o}{r_o}\right)^{\frac{5}{6}} \frac{1}{d^4} \int \int d\Delta_y d\Sigma_y \text{rect}\left(\frac{\Sigma_y - \frac{\Delta_y}{2}}{d}\right) \text{rect}\left(\frac{\Sigma_y + \frac{\Delta_y}{2} - y_o}{d}\right) \\ &\times \left[2 \frac{\Gamma[1/6]}{\pi^{\frac{1}{6}}} \left(\frac{\sqrt{x_o^2 + (\Delta_y)^2}}{L_o}\right)^{\frac{5}{6}} K_{5/6} \left[2\pi \frac{\sqrt{x_o^2 + (\Delta_y)^2}}{L_o} \right] \right. \\ &\quad - \frac{\Gamma[1/6]}{\pi^{\frac{1}{6}}} \left(\frac{\sqrt{(x_o + d)^2 + (\Delta_y)^2}}{L_o}\right)^{\frac{5}{6}} K_{5/6} \left[2\pi \frac{\sqrt{(x_o + d)^2 + (\Delta_y)^2}}{L_o} \right] \\ &\quad \left. - \frac{\Gamma[1/6]}{\pi^{\frac{1}{6}}} \left(\frac{\sqrt{(x_o - d)^2 + (\Delta_y)^2}}{L_o}\right)^{\frac{5}{6}} K_{5/6} \left[2\pi \frac{\sqrt{(x_o - d)^2 + (\Delta_y)^2}}{L_o} \right] \right].\end{aligned}\tag{B.7}$$

The previous equation can be simplified to a single integral by eliminating one variable. Consider the terms that depend only on Σ_y :

$$\int d\Sigma_y \text{rect}\left(\frac{\Sigma_y - \frac{\Delta_y}{2}}{d}\right) \text{rect}\left(\frac{\Sigma_y + \frac{\Delta_y}{2} - y_o}{d}\right).\tag{B.8}$$

Define:

$$\alpha = \frac{\Sigma_y - \frac{\Delta_y}{2}}{d} \quad \text{and} \quad d\alpha = \frac{1}{d} d\Sigma_y.\tag{B.9}$$

Equation (B.8) can then be written as

$$d \int d\alpha \text{rect}(\alpha) \text{rect}\left(\alpha - \frac{(-\Delta_y + y_o)}{d}\right).\tag{B.10}$$

Since $(-\Delta_y + y_o)/d$ is constant, this integral is the correlation of the two rect functions. Referencing Goodman and using Fourier Transform analysis, the integral becomes:

$$\int d\Sigma_y \text{rect}\left(\frac{\Sigma_y - \frac{\Delta_y}{2}}{d}\right) \text{rect}\left(\frac{\Sigma_y + \frac{\Delta_y}{2} - y_o}{d}\right) = d \text{tri}\left(\frac{-\Delta_y + y_o}{d}\right). \quad (\text{B.11})$$

The triangle function defines the limits of the remaining integral:

$$\text{tri}\left(\frac{-\Delta_y + y_o}{d}\right) = \begin{cases} \left(\frac{d - |-\Delta_y + y_o|}{d}\right) & y_o - d \leq \Delta_y \leq y_o + d \\ 0 & \text{otherwise.} \end{cases} \quad (\text{B.12})$$

Substituting this into Eqn. (B.7):

$$\begin{aligned} R_{xx} = & 0.08663 \left(\frac{L_o}{r_o}\right)^{\frac{5}{6}} \frac{1}{d^4} \int_{y_o-d}^{y_o+d} d\Delta_y d \left(\frac{d - |-\Delta_y + y_o|}{d}\right) \\ & \left[2 \frac{\Gamma[1/6]}{\pi^{\frac{1}{6}}} \left(\frac{\sqrt{x_o^2 + (\Delta_y)^2}}{L_o}\right)^{\frac{5}{6}} K_{5/6} \left[2\pi \frac{\sqrt{x_o^2 + (\Delta_y)^2}}{L_o} \right] \right. \\ & - \frac{\Gamma[1/6]}{\pi^{\frac{1}{6}}} \left(\frac{\sqrt{(x_o + d)^2 + (\Delta_y)^2}}{L_o}\right)^{\frac{5}{6}} K_{5/6} \left[2\pi \frac{\sqrt{(x_o + d)^2 + (\Delta_y)^2}}{L_o} \right] \\ & \left. - \frac{\Gamma[1/6]}{\pi^{\frac{1}{6}}} \left(\frac{\sqrt{(x_o - d)^2 + (\Delta_y)^2}}{L_o}\right)^{\frac{5}{6}} K_{5/6} \left[2\pi \frac{\sqrt{(x_o - d)^2 + (\Delta_y)^2}}{L_o} \right] \right]. \quad (\text{B.13}) \end{aligned}$$

Perform the following change of variables to put the limits of integration in dimensionless quantities:

$$\begin{aligned} \tilde{x}_o &= \frac{x_o}{d} \quad \text{and} \quad \tilde{y}_o = \frac{y_o}{d}, \\ \Delta_{\tilde{y}} &= \frac{\Delta_y}{d} \quad \text{and} \quad d\Delta_{\tilde{y}} = \frac{d\Delta_y}{d}. \end{aligned} \quad (\text{B.14})$$

The final equation for the correlation between subapertures with \hat{x} directed slopes is:

$$\begin{aligned}
R_{xx} = & 0.08663 \left(\frac{L_o}{r_o} \right)^{\frac{5}{6}} \frac{1}{d^2} \left(\frac{\Gamma[1/6]}{\pi^{\frac{1}{6}}} \right) \int_{\tilde{y}_o-1}^{\tilde{y}_o+1} d\Delta_{\tilde{y}} (1 - |\Delta_{\tilde{y}} - \tilde{y}_o|) \\
& \left[2 \left(\frac{d\sqrt{\tilde{x}_o^2 + (\Delta_{\tilde{y}})^2}}{L_o} \right)^{\frac{5}{6}} K_{5/6} \left[2\pi \frac{d\sqrt{\tilde{x}_o^2 + (\Delta_{\tilde{y}})^2}}{L_o} \right] \right. \\
& - \left(\frac{d\sqrt{(\tilde{x}_o + 1)^2 + (\Delta_{\tilde{y}})^2}}{L_o} \right)^{\frac{5}{6}} K_{5/6} \left[2\pi \frac{d\sqrt{(\tilde{x}_o + 1)^2 + (\Delta_{\tilde{y}})^2}}{L_o} \right] \\
& \left. - \left(\frac{d\sqrt{(\tilde{x}_o - 1)^2 + (\Delta_{\tilde{y}})^2}}{L_o} \right)^{\frac{5}{6}} K_{5/6} \left[2\pi \frac{d\sqrt{(\tilde{x}_o - 1)^2 + (\Delta_{\tilde{y}})^2}}{L_o} \right] \right]. \quad (B.15)
\end{aligned}$$

where R_{xx} is a function of \tilde{x}_o and \tilde{y}_o , the normalized \hat{x} and \hat{y} separation of the subapertures.

The development of the correlation between subapertures with \hat{y} directed slopes, \vec{d}_i and $\vec{d}_j = \hat{y}$, is identical. The result can simply be written as

$$\begin{aligned}
R_{yy} = & 0.08663 \left(\frac{L_o}{r_o} \right)^{\frac{5}{6}} \frac{1}{d^2} \left(\frac{\Gamma[1/6]}{\pi^{\frac{1}{6}}} \right) \int_{\tilde{x}_o-1}^{\tilde{x}_o+1} d\Delta_{\tilde{x}} (1 - |\Delta_{\tilde{x}} - \tilde{x}_o|) \\
& \times \left[2 \left(\frac{d\sqrt{\tilde{y}_o^2 + (\Delta_{\tilde{x}})^2}}{L_o} \right)^{\frac{5}{6}} K_{5/6} \left[2\pi \frac{d\sqrt{\tilde{y}_o^2 + (\Delta_{\tilde{x}})^2}}{L_o} \right] \right. \\
& - \left(\frac{d\sqrt{(\tilde{y}_o + 1)^2 + (\Delta_{\tilde{x}})^2}}{L_o} \right)^{\frac{5}{6}} K_{5/6} \left[2\pi \frac{d\sqrt{(\tilde{y}_o + 1)^2 + (\Delta_{\tilde{x}})^2}}{L_o} \right] \\
& \left. - \left(\frac{d\sqrt{(\tilde{y}_o - 1)^2 + (\Delta_{\tilde{x}})^2}}{L_o} \right)^{\frac{5}{6}} K_{5/6} \left[2\pi \frac{d\sqrt{(\tilde{y}_o - 1)^2 + (\Delta_{\tilde{x}})^2}}{L_o} \right] \right]. \quad (B.16)
\end{aligned}$$

The correlation between subapertures with \hat{y} directed slope and \hat{x} directed slope, $\vec{d}_i = \hat{y}$ and $\vec{d}_j = \hat{x}$, follows. Using the notation $R_{yx} = R_{yx}(x_o, y_o)$. Eqn. (3.11) can be written as

$$\begin{aligned}
 R_{yx} = & \int \int \int \int dx dx' dy dy' \left(\frac{1}{d^2} \left(\delta(x + \frac{d}{2}) - \delta(x - \frac{d}{2}) \right) \text{rect} \left(\frac{y}{d} \right) \right) \\
 & \times \left(\frac{1}{d^2} \left(\delta(y' + \frac{d}{2} - y_o) - \delta(y' - \frac{d}{2} - y_o) \right) \text{rect} \left(\frac{x' - x_o}{d} \right) \right) \\
 & \times \left(\Gamma_\phi(0,0) - \frac{1}{2} D_\phi(x - x', y - y') \right). \tag{B.17}
 \end{aligned}$$

Rearranging terms, the equation can be written

$$\begin{aligned}
 R_{yx} = & \frac{1}{d^4} \int \int \int \int dx dx' dy dy' \text{rect} \left(\frac{y}{d} \right) \text{rect} \left(\frac{x' - x_o}{d} \right) \\
 & \times \left[\delta(x + \frac{d}{2}) \delta(y' + \frac{d}{2} - y_o) - \delta(x + \frac{d}{2}) \delta(y' - \frac{d}{2} - y_o) \right. \\
 & \quad \left. - \delta(x - \frac{d}{2}) \delta(y' + \frac{d}{2} - y_o) + \delta(x - \frac{d}{2}) \delta(y' - \frac{d}{2} - y_o) \right] \\
 & \times \left(\Gamma_\phi(0,0) - \frac{1}{2} D_\phi(x - x', y - y') \right). \tag{B.18}
 \end{aligned}$$

Use the von Karman structure function defined in Eqn. (B.4) and the sifting property of delta functions

$$\begin{aligned}
 R_{yx} = & -0.08663 \left(\frac{L_o}{r_o} \right)^{\frac{5}{6}} \frac{1}{d^4} \int \int dx' dy \text{rect} \left(\frac{x' - x_o}{d} \right) \text{rect} \left(\frac{y}{d} \right) \\
 & \times \left(\frac{\Gamma[1/6]}{\pi^{\frac{1}{6}}} \left(\frac{\sqrt{(x' - \frac{d}{2})^2 + (-\frac{d}{2} + y_o - y)^2}}{L_o} \right)^{\frac{5}{6}} K_{5/6} \left[2\pi \frac{\sqrt{(x' - \frac{d}{2})^2 + (-\frac{d}{2} + y_o - y)^2}}{L_o} \right] \right. \\
 & \quad - \frac{\Gamma[1/6]}{\pi^{\frac{1}{6}}} \left(\frac{\sqrt{(x' - \frac{d}{2})^2 + (\frac{d}{2} + y_o - y)^2}}{L_o} \right)^{\frac{5}{6}} K_{5/6} \left[2\pi \frac{\sqrt{(x' - \frac{d}{2})^2 + (\frac{d}{2} + y_o - y)^2}}{L_o} \right] \\
 & \quad - \frac{\Gamma[1/6]}{\pi^{\frac{1}{6}}} \left(\frac{\sqrt{(x' + \frac{d}{2})^2 + (-\frac{d}{2} + y_o - y)^2}}{L_o} \right)^{\frac{5}{6}} K_{5/6} \left[2\pi \frac{\sqrt{(x' + \frac{d}{2})^2 + (-\frac{d}{2} + y_o - y)^2}}{L_o} \right] \\
 & \quad \left. + \frac{\Gamma[1/6]}{\pi^{\frac{1}{6}}} \left(\frac{\sqrt{(x' + \frac{d}{2})^2 + (\frac{d}{2} + y_o - y)^2}}{L_o} \right)^{\frac{5}{6}} K_{5/6} \left[2\pi \frac{\sqrt{(x' + \frac{d}{2})^2 + (\frac{d}{2} + y_o - y)^2}}{L_o} \right] \right). \tag{B.19}
 \end{aligned}$$

The rect functions define the limits of integration:

$$\begin{aligned}
R_{yx} = & 0.08663 \left(\frac{L_o}{r_o} \right)^{\frac{5}{6}} \frac{1}{d^4} \int_{-\frac{d}{2}}^{\frac{d}{2}} \int_{x_o - \frac{d}{2}}^{x_o + \frac{d}{2}} dx' dy \\
& \times \left(-\frac{\Gamma[1/6]}{\pi^{\frac{1}{6}}} \left(\frac{\sqrt{(x' - \frac{d}{2})^2 + (-\frac{d}{2} + y_o - y)^2}}{L_o} \right)^{\frac{5}{6}} K_{5/6} \left[2\pi \frac{\sqrt{(x' - \frac{d}{2})^2 + (-\frac{d}{2} + y_o - y)^2}}{L_o} \right] \right. \\
& + \frac{\Gamma[1/6]}{\pi^{\frac{1}{6}}} \left(\frac{\sqrt{(x' - \frac{d}{2})^2 + (\frac{d}{2} + y_o - y)^2}}{L_o} \right)^{\frac{5}{6}} K_{5/6} \left[2\pi \frac{\sqrt{(x' - \frac{d}{2})^2 + (\frac{d}{2} + y_o - y)^2}}{L_o} \right] \\
& + \frac{\Gamma[1/6]}{\pi^{\frac{1}{6}}} \left(\frac{\sqrt{(x' + \frac{d}{2})^2 + (-\frac{d}{2} + y_o - y)^2}}{L_o} \right)^{\frac{5}{6}} K_{5/6} \left[2\pi \frac{\sqrt{(x' + \frac{d}{2})^2 + (-\frac{d}{2} + y_o - y)^2}}{L_o} \right] \\
& \left. - \frac{\Gamma[1/6]}{\pi^{\frac{1}{6}}} \left(\frac{\sqrt{(x' + \frac{d}{2})^2 + (\frac{d}{2} + y_o - y)^2}}{L_o} \right)^{\frac{5}{6}} K_{5/6} \left[2\pi \frac{\sqrt{(x' + \frac{d}{2})^2 + (\frac{d}{2} + y_o - y)^2}}{L_o} \right] \right). \quad (B.20)
\end{aligned}$$

Perform the following change of variables to put the limits of integration in dimensionless quantities:

$$\begin{aligned}
\tilde{x}_o &= \frac{x_o}{d} \quad \text{and} \quad \tilde{y}_o = \frac{y_o}{d}, \\
\tilde{x}' &= \frac{x'}{d} \quad \text{and} \quad d\tilde{x}' = \frac{dx'}{d} \\
\tilde{y}' &= \frac{y}{d} \quad \text{and} \quad d\tilde{y}' = \frac{dy}{d}. \quad (B.21)
\end{aligned}$$

Factoring out common terms, the correlation between subapertures with \hat{y} directed slope and \hat{x} directed slope is

$$\begin{aligned}
R_{yx} = & 0.08663 \left(\frac{L_o}{r_o} \right)^{\frac{5}{6}} \frac{1}{d^2} \left(\frac{\Gamma[1/6]}{\pi^{\frac{1}{6}}} \right) \int_{-\frac{1}{2}}^{\frac{1}{2}} \int_{\tilde{x}_o - \frac{1}{2}}^{\tilde{x}_o + \frac{1}{2}} d\tilde{x}' d\tilde{y}' \\
& \times \left(-\left(\frac{d\sqrt{(\tilde{x}' - \frac{1}{2})^2 + (-\frac{1}{2} + \tilde{y}_o - \tilde{y})^2}}{L_o} \right)^{\frac{5}{6}} K_{5/6} \left[2\pi \frac{d\sqrt{(\tilde{x}' - \frac{1}{2})^2 + (-\frac{1}{2} + \tilde{y}_o - \tilde{y})^2}}{L_o} \right] \right. \\
& + \left(\frac{d\sqrt{(\tilde{x}' - \frac{1}{2})^2 + (\frac{1}{2} + \tilde{y}_o - \tilde{y})^2}}{L_o} \right)^{\frac{5}{6}} K_{5/6} \left[2\pi \frac{d\sqrt{(\tilde{x}' - \frac{1}{2})^2 + (\frac{1}{2} + \tilde{y}_o - \tilde{y})^2}}{L_o} \right] \\
& + \left(\frac{d\sqrt{(\tilde{x}' + \frac{1}{2})^2 + (-\frac{1}{2} + \tilde{y}_o - \tilde{y})^2}}{L_o} \right)^{\frac{5}{6}} K_{5/6} \left[2\pi \frac{d\sqrt{(\tilde{x}' + \frac{1}{2})^2 + (-\frac{1}{2} + \tilde{y}_o - \tilde{y})^2}}{L_o} \right] \\
& \left. - \left(\frac{d\sqrt{(\tilde{x}' + \frac{1}{2})^2 + (\frac{1}{2} + \tilde{y}_o - \tilde{y})^2}}{L_o} \right)^{\frac{5}{6}} K_{5/6} \left[2\pi \frac{d\sqrt{(\tilde{x}' + \frac{1}{2})^2 + (\frac{1}{2} + \tilde{y}_o - \tilde{y})^2}}{L_o} \right] \right), \quad (B.22)
\end{aligned}$$

where R_{yx} is a function of \tilde{x}_o and \tilde{y}_o , the normalized *hatx* and \hat{y} separation of the subapertures.

The correlation between subapertures with \hat{x} directed slope and \hat{y} directed slope is developed in the same manner.

$$\begin{aligned}
R_{xy} = & 0.08663 \left(\frac{L_o}{r_o} \right)^{\frac{5}{6}} \frac{1}{d^2} \left(\frac{\Gamma[1/6]}{\pi^{\frac{1}{6}}} \right) \int_{-\frac{1}{2}}^{\frac{1}{2}} \int_{\tilde{y}_o - \frac{1}{2}}^{\tilde{y}_o + \frac{1}{2}} dy' dx \\
& \times \left(- \left(\frac{d\sqrt{(\tilde{y}' - \frac{1}{2})^2 + (-\frac{1}{2} + \tilde{x}_o - \tilde{x})^2}}{L_o} \right)^{\frac{5}{6}} K_{5/6} \left[2\pi \frac{d\sqrt{(\tilde{y}' - \frac{1}{2})^2 + (-\frac{1}{2} + \tilde{x}_o - \tilde{x})^2}}{L_o} \right] \right. \\
& + \left(\frac{d\sqrt{(\tilde{y}' - \frac{1}{2})^2 + (\frac{1}{2} + \tilde{x}_o - \tilde{x})^2}}{L_o} \right)^{\frac{5}{6}} K_{5/6} \left[2\pi \frac{d\sqrt{(\tilde{y}' - \frac{1}{2})^2 + (\frac{1}{2} + \tilde{x}_o - \tilde{x})^2}}{L_o} \right] \\
& + \left(\frac{d\sqrt{(\tilde{y}' + \frac{1}{2})^2 + (-\frac{1}{2} + \tilde{x}_o - \tilde{x})^2}}{L_o} \right)^{\frac{5}{6}} K_{5/6} \left[2\pi \frac{d\sqrt{(\tilde{y}' + \frac{1}{2})^2 + (-\frac{1}{2} + \tilde{x}_o - \tilde{x})^2}}{L_o} \right] \\
& \left. - \left(\frac{d\sqrt{(\tilde{y}' + \frac{1}{2})^2 + (\frac{1}{2} + \tilde{x}_o - \tilde{x})^2}}{L_o} \right)^{\frac{5}{6}} K_{5/6} \left[2\pi \frac{d\sqrt{(\tilde{y}' + \frac{1}{2})^2 + (\frac{1}{2} + \tilde{x}_o - \tilde{x})^2}}{L_o} \right] \right). \tag{B.23}
\end{aligned}$$

Appendix C. Shot limited performance

This appendix derives a centroid shift estimator optimized for a quadcell detector with shot noise. Equations developed by Tyler and Fried [27] were used for this derivation. Given incident plane

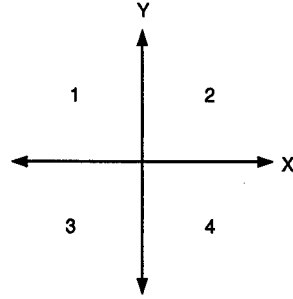


Figure C.1 Quad cell detector configuration

waves in the subaperture and no read noise in the detection process, the authors derived a shift estimator that was optimized for shot noise. A single lens imaging system with a detector located at the focal length forms an intensity distribution centered on the optical axis when when incident wavefront is planer. Shot noise in the detection process will result in centroids shifted off the optical axis. The distance the centroid deviated from the optical axis is the shot induced error. If the centroid shift errors are assumed to be small, a linear relationship can be found between the detected centroid position, \vec{x} , and the difference in intensities detected on each half of the detector in the \hat{x} and \hat{y} directions, ΔI_x and ΔI_y . Since the actual centroid distributions are centered on the optical axis, the equation developed in this appendix will be the shot limited estimate for the centroid shift.

The following derivation is for the shift in the \hat{x} direction. ΔI_x is the sum of the detected signal on quadrants 2 and 4 minus the sum of the detected signal on quadrants 1 and 3.

The expected intensity difference is defined:

$$\Delta I_x = \int_0^\infty df_x F(f_x + f_{x_o}) - \int_{-\infty}^0 d\alpha F(f_x + f_{x_o}), \quad (C.1)$$

where F was the one dimensional point spread function (PSF):

$$F(f_x) = \int dx \tilde{I}(x, 0) T(x, 0) \exp^{2\pi j f_x x}. \quad (\text{C.2})$$

First the Fourier transform of the irradiance on the detector, \tilde{I} , is defined:

$$\tilde{I}(x, y) = \int \int df_x df_y O_o(f_x, f_y) \exp^{-2\pi j(x f_x + y f_y)}, \quad (\text{C.3})$$

where $O_o(f_x, f_y)$ is the object irradiance. Using a point source irradiance, $O_o(f_x, f_y)$ is defined:

$$O_o(f_x, f_y) = \frac{I_o}{d_w^2} \delta(f_x, f_y), \quad (\text{C.4})$$

where I_o is the total intensity on the detector and d_w is the width of the wavefront sensor subaperture. Solving for \tilde{I} in Eqn (C.3):

$$\tilde{I}(x, y) = \frac{I_o}{d_w^2}. \quad (\text{C.5})$$

Next, the optical transfer function $T(f_x, f_y)$ must be approximated. The result is simply the autocorrelation of the pupil function:

$$\begin{aligned} T(x, y) &= \int \int df_x df_y |\tilde{P}(f_x, f_y)|^2 \exp^{-2\pi j(x f_x + y f_y)} \\ &= \mathcal{F}^{-1}[|\tilde{P}(f_x, f_y)|^2] \\ &= \mathcal{F}^{-1}[\tilde{P}(f_x, f_y)] \star \mathcal{F}^{-1}[\tilde{P}(f_x, f_y)] \\ &= P(x, y) \star P(x, y), \end{aligned} \quad (\text{C.6})$$

where \mathcal{F} is the Fourier transform and the pupil function for a square aperture is defined:

$$P(x, y) = \text{rect}\left(\frac{x}{d_w}\right) \text{rect}\left(\frac{y}{d_w}\right), \quad (\text{C.7})$$

where the rect function was defined in Eqn. (2.5). The optical transfer function in Eqn. (C.6) can be written as:

$$T(x, y) = d_w^2 \left(1 - \frac{|x|}{d_w}\right) \left(1 - \frac{|y|}{d_w}\right) \text{ for } |x| \leq d_w \text{ and } |y| \leq d_w. \quad (\text{C.8})$$

Solving for F in Eqn. (C.2), the 1 dimensional PSF became:

$$\begin{aligned} F(f_x) &= \int dx I_o \left(1 - \frac{|x|}{d_w}\right) \exp^{2\pi j x f_x} \\ &= I_o d_w \text{sinc}^2(d_w f_x). \end{aligned} \quad (\text{C.9})$$

Since the centroid displacement was small, the authors used the first order term of a Taylor series expansion about x_o for Eqn. (C.1) in order to relate the difference in intensity ΔI_x to the object displacement x_o .

$$\Delta I_x = -2 \frac{x_o}{\lambda z} F(0). \quad (\text{C.10})$$

Solving for $F(0)$ in Eqn. (C.9):

$$F(0) = I_o d_w. \quad (\text{C.11})$$

The final form of the centroid estimator can now be found. Solving Eqn. (C.10) for the centroid shift in the \hat{x} direction, x_o :

$$x_o = \frac{-\Delta I_x}{I_o} \frac{\lambda f_l}{2d_w}, \quad (\text{C.12})$$

where z is the focal length of the system f_l , λ is the average wavelength, d_w is the width of the wavefront sensor subaperture, ΔI_x is the the sum of the detected signal on quadrants 2 and 4 minus the sum of the detected signal on quadrants 1 and 3, and I_o is the total detected signal. The centroid shift in the \hat{y} direction is found in the same manner.

$$y_o = \frac{-\Delta I_y}{I_o} \frac{\lambda f_l}{2d_w}, \quad (\text{C.13})$$

where ΔI_y is the the sum of the detected signal on quadrants 3 and 4 minus the sum of the detected signal on quadrants 1 and 2. The centroid shift estimate can then be written as

$$\vec{x} = x_o \hat{x} + y_o \hat{y}. \quad (\text{C.14})$$

Appendix D. Wavefront sensor source code listing

This Appendix contains the source code listing for the wavefront sensor and the functions it calls.

D.1 Wavefront sensor code

```

% *****
% *****
%      Troy B Van Caster  GE-97D
%      Hartmann Wavefront Sensor Simulation
%      Last Modified: 30 Jun 1997
% *****
% *****
%
% This function returns a vector xest with x and y shift estimates and
% a vector xact with actual x and y shift values for the centroid
% location in each subaperture. The function is called as follows:
%
% [xest,xact] = wfs(screen1,naps,foc,diam,lambda,ccdnumb,
%                  rn,K,tilton,dutyc,solap)
%
function [xest,xact] = wfs1(screen1, ...
    naps, ...
    foc, ...
    diam, ...
    lambda, ...
    ccdnumb, ...
    rn, ...
    K, ...
    tilton, ...
    dutyc, ...
    solap)

% screen1 is the phase screen in the aperture of the
% wavefront sensor.
%
% Parameters in the function call
%   naps - N where N*N is the total number of subapertures
%   foc - subaperture focal length
%   diam - subaperture pupil diameter
%   lambda - average wavelength
%   ccdnumb - M where M*M is the number of detector pixels per subaperture
%   rn - read noise variance
%   K - average photon count per subaperture
%   tilton - one=remove tilt zero=retain tilt
%   dutyc - duty cycle of the detector
%   solap - subaperture overlap one=allowed zero=not allowed
%
% Variables used in this function
%   nft - the size of the matrix containing the intensity distribution
%         data for one subaperture detector
%   Na - the array size of the phase screen in each subaperture
%   nn - the overall array size
%   amattot - the matrix containing complex amplitude data for all
%             subapertures in the wavefront sensor array
%   mattot - the matrix containing the intensity distribution for all
%            subapertures in the wavefront sensor array
%   sapmask - subaperture mask for intensity overlap
%   mat1,mat2 - used to find the estimated centroid position
%   slc - used to make the intensity pattern an even multiple
%         of the CCD detector array
%   delx,dely - vectors used in the moment calculation
%   dphix,dphiy - used in the actual centroid calculation
%
% *****
%      function begins
% *****

```

```

% *****
% calculate some preliminary items
% *****

Na=15; %This is the number of samples in the subaperture

% Determine the number of pixels in the transform matrix window that are
% required to physically occupy the space on the detector array in each
% subaperture.
nft=floor((diam*64)/((Na-1)*lambda*(foc/diam)))+1;

% Make sure nft<=63, otherwise the indexes to matrices are all messed up.
% If nft is too large, increase the subaperture "window" size. If nft
% cannot be made small enough by increasing Na, the function will crash.
while nft>63 & Na<40
    Na=Na+1;
    nft=floor((diam*64)/((Na-1)*lambda*(foc/diam)))+1;
end

% Force the size of the transform matrix window to be odd and center it on
% pixel (33,33). This places the maximum intensity value at the center of
% each subaperture and ensures the fftshift command will properly orient the
% maximum to the upper left corner before using the fft2 command.
if floor(nft/2)~=nft/2
    nft=nft-1;
end

% Create a mask for the subaperture. If no overlap is desired, mask the
% overlap area with zeros.
if solap==1
    sapmask=ones(63);
else
    sapmask=zeros(63);
    sapmask(32-(nft-1)/2:32+(nft-1)/2,32-(nft-1)/2:32+(nft-1)/2)=ones(nft);
end

% Scale the photon count per subaperture by the duty cycle of the detector array.
K=K*dutyc;

% Remove tilt from phase screen if required.
if tilton==1
    screen1=tiltoff(screen1);
end

% Initialize the detector array (amattot) to zero.
amattot=zeros(nft*naps+(64-1-nft));

% Increase the number of samples in the phase screen so there are Na*Na
% samples for each subaperture screen1=resize(screen1,naps*Na).

% *****
% compute complex amplitude on the detector
% *****

p=1;
for hc=1:naps
    for vc=1:naps

% Window the phase screen data into the 64*64 array.
mat1=zeros(64);
mat1(33-(Na-1)/2:33+(Na-1)/2,33-(Na-1)/2:33+(Na-1)/2)= ...
    exp(screen1((hc-1)*Na+1:(hc-1)*Na+Na,(vc-1)*Na+1:(vc-1)*Na+Na).*(1*sqrt(-1)));

% Calculate the actual x and y positions.
dphix=(sum(screen1((hc-1)*Na+1:(hc-1)*Na+Na,(vc-1)*Na+Na))-...
    sum(screen1((hc-1)*Na+1:(hc-1)*Na+Na,(vc-1)*Na+1))/Na;
dphiy=(sum(screen1((hc-1)*Na+Na,(vc-1)*Na+1:(vc-1)*Na+Na))-...
    sum(screen1((hc-1)*Na+1,(vc-1)*Na+1:(vc-1)*Na+Na))/Na;
xact(p*p+1,1)=[dphix*foc*lambda/(2*pi*diam);dphiy*foc*lambda/(2*pi*diam)];

```

```

p=p+2;
% Take FFT of the wavefront in the subaperture to get complex amplitude data.
mat2=fftshift(fft2(fftshift(mat1)));
% Add complex amplitudes to amattot matrix.
amattot((hc-1)*nft+1:(hc-1)*nft+64-1,(vc-1)*nft+1:(vc-1)*nft+64-1)=...
amattot((hc-1)*nft+1:(hc-1)*nft+64-1,(vc-1)*nft+1:(vc-1)*nft+64-1)+...
mat2(2:64,2:64).*sapmask;
end
end
% *****
% Calculate intensity on the detector array
% *****
mattot=amattot.*conj(amattot);
% *****
% Determine detected intensities for each subaperture
% and find the estimated x and y offsets
% *****
% scl is an integer multiple of the ccd array size. The intensity data in
% each subaperture is resized from nft*nft to the smallest integer multiple
% of ccddnumb larger than nft.
scl=2;
while scl*ccddnumb < nft
scl=scl+1;
end
for hc=1:naps
for vc=1:naps
% Pull off individual subaperture intensity patterns from mattot.
mat1=zeros(nft);
mat1=mattot((64-nft-1)/2+(hc-1)*nft+1:(64-nft-1)/2+(hc-1)*nft+nft,...
(64-nft-1)/2+(vc-1)*nft+1:(64-nft-1)/2+(vc-1)*nft+nft);
mat2=mat1./max(max(mat1)); %data in mat2
% Find the detected photon count for each pixel in the subaperture detector
% array.
mat1=resize(mat2,scl*ccddnumb); %data in mat1
mat2=zeros(ccddnumb);
for x=1:ccddnumb
for y=1:ccddnumb
mat2(x,y)=sum(sum(mat1((x-1)*scl+1:(x-1)*scl+scl,...
(y-1)*scl+1:(y-1)*scl+scl)));
end
end %data in mat2
% Normalize the subaperture photon count to K.
total=sum(sum(mat2));
mat1=((mat2.*K)./total); %data in mat1
% Account for shot noise.
mat2=poisson2(mat1);
mat1=mat2; %data in mat1
% Add read noise.
mat2=mat1+rn*randn(ccddnumb); %data in mat2
% Calculate x and y offsets using a moment calculation.
delx=((1:ccddnumb)-(ccddnumb+1)/2)*diam/ccddnumb';
if sum(sum(mat2))==0
xoff(hc,vc)=0;
yoff(hc,vc)=0;
else

```

```

        xoff(hc,vc)=sum(mat2)*delx/sum(sum(mat2));
        yoff(hc,vc)=sum(mat2')*delx/sum(sum(mat2));
    end
end
end
% *****
% Stack shift estimate results into a column vector
% *****
p=1;
for hc=1:naps
    for vc=1:naps
        xest(p:p+1,1)=[xoff(hc,vc);yoff(hc,vc)];
        p=p+2;
    end
end
% *****
% end of function
% *****

```

230

240

D.2 Poisson number generator

```

% This program takes an n*n matrix and returns
% an n*n matrix whose values are a random deviate
% drawn from a poisson distribution generated from
% the value of each entry using rand
% as a source for uniformly distributed deviates
% This program was generated from Numerical Recipe
% The Art of Scientific Computing 1986, p.207.

function [newmat] = poisson2(mat)

rand('seed',sum(100*clock));
n=length(mat);
for x=1:n
    for y=1:n
        pmean=mat(x,y);
        if pmean<12 %use direct method
            gpois=exp(-pmean);
            empois=-1;
            tpois=1;
            empois=empois+1;
            tpois=tpois*rand;
            while tpois>gpois
                empois=empois+1;
                tpois=tpois*rand;
            end
        else %use the rejection method
            sqpois=sqrt(2*pmean);
            alxmpois=log(pmean);
            gpois=pmean*alxmpois-gammain(pmean+1);
            ypois=tan(pi*rand); %Y is a deviate from a Lorentzian comparison
            empois=sqpois*ypois+pmean;
            while empois<0 % continue until empois>=0
                ypois=tan(pi*rand); %Y is a deviate from a Lorentzian comparison
                empois=sqpois*ypois+pmean;
            end
            empois=floor(empois);
            tpois=0.9*(1+ypois^2)*exp(empois*alxmpois-gammain(empois+1)-gpois);
            while rand > tpois
                ypois=tan(pi*rand);
                empois=sqpois*ypois+pmean;
                while empois<0
                    ypois=tan(pi*rand);
                    empois=sqpois*ypois+pmean;
                end
                empois=floor(empois);
                tpois=0.9*(1+ypois^2)*exp(empois*alxmpois-gammain(empois+1)-gpois);
            end
            newmat(x,y)=empois;
        end
    end
end

```

10

20

30

40

end
end

50

D.3 Phase screen tilt removal

```
% *****  
% *****  
% ** Troy B Van Caster GE-97D  
% ** Phase screen tilt removal  
% ** Last modified 15 May 97  
% *****  
% *****
```

% This subroutine removes the tilt from a phase screen.

10

function [tilto] = tiltoff(tilt)

l=length(tilt);

cent=(l+1)/2;

sumx=0;

sumy=0;

sumxx=0;

sumyy=0;

20

for x=1:l

for y=1:l

 sumx=sumx+tilt(x,y)*(x-cent)/cent;

 sumy=sumy+tilt(x,y)*(y-cent)/cent;

 sumxx=sumxx+((x-cent)/cent)^2;

 sumyy=sumyy+((y-cent)/cent)^2;

end

end

30

tx=sumx./sumxx;

ty=sumy./sumyy;

for x=1:l

for y=1:l

 tilto(x,y)=tilt(x,y)-tx*(x-cent)/cent-ty*(y-cent)/cent;

end

end

Appendix E. Correlation generation source code listing

This Appendix contains the source code listing the correlation matrices.

E.1 Source code for building Kolmogorov correlation matrices

```
% *****
% *****
% ** Troy B Van Caster GE-97D **
% ** Kolmogorov slope correlation **
% ** matrix generator **
% ** Last Modified 5 Jun 97 **
% *****
% *****
% This builds a slope covariance matrix using the kolmogorov
% structure function. The program calculates the first row
% values then uses symmetry to fill in the rest of the matrix.
% The program builds x offset and y offset matrices as well
% as a ref matrix. xoff and yoff are subap*subap in size and
% contain normalized x and y offsets from x1,y1 to x2,y2. The
% ref matrix is used to fill in the rest of the correlation
% matrix. It is indexed using the x and y offsets and contains
% a flag to the appropriate first row element to place in the
% matrix. Called by R = kcorrmat(asize,d,ro)
%
% This program calls the following functions:
% kolzx - for correlation of slopes that are in the same direction
% for zx slopes: val=quad8('kolzx',-1+xoff,1+xoff,[],[],xoff,yoff)
% xoff is the x offset normalized by d
% yoff is the y offset normalized by d
% limits of integration are from -1 to 1
%
% kolxyfun - returns xy slope correlation
% calls function integrate.m and kolxy.m
% xoff is the x offset normalized by d
% yoff is the y offset normalized by d
% limits of integration are from -1/2 to 1/2
%
% kolxy - determines xy slope correlation
% val=quad8('kolxy',xoff-1/2,xoff+1/2,[],[],y,xoff,yoff)
% must be used in a 2D integration format
% *****
function R = kcorrmat(asize,d,ro)
subap=asize^2; % length of covariance matrix
% *****
% build x and y offset matrices and the reference matrix
% *****
index=0;
for x=1:asize
for y=1:asize
index=index+1;
ref(y,x)=index*2-1;
xtemp(x,y)=(y-x);
end
end
for x=1:asize
for y=1:asize
xoff(asize*x-asize+1:asize*x,asize*y-asize+1:asize*y)=xtemp;
end
endM
for x=1:asize^2
for y=1:asize^2
yoff(x,y)=(floor((y-1)/asize)-floor((x-1)/asize));
```

```

end
end

% *****
% calculate the first row of the correlation matrix
% *****

x=1;
for y=1:subap*2
    if (floor(y/2)) == (y/2) %its an xx/yy correlation
        R(x,y)=quad8('kolxx',yoff(1+floor(x/2),1+floor(y/2))-1,yoff(1+floor(x/2),1+floor(y/2))+1,...
            [],[],xoff(1+floor(x/2),1+floor(y/2)),yoff(1+floor(x/2),1+floor(y/2)));
    else %its an xy/yz correlation
        %check to see if the subapertrues are in the same row/column
        if xoff(1+floor(x/2),floor(y/2))*yoff(1+floor(x/2),floor(y/2))==0
            R(x,y)=0;
        else
            R(x,y)=kolxyfun(xoff(1+floor(x/2),floor(y/2)),yoff(1+floor(x/2),floor(y/2)));
        end
    end
end
end

% Fill in the rest of the upper diagonal matrix
% start with y rows

for x=2:2:subap*2
    for y=x:subap*2
        if (floor(y/2)) == (y/2) %its an xx/yy correlation
            R(x,y)=R(1, ref(abs(yoff(floor(x/2),floor(y/2))+1,...
                abs(xoff(floor(x/2),floor(y/2))+1)));
        else %its an xy/yz correlation
            R(x,y)=R(1,ref(abs(yoff(floor(x/2),floor(y/2)+1))+1,...
                abs(xoff(floor(x/2),floor(y/2)+1))+1));
        end
        %check the x and y offsets to determine sign of cross terms
        %remember, they are all negative to start with
        %if the xoff or the yoff is negative, make the cross term positive
        if ( xoff(floor(x/2),floor(y/2)+1) )*( yoff(floor(x/2),floor(y/2)+1) ) < 0
            R(x,y)=-1*R(x,y);
        end
    end
end
end
end

% add x rows
for x=3:2:subap*2
    for y=x:subap*2
        if (floor(y/2)) == (y/2) %its an xx/yy correlation
            R(x,y)=R(1, ref(abs(xoff(floor(x/2)+1,floor(y/2)+1))+1,...
                abs(yoff(floor(x/2)+1,floor(y/2)+1))+1 ));
        else %its an xy/yz correlation
            R(x,y)=R(1,ref(abs(xoff(floor(x/2)+1,floor(y/2))+1))+1,...
                abs(yoff(floor(x/2)+1,floor(y/2))+1))+1);
        end
        %check the x offset and if negative, make the correlation value negative
        if ( xoff(floor(x/2)+1,floor(y/2)) )*( yoff(floor(x/2)+1,floor(y/2)) ) < 0
            R(x,y)=-1*R(x,y);
        end
    end
end
end
end

%*****
%mirror the matrix
R=R+triu(R,1)';
R=R*(1/d)^2*(d/ro)^(5/3);
%*****

% *****
% *****
% ** Troy B Van Caster GE-97D **
% ** Kolmogorov slope correlation **
% ** matrix generator **

```

```

% **      Last Modified 5 Jun 97      **
% *****
% *****
10

function val=kolxx(y,xoff,yoff)

val=3.44*(1-abs(yoff-y)).*(...
((xoff+1)^2+y.^2).^(5/6)+...
((xoff-1)^2+y.^2).^(5/6)-...
2*(xoff^2+y.^2).^(5/6) );

% *****
% *****
% **      Troy B Van Caster  GE-97D      **
% **      2D integrator for xy and yz      **
% **      slope correlation terms      **
% **      Last Modified 3 May 97      **
% *****
% *****
10

% *****
% This function returns the value for a 2D integration
% for the slope correlation matrix xy and yz terms.
% The integral is evaluated for several values of y,
% then sent to integrate.m to do the 2D integration.
% *****

function val = kolxyfun(xoff,yoff)

ylim=.5;
step=.1;
c=0;
20

for x=-ylim:step:ylim;
c=c+1;
ma(c)=quad8('kolxy',yoff-ylim,yoff+ylim,[],[],x,xoff);
end
ma=ma';
h=[step];
val=integrate(ma,h);
30

% *****
% *****
% **      Troy B Van Caster  GE-97D      **
% **      Slope Correlation Matrix for      **
% **      xy or yz directed slopes      **
% **      Last Modified 5 Jun 97      **
% *****
% *****
10

% *****
% This function is called by kolxyfun.m and is used
% to evaluate the correlation for slopes in the xy
% or yz direction when the limits of integration span
% the origin. The modified Bessel function uses a
% two term expansion to prevent the integral from
% having an infinite value.
% *****

function val = kolxy(y,x,xoff)
val=-3.44*(...
((y+1/2).^2+(-1/2+xoff-x)^2).^(5/6) -...
((y+1/2).^2+(1/2+xoff-x)^2).^(5/6) -...
((y-1/2).^2+(-1/2+xoff-x)^2).^(5/6) +...
((y-1/2).^2+(1/2+xoff-x)^2).^(5/6) );
20

```

E.2 Source code for building von Karman correlation matrices

```

function [R] = vcorrmat(ysize,d,ro,lo)

% *****
% *****
% **  Troy B Van Caster  GE-97D  **
% **  von Karman slope correlation  **
% **      matrix generator      **
% **    Last Modified 5 Jun 97    **
% *****
% *****
%
% This builds a slope covariance matrix using the von Karman
% structure function. The program calculates the first row
% values then uses symmetry to fill in the rest of the matrix.
% The program builds x offset and y offset matrices as well
% as a ref matrix. xoff and yoff are subap*subap in size and
% contain normalized x and y offsets from x1,y1 to x2,y2. The
% ref matrix is used to fill in the rest of the correlation
% matrix. It is indexed using the x and y offsets and contains
% a flag to the appropriate first row element to place in the
% matrix. Called by R=vcorrmat(ysize,d,ro,lo)

% This program calls the following functions:
%
% vonkxx - for correlation of slopes that are in the same direction
% for xx slopes: val=quad8('vonkxx',-1+xoff,1+xoff,[],[],xoff,yoff)
% xoff is the x offset normalized by d
% yoff is the y offset normalized by d
% limits of integration are from -1 to 1
%
% vonkxyfun - returns xy slope correlation
% calls function integrate.m and vonkxy.m
% xoff is the x offset normalized by d
% yoff is the y offset normalized by d
% limits of integration are from -1/2 to 1/2
%
% vonkxy - determines xy slope correlation
% val=quad8('vonkxy',xoff-1/2,xoff+1/2,[],[],y,xoff,yoff)
% must be used in a 2D integration format
% *****

subap=ysize^2; % length of covariance matrix

% *****
% build x and y offset matrices and the reference matrix
% *****
index=0;
for x=1:ysize
for y=1:ysize
index=index+1;
ref(y,x)=index*2-1;
xtemp(x,y)=(y-x);
end
end
for x=1:ysize
for y=1:ysize
xoff(ysize*x-ysize+1:ysize*x,ysize*y-ysize+1:ysize*y)=xtemp;
end
endM

for x=1:ysize^2
for y=1:ysize^2
yoff(x,y)=(floor((y-1)/ysize)-floor((x-1)/ysize));
end
end

% *****
% calculate the first row of the correlation matrix
% *****

x=1;
for y=1:subap*2

```



```

% below a certain level, then the modified Bessel
% function uses a series expansion. There is also
% a check to make sure that the series expansion is
% used when the correlation between adjacent subapertures.
% This prevents the integral from taking on an infinite
% value.
%
% For evaluation in the xx direction, use the form:
%
% quad8('vonkxx',yoff-1,yoff+1,[],[],yoff,xoff,lo,d)
%
% For evaluation in the yy direction, use the form:
%
% quad8('vonkxx',xoff-1,xoff+1,[],[],xoff,yoff,lo,d)
% *****
function val=vonkxx(y,xoff,yoff,lo,d)

% evaluate the three arguments
arg1=d/lo*(sqrt(xoff^2+y.^2));
arg2=d/lo*(sqrt((xoff+1)^2+y.^2));
arg3=d/lo*(sqrt((xoff-1)^2+y.^2));
threshold=.02;

% Define some initial parameters
A=0.08663*(lo)^(5/3);
B1=gamma(1/6)/pi^(1/6);
B2=pi/(2*sin(5/6*pi));
trifun=(1-abs(yoff-y));
term1=pi*(-5/6)/gamma(1/6);

% Check the first term of the integral
if (arg1 <= threshold) | (xoff<=1) |(yoff<=1) % use the series expansion
    term2=pi^(1+1/6)/gamma(1+1/6)*arg1.^2;
    term3=pi^(5/6)/gamma(1+5/6)*arg1.^(1+2/3);
    term4=pi^(2+5/6)/gamma(2+5/6)*arg1.^(3+2/3);
    t1=trifun.*A.*B1.*B2.*(term1+term2-term3-term4);
else % use the actual function
    t1=trifun.*A.*B1.*arg1.^(5/6).*besselk(5/6,2*pi*arg1);
end

% Check the second term of the integral
if (arg2 <= threshold) | (xoff<=1) |(yoff<=1) % use the series expansion
    term2=pi^(1+1/6)/gamma(1+1/6)*arg2.^2;
    term3=pi^(5/6)/gamma(1+5/6)*arg2.^(1+2/3);
    term4=pi^(2+5/6)/gamma(2+5/6)*arg2.^(3+2/3);
    t2=trifun.*A.*B1.*B2.*(term1+term2-term3-term4);
else % use the actual function
    t2=trifun.*A.*B1.*arg2.^(5/6).*besselk(5/6,2*pi*arg2);
end

% Check the third term of the integral
if (arg3 <= threshold) | (xoff<=1) |(yoff<=1) % use the series expansion
    term2=pi^(1+1/6)/gamma(1+1/6)*arg3.^2;
    term3=pi^(5/6)/gamma(1+5/6)*arg3.^(1+2/3);
    term4=pi^(2+5/6)/gamma(2+5/6)*arg3.^(3+2/3);
    t3=trifun.*A.*B1.*B2.*(term1+term2-term3-term4);
else % use the actual function
    t3=trifun.*A.*B1.*arg3.^(5/6).*besselk(5/6,2*pi*arg3);
end

val=2*t1-t2-t3;

% *****
% *****
% ** Troy B Van Caster GE-97D **
% ** 2D integrator for xy and yz **
% ** slope correlation terms **
% ** Last Modified 20 April 97 **
% *****
% *****
%

```

```

%*****
% This function returns the value for a 2D integration
% of the slope correlation matrix xy and yx terms.
% The integral is evaluated for several values of y,
% then sent to integrate.m to do the 2D integration.
%*****

```

```

function val = vonkxyfun(xoff,yoff,lo,d);

ylim=.5;
step=.1;
c=0;

for x=-ylim:step:ylim;
c=c+1;
ma(c)=quad8('vonkxy',yoff-ylim,yoff+ylim,[],[],x,xoff,yoff,lo,d);
end
ma=ma';
h=[step];
val=integrate(ma,h);

```

E.3 Function for Two dimensional numerical integration

```

function F = integrate(f,h)
% function F = integrate(f,h)
% provides numeric integration via Newton Coates methods
% f is the function to be integrated sampled at evenly spaced
% intervals h.
% f - Matrix of column vectors of samples of functions to be integrated
% h - column vector of the width of the spaces for each column of f
% Let N = length of sampled function
% If (N-1)/4 is an integer, we use Newton Coats K=4
% If (N-1)/3 is an integer, we use Newton Coats K=3
% If (N-1)/2 is an integer, we use Newton Coats K=2 (Simpsons)
% If (N-1)/1 is an integer, we use trapezoidal K=1 rule
%
% K=1, F = h/2*(f_1+f_N+sum(w*f(2:N-1))); w = [2 2 2 ... 2];
% K=2, F = h/3*(f_1+f_N+sum(w*f(2:N-1))); w = [4 2 4 2 ... 4]
% K=3, F = 3h/8*(f_1+f_N+sum(w*f(2:N-1))); w = [3 3 2 3 3 2 ... 3 3];
% K=4, F = 2h/45*(7f_1+7f_N+sum(w*f(2:N-1))); w = [32 12 32 14
% ..32 12 32];

W = [1 2 1 0 0 0 0;
      1 4 2 1 0 0 0;
      1 3 3 2 1 0 0;
      7 32 12 32 14 7 0];

B = [1/2 1/3 3/8 2/45];
[N,M] = size(f);
P = N-1;
for K = 4:-1:1
    if (abs(round(P/K)-P/K) < .0001)
        C = W(K,2:K+1)*ones(1,round(P/K));
        b = B(K);
        A = reshape(C,1,N-1);
        A = [W(K,1), A(1:N-2), W(K,K+2)];
        F = (h*b)'*(A*f);
        break;
    end;
end;

```

Bibliography

1. Ayers, G. R. and J. C. Dainty. "Iterative blind deconvolution method and its applications," *Optics Letters*, 7:547-549 (July 1988).
2. Beavers, W. I., et al. "Speckle Imaging Through the Atmosphere," *Lincoln Laboratories Journal*, 2:207-228 (1989).
3. Cannon, Robert C. "Global Wavefront Reconstruction using Shack Hartmann Sensors," *Journal of the Optical Society of America A*, 12:2031-2039 (September 1995).
4. Cao, Genrui and Xin Yu. "Accuracy analysis of a Hartmann-Shack wavefront sensor operated with a faint object," *Optical Engineering*, 7:2331-2335 (July 1994).
5. Consortini, A. and L. Ronchi. "Role of the outer scale of turbulence in atmospheric degradation of optical images," *Journal of the Optical Society of America A*, 69:1246-1248 (October 1973).
6. Dayton, David, et al. "Atmospheric structure function measurements with a Shack-Hartmann wave-front sensor," *Optic Letters*, 17:1737-1740 (December 1992).
7. Fried, D.L. "Limiting Resolution Looking Down Through the Atmosphere," *Journal of the Optical Society of America A*, 56:1372-1384 (October 1966).
8. Fried, D.L. "Optical Resolution Through a Randomly Inhomogeneous Medium for Very Long and Very Short Exposures," *Journal of the Optical Society of America A*, 56:1372-1379 (October 1966).
9. Fugate, R. Q., et al. "Two generations of laser guide-star adaptive optics experiments at the Starfire Optical Range," *Journal of the Optical Society of America A*, 11:310-324 (January 1994).
10. Gardner, Chester S., et al. "Design and Performance Analysis of Adaptive Optical Telescopes Using Laser Guide Stars," *Proceedings of the IEEE*, 78:1721-1743 (November 1990).
11. Goodman, Joseph W. *Statistical Optics*. New York: John Wiley and Sons, 1985.
12. Goodman, Joseph W. *Introduction to Fourier Optics*. New York: McGraw Hill, 1996.
13. Hardy, John W. "Adaptive Optics: A New Technology for the Control of Light," *Proceedings of the IEEE*, 66:651-697 (June 1978).
14. Kane, Timothy J., et al. "Wavefront Detector Optimization for Laser Guided Adaptive Telescopes," *Proceedings of the SPIE*, 1114:160-171 (1989).
15. Kay, Steven M. *Fundamentals of Statistical Signal Processing: Estimation Theory*. New Jersey: Prentice Hall, 1993.
16. Newton, Isaac. *Opticks*. New York: Dover Publications Inc., 1952.
17. Parenti, Roger R. and Richard J. Sasiela. "Laser-guide-star systems for astronomical applications," *Journal of the Optical Society of America A*, 11:288-309 (January 1994).
18. Pennington, Timothy L. *Performance Comparison of Shearing Interferometer and Hartmann Wave Front Sensors*. MS thesis, AFIT/GE/ENG/93D-31, Air Force Institute of Technology, Wright-Patterson AFB, December 1993 (AD-A274031).
19. Pennington, Timothy L., et al. "Performance measurements of Generation III wavefront sensors at the Starfire Optical Range," *SPIE*, 2534:327-337 (May 1995).

20. Primot, J., et al. "Deconvolution from wave front sensing: A new technique for compensating turbulence degraded images," *Journal of the Optical Society of America A*, 7:1598-1608 (September 1990).
21. Proakis, John G. and Dimitris G. Manolakis. *Introduction to Digital Signal Processing*. New York: Macmillian Publishing Company, 1988.
22. Roggemann, Michael C. and Byron M. Welsh. *Imaging Through Turbulence*. New York: CRC Press, 1996.
23. Sallberg, Scott A. *Maximum Likelihood estimation of Wave-Front Slopes using a Hartmann-type Sensor*. MS thesis, AFIT/GE/ENG/95D-23, Air Force Institute of Technology, Wright-Patterson AFB, December 1995.
24. Sallberg, Scott A., et al. "Maximum A-Posteriori Estimation of Wave front Slopes using a Shack-Hartmann Wavefront Sensor," *Journal of the Optical Society of America A*, 14:1347-1354 (June 1997).
25. Sillbaugh, Eric E., et al. "Characterization of atmospheric turbulence phase statistics using wave-front slope measurements," *Journal of the Optical Society of America A*, 13:2453-2460 (December 1996).
26. Snyder, Donald L., et al. "Compensation for Readout Noise in CCD Images," *Journal of the Optical Society of America A*, 12:272-283 (1995).
27. Tyler, Glenn A. and David L. Freid. "Image position error associated with a quadrant detector," *Journal of the Optical Society of America A*, 72:804-808 (December 1982).
28. Wallner, Edward P. "Optimal Wave-Front Correction using Slope Measurements," *Journal of the Optical Society of America A*, 73:1771-1776 (December 1983).
29. Weigelt, Gerd. "Speckle Imaging and Speckle Spectroscopy," *SPIE: New Technologies for Astronomy*, 1130:148-151 (1989).
30. Welsh, Byron M., "A Fourier Series Based Atmospheric Phase Screen Generator for Simulating Nonisoplanatic Geometries and Temporal Evolution." Reviewer Copy, 1997.
31. Welsh, Byron M., et al. "Fundamental Performance Comparison of a Hartmann and Shearing Interferometer Wave-front Sensor," *Applied Optics*, 34:4186-4195 (July 1995).
32. Winick, Kim A. "Cramer-Rao Lower Bounds on the Performance of Charge Coupled Device Optical Position Estimators," *Journal of the Optical Society of America A*, 11:1809-1815 (November 1986).
33. Yura, H. T. and M. T. Travis. "Centroid Anisoplanatism," *Journal of the Optical Society of America A*, 2:765-773 (May 1985).

Vita

Captain Troy B. Van Caster was born and raised in Omaha, Nebraska. After graduating from Ralston High School in 1985, he attended Iowa State University. He graduated in December 1989 with a Bachelor of Science in Electrical Engineering and was commissioned a 2nd Lieutenant in the United States Air Force. His first assignment was to Keesler Air Force Base, Mississippi, to attend Basic Communications Officer Course in October of 1990. Upon completion in February 1991, Lt. Van Caster was assigned to the 3rd Combat Communications Group, Tinker Air Force Base, Oklahoma. He served as a combat communications officer for the 31st Combat Communications Squadron until January 1993 when he was moved to the 3rd Combat Support Squadron engineering office where he was responsible for exercise planning and testing and integration of new communications systems. In Jan 1994, he was assigned to the 1st Communications Squadron, Langley Air Force Base, Virginia. As Officer in Charge of Combat Systems, he was responsible for the installation and operation of a satellite ground entry station known as *Reachback*. *Reachback* was Air Combat Command's model to provide rapid and flexible C4I support using Ground Mobile Forces Satellite Communications assets to deployed Department of Defense personnel. In August 1995, he was reassigned to the Network Services Flight where he designed WAN architectures to support the base networking requirements. Captain Van Caster completed his Masters in Engineering Management from Old Dominion University, Norfolk, Virginia, in May of 1996. He was then selected to attend the Air Force Institute of Technology in July 1996 where he specialized in Communications Systems and Optical Information Processing while pursuing his Master of Science in Electrical Engineering. His follow on assignment will be with Space Command Advanced Systems Directorate in Colorado Springs, Colorado, where he will work proof of concept and prototype development projects.

Permanent address: 7362 Drexel St
Ralston, Nebraska 68127

REPORT DOCUMENTATION PAGE			Form Approved OMB No. 0704-0188	
Public reporting burden for this collection of information is estimated to average 1 hour per response, including the time for reviewing instructions, searching existing data sources, gathering and maintaining the data needed, and completing and reviewing the collection of information. Send comments regarding this burden estimate or any other aspect of this collection of information, including suggestions for reducing this burden, to Washington Headquarters Services, Directorate for Information Operations and Reports, 1215 Jefferson Davis Highway, Suite 1204, Arlington, VA 22202-4302, and to the Office of Management and Budget, Paperwork Reduction Project (0704-0188), Washington, DC 20503.				
1. AGENCY USE ONLY (Leave blank)		2. REPORT DATE December 1997		3. REPORT TYPE AND DATES COVERED Master of Science Thesis
4. TITLE AND SUBTITLE Evaluation of a maximum a-posteriori slope estimator for a Hartmann wavefront sensor			5. FUNDING NUMBERS	
6. AUTHOR(S) Troy Bryan Van Caster, Captain, USAF				
7. PERFORMING ORGANIZATION NAME(S) AND ADDRESS(ES) School of Engineering (AFIT/ENG) Air Force Institute of Technology Wright-Patterson AFB, OH 45433-6583			8. PERFORMING ORGANIZATION REPORT NUMBER AFIT/GE/ENG/97D-08	
9. SPONSORING/MONITORING AGENCY NAME(S) AND ADDRESS(ES) Captain Bruce Stribling Phillips Laboratory/OL-YY 535 Lipoa Pkwy, Suite 200 Kihei HI 96753 808-874-1535			10. SPONSORING/MONITORING AGENCY REPORT NUMBER	
11. SUPPLEMENTARY NOTES				
12a. DISTRIBUTION AVAILABILITY STATEMENT Approved for Public Release Distribution Unlimited			12b. DISTRIBUTION CODE	
13. ABSTRACT (Maximum 200 words) <p>Current methods for estimating the wavefront slope at the aperture of a telescope using a Hartmann wavefront sensor are based upon a centroid shift estimator. The centroid shift estimator determines the displacement, or shift, of the centroid off the optical axis using a moment calculation of the intensity distributions recorded in each subaperture. This centroid shift is proportional to the average slope of the wavefront in each subaperture. A maximum a-posteriori (MAP) slope estimator takes advantage of a-priori knowledge of the wavefront slope statistics and total irradiance falling on the subaperture detector arrays when determining the shift estimate. In order to derive a closed form solution for the MAP estimator, several assumptions were made: infinite resolution on the detector arrays, no read noise in the detection process, and no intensity spillover into adjacent subapertures. By implementing the Hartmann wavefront sensor and MAP estimator in simulation, the performance of the MAP estimator was evaluated using realizable wavefront sensor parameters. While the MAP estimator mean square error (MSE) performance decreased relative to the centroid estimator MSE performance as a result of spillover, finite detector resolution, and read noise, the MAP estimator MSE performance was found to be upper bounded by the centroid estimator MSE in all cases.</p>				
14. SUBJECT TERMS wavefront sensors, wavefront estimation, atmospheric turbulence, imaging through turbulence, maximum a-posteriori estimation			15. NUMBER OF PAGES 121	
			16. PRICE CODE	
17. SECURITY CLASSIFICATION OF REPORT UNCLASSIFIED	18. SECURITY CLASSIFICATION OF THIS PAGE UNCLASSIFIED	19. SECURITY CLASSIFICATION OF ABSTRACT UNCLASSIFIED	20. LIMITATION OF ABSTRACT UL	